Lanthanum Ferrite-Based Mixed-Conducting Electrodes for Solid Oxide Fuel Cells and Electrolyzers

Tim C Geary

A dissertation submitted in partial fulfillment
of the requirements for the degree of

Doctor of Philosophy

University of Washington

2014

Reading Committee:

Stuart Adler, Chair
Daniel Schwartz
Eric Stuve

Program Authorized to Offer Degree:
Chemical Engineering

University of Washington

Abstract

Lanthanum Ferrite-Based Mixed-Conducting Electrodes for
Solid Oxide Fuel Cells and Electrolyzers

Tim C Geary

Chair of Supervisory Committee:
Prof. Stuart Adler
Chemical Engineering

Intermediate temperature solid oxide fuel cells (SOFCs) and electrolysis cells (SOECs) potentially facilitate efficient, decentralized, and environmentally sustainable interconversion of electricity and carbon-containing fuels. However, the phenomena limiting performance of the associated oxygen and fuel electrodes are poorly understood, particularly for the class of mixed ionic and electronic conducting (MIEC) electrodes gaining interest for their performance and stability. This work investigates thermodynamic, kinetic, and transport processes affecting the performance of $La_{0.9}Ca_{0.1}FeO_{3-\delta}$ (LCF) and $La_{0.6}Sr_{0.4}Co_{0.2}Fe_{0.8}O_{3-\delta}$ (LSCF) electrodes. Thermodynamic measurements on LCF reveal semiconducting behavior across a wide range of temperature and oxygen partial pressure, while also showing stability in both oxidizing and reducing conditions.

Linear and nonlinear electrochemical impedance spectroscopy (EIS, NLEIS) were used to identify rate-limiting processes occurring on LCF and LSCF cells in oxygen by comparison with porous electrode models. In both cases, results suggest the electrode surface to play a dominant role, behaving more reduced than expected from bulk measurements. Additionally, impedance measurements of LCF-91 electrodes in reducing hydrogen-water environments highlight the difficulties, both thermodynamic and transport-related, that arise when studying n-type MIECs under these conditions.

Table of Contents

1. Introduction 1
   1.1 Solid Oxide Fuel Cells and Electrolysis Cells 1
   1.2 Mixed-Conducting Perovskite Electrodes 5
      1.2.1 Thermodynamic Properties 6
      1.2.2 Transport Properties 10
   1.3 Electrode Kinetics 12
      1.3.1 Oxygen Reduction on Mixed Conducting Electrodes 12
      1.3.2 Fuel Kinetics 13
   1.4 Electrochemical Impedance Techniques 14
   1.5 Present Work 16

2. Oxygen Nonstoichiometry and Defect Chemistry of $La_{0.9}Ca_{0.1}FeO_{3-\delta}$ 18
   2.1 Background 18
   2.2 Coulometric Titration 19
   2.3 Experimental 21
      2.3.1 LCF Samples 21
      2.3.2 Coulometric Titration Cell 21
      2.3.3 Coulometric Titration Method 24
      2.3.4 X-Ray Diffraction 24
   2.4 Results and Discussion 25
      2.4.1 LCF Characterization and Stability 25
      2.4.2 Oxygen Nonstoichiometry 27
      2.4.3 Defect Model 29
   2.5 Summary 34
   2.6 Appendix A: Adaptation for Future Electrode Models 35
      2.6.1 Thermodynamic Factor 36
   2.7 Appendix B: Steady State Leak Current 37

3. Porous Electrode Modeling Framework for p-Type Mixed-Conducting Electrodes 40
   3.1 Introduction 40
   3.2 Rate-Determining Phenomena 42
      3.2.1 Thermodynamics 42
      3.2.2 Oxygen Exchange Kinetics 44
      3.2.3 Transport 46

3.3 1D Macrohomogenous Model 48
3.3.2 Nondimensionalization and Scaling 50
3.4 2D Cylindrical Model 53
3.4.1 Finite-Element Solution and Skin Layer Formulation 56
3.5 1D Macrohomogeneous Model Results 59
3.5.1 Dimensional Analysis of Linear 1D Solution 59
3.5.2 Nonlinear Harmonics for 1D Model 60
3.6 2D Cylindrical Model Results 65
3.7 Summary 70

4. Oxygen Reduction on Porous LCF-91 Electrodes 71
4.1 Introduction 71
4.2 Experimental 71
4.2.1 Symmetric Cell Fabrication 71
4.2.2 Cell Characterization 72
4.2.3 Impedance Measurements 74
4.3 Results & Discussion 76
4.3.1 Linear Impedance Spectroscopy Results 76
4.3.2 Nonlinear Impedance Spectroscopy Results 84
4.4 Summary 93

5. Oxygen Reduction on Porous LSCF-6428 Electrodes 95
5.1 Introduction 95
5.2 Experimental 96
5.2.1 Symmetric Cell Fabrication 96
5.2.2 Cell Characterization 97
5.2.3 Impedance Measurements 97
5.3 Electrochemical Analysis: Results & Discussion 98
5.3.1 Linear Impedance Spectroscopy Results 98
5.3.2 Nonlinear Impedance Spectroscopy Results 102
5.3.3 Comparison to Porous Electrode Models 104
5.4 Summary 109

6. Porous LCF-91 Electrodes in H_2-H_2O Environments 110
6.1 Introduction 110
6.2 Theory 111
6.2.1 Thermodynamics 111
6.2.2 H_2-H_2O Kinetics 113
6.2.3 Transport Properties near the p-n Transition 114
6.3 Experimental 119
6.3.1 Cell Fabrication & Characterization 119

6.3.2 Electrochemical Measurements 119
6.4 Results 121
6.4.1 Characterization and Stability 121
6.4.2 Electrochemical Measurements in H_2-H_2O 122
6.5 Discussion 131
6.6 Summary and Future Work 135

7. Summary 137
7.1 Summary of Results 137
7.2 Implications and Future Work 140

List of Figures

Figure 1.1: The working principle behind (a) SOFCs and (b) SOECs is shown for the simplified case of O_2 and H_2-H_2O streams. 2

Figure 1.2: A potential application of a combined solid oxide electrolysis and fuel cell system which simultaneously functions as both a fuel upgrader and electricity generator depending on the demand for each. 4

Figure 1.3: The perovskite crystal structure has a cubic unit cell of ABO_3, where A and B are typically rare earth or alkaline and transition metal cations, respectively. 5

Figure 1.4: Perovskites of the form (a) $La_{1-x}Sr_xFeO_{3-\delta}$ show a plateau of oxygen stoichiometry, $3-\delta$, with changing p_{O_2} occurring at $\delta = x2$, while (b) $La_{1-x}Sr_xCoO_{3-\delta}$ shows a continuous increase in nonstoichiometry with decreasing p_{O_2} (adapted from [13], [14]). 7

Figure 1.5: The observed thermodynamic behavior of $La_{0.6}Sr_{0.4}Co_{0.2}Fe_{0.8}O_{3-\delta}$ measured to decomposition, interpreted using both a metallic and semiconducting model (adapted from [16]). 9

Figure 1.6: (left) The total electrical conductivity of LSF-91 shows a minimum at the center of its p-n transition, the plateau shown in Figure 1.4a (adapted from [29]). (right) The $pO2$-independent vacancy diffusivity is inferred for LSF-91 and LSC-91 (adapted from [12]). 11

Figure 1.7: NLEIS and EIS techniques are qualitatively illustrated, and example spectra for each are shown on the right. 16

Figure 2.1: Diagram of the working principle behind coulometric titration for the perovskite sample $ABO_{3-\delta}$. 20

Figure 2.2: Schematic of the sealed, two-probe, coulometric titration cell, where the LCF sample is maintained at constant temperature. 23

Figure 2.3: Cross-sectional SEM image of screen-printed LCF ink sintered at 1050°C on a YSZ pellet, showing good adhesion of the electrode to the electrolyte. 26

Figure 2.4: . XRD spectra of 50-50 wt% samples of LCF & YSZ unsintered, and sintered at 1050˚ and 1200˚C. 26

Figure 2.5: XRD spectra of two samples of LCF powder: one exposed to a 20:1 blend of H_2-H_2O at 850˚C for 48 hours, the other exposed to air. 27

Figure 2.6: Measured nonstoichiometry of $La_{0.9}Ca_{0.1}FeO_{3-\delta}$ as a function of p_{O_2} at 750°,800°, 850°, and 900°C. Solid curves were calculated from the model discussed in the following section. The two high-p_{O_2} points at 800°C (*) were not fully equilibrated and not used in the fit. 28

Figure 2.7: Calculated defect concentrations as a function of p_{O_2}, given at 850°C. ... 31

Figure 2.8: Arrhenius plot of the equilibrium constants, K_{ox} and K_r, for $La_{0.9}Ca_{0.1}FeO_{3-\delta}$. Lines represent least-squares fits. Error bars indicate the mean variance of each model fit shown in Figure 2.6. Dotted lines indicate the model fit for $La_{0.9}Sr_{0.1}FeO_{3-\delta}$ [14]. 33

Figure 2.9: Equilibrium thermodynamic factor, $Axv0$ as function of $pO2$ in the limit of (a) high $pO2$and p-type conductivity, and (b) low $pO2$ and n-type conductivity. 37

Figure 2.10: Steady-state leak current for each voltage step. Solid lines are given by Eq. 1.2. 38

Figure 2.11: Scaled average leak current as a function of inverse temperature. Open symbols indicate cells found to have microcracks via helium leak detection. ... 39

Figure 3.1: Depiction of the oxygen reduction process on a porous mixed-conducting electrode modeled in this chapter. 41

Figure 3.2: Two surface diffusion models are considered with differing mobile species: a) surface oxygen vacancies with xv,s, and b) oxygen interstitials scaling inversely with xv,s. Adapted from Ref. [34]. 47

Figure 3.3: The 1D macrohomogeneous model is represented with color corresponding to gradients in vacancy concentration. 49

Figure 3.4: The 2D cylindrical model represents the porous electrode (left) as an array of cylinders (right), considering axial and radial transport. 54

Figure 3.5: A zero-volume electrode "surface" is numerically represented by a radial decay function, $\phi(\rho)$, staining the electrode surface with a dimensionless decay length $\delta = 0.001$. 58

Figure 3.6: A Nyquist plot of the linear impedance, ZG, results from the 1D macrohomogeneous model with dimensional arc height Rc and peak frequency ωc. 60

Figure 3.7: The case of no surface diffusion ($\nu = 0$) at thermodynamic values corresponding to p_{O_2} of 1 (red), 0.21 (green), and 0.01 atm (blue) at 800°C shows an identical linear response for (a) dissociative adsorption and (b)

chemisorption-limiting rate law. Both scenarios show a very weak variation with thermodynamic state. 62

Figure 3.8: The nonlinear response predicted for a bulk and surface diffusion model assuming a constant value of $A0 = A0, s = 1.01$, shows a strong dependence on the parameter ν, the rate of surface diffusion relative to bulk diffusion, for both (a) dissociative adsorption and (b) chemisorption-limited models. Arrows indicate the direction of phasor rotation and shifting low-frequency intercept with increasing values of $\nu = 0, 0.5, 1$, and 10. 63

Figure 3.9: The low-frequency real intercept of $U22$ and $U33$ is shown for both (a) dissociative adsorption, and (b) chemisorption rate laws, assuming $A0 = 1.01$ and parametric in $A0, s$. $U33$ shows an inversion of its trend with $A0, s$ at small values of ν. 64

Figure 3.10: The 2D dimensionless vacancy concentration profiles for $\chi 11$ (left), $\chi 22$ (middle), and $\chi 33$ (top) are evaluated at $\sigma = 0.01$ (top) and $\sigma = 100$ (bottom) with $\kappa = 1$, $\nu = 2$, and $A0, s = 1.01$. 67

Figure 3.11: The linear impedance response for the 2D model using a skin layer approximation shows a depression of the arcs from a true Gerischer shape upon increasing κ and ν. 68

Figure 3.12: The second (left) and third-order (right) voltage responses are predicted for (a) $\nu = 0.2$, (b) $\nu = 2$, and (c) $\nu = 20$. 69

Figure 4.1: A picture of a symmetric cell used in electrochemical testing shows LCF-91 working (identical counter not shown) and reference electrodes on a YSZ pellet. 72

Figure 4.2: SEM of (a) the electrode-electrolyte interface shows a cell thickness between 10-15 μm and good electrode contact to the YSZ, and (b) shows particle diameters ranging from 0.2-1 μm. 73

Figure 4.3: The elemental mapping from EDS based on the 20 kV SEM image in the top left shows a clear separation of electrolyte (Y, Zr) and electrode (La, Ca, Fe) species at the interface. 74

Figure 4.4: The NLEIS setup consists of a Probostat housing the gas and electrical feed-throughs to the cell, connected to a potentiostat applying a current waveform (generated by a National Instruments PCI-5421) and measuring the voltage response (sent to an NI PCI-5122 High-Speed Digitizer). 76

Figure 4.5: The EIS spectra at 0.01, 0.21, and 0.01 atm O_2 are shown at (a) 700, (b) 750, and (c) 800°C. 79

Figure 4.6: Measured values of (a) Rc show a weak decrease with increasing p_{O_2} and (c) strong thermal activation (~ -220 kJ/mol). (b) The peak frequency ωc shows a strong increase with increasing p_{O_2}, while (d) $Cchem$ shows a strong inverse dependence on p_{O_2}. 80

Figure 4.7: The distance that the active region of the electrode from the triple phase boundary, $L\delta$, estimated from changes in bulk nonstoichiometry, is compared to the average electrode particle diameter. 82

Figure 4.8: The degree of "flattening" of the observed spectra relative to that predicted by a 1D model, defined in the inset, is reported for all conditions. No attempt is made to remove the high-frequency features shown in Figure 4.5 from the arc width. 82

Figure 4.9: The characteristic resistance, Rc, and frequency, ωc, of a particularly transient LCF|YSZ cell is monitored over 800 hours in 700°C upon cycling $pO2$. 83

Figure 4.10: Measuring the impedance over long periods of time and varying $pO2$ reveals a strong connection between tc and Rc. 84

Figure 4.11: The measured nonlinear impedance response at p_{O_2} of 1 (red), 0.21 (green), and 0.01 atm (blue) for (a) 700°, (b) 750°, and (c) 800°C, with arrows indicating trends of phasor line rotation and magnitude shifts with increasing p_{O_2}. 86

Figure 4.12: The measured $U22$ spectra (points, dashed lines) in 1% (blue), 21% (green), and 100% (red) 02 environments are compared to modeled results (solid lines) assuming $\nu = 0$, $A0, s = A0$, and either chemisorption (left) or dissociative adsorption (right) rate laws. 88

Figure 4.13: $U22$ for the 1D model (solid lines) is fit to the measured spectra (points, dashed lines) in 1% (blue), 21% (green), and 100% (red) 02, by varying ν but fixing $A0, s = A0$ for both chemisorption (left) and dissociative adsorption (right) rate laws. 88

Figure 4.14: The model assuming surface interstitial diffusion and a chemisorption rate law (solid lines) is fit to the measured spectra (dashed lines) at 1% (blue), 21% (green) and 100% O_2 by varying ν and $A0, s$. 90

Figure 4.15: The model assuming surface interstitial diffusion and a dissociative adsorption rate law (solid lines) is fit to the measured spectra (dashed lines) at 1% (blue), 21% (green) and 100% O_2 by varying ν and $A0, s$. 91

Figure 4.16: The best-fit values of (a) ν and (b) $A0, s$ corresponding to Figure 4.15 are reported as a function of $pO2$ at 700, 750, and 800°C, with the expected $pO2$ dependence of ν shown for comparison. 92

Figure 5.1: A picture of a symmetric cell used in electrochemical testing shows LSCF working (identical counter not shown) and reference electrodes on a GDC pellet. 96

Figure 5.2: SEM of the electrode-electrolyte interface shows a cell thickness between 4-6 μm, good electrode contact to the GDC, and particle diameters ranging from 0.1-1 μm. 97

Figure 5.3: The EIS spectra at 0.01, 0. 1, and 0.01 atm O_2 are shown for (a) 550, (b) 600, and (c) 650°C 99

Figure 5.4: Measured values of the characteristic resistance Rc show (a) a weak decrease with increasing p_{O_2} and (b) thermal activation of ~ -65—-94 kJ/mol. 100

Figure 5.5: (a) The peak frequency ωc shows a strong $pO2n$ dependence where $n \approx 0.77 - 0.88$, (b) which is compared to the predicted dependence of equilibrium exchange rates for chemisorption (dashed red line) and dissociative adsorption (dashed blue line) rate laws. 101

Figure 5.6: By relating (a) the measured chemical capacitance of the elec trode to changes in bulk nonstoichiometry, (b) the length of the active region of the electrode from the triple phase boundary ($L\delta$) is estimated and compared to observed electrode particle diameters. 102

Figure 5.7: The measured second (left) and third-order (right) nonlinear response at p_{O_2} of 0.01 (blue), 0.1 (green), and 1 atm $O2$ (red) is shown at (a) 500, (b) 550, and (c) 650°C. 103

Figure 5.8: The simplest modelling scenario (solid lines) neglecting surface diffusion ($\nu = 0$), fixing the surface thermodynamics to measured bulk values ($A0, s = A0$) and assuming either a chemisorption (left) or dissociative adsorption (right) rate law is compared to measured $U22$ (dashed lines) at 650°C for 1% (blue), 10% (green), and 100% $O2$(red). 105

Figure 5.9: $U22$ (left) and $U33$ (right) assuming $\nu > 0$, $A0, s > A0$, and a chemisorption rate law (model, solid lines) is fit to data (dashed lines) for $pO2$ of 0.01 (blue), 0.10 (green), and 1 atm (red) and 550 (top), 600 (middle), and 650°C (bottom). 107

Figure 5.10: $U22$ (left) and $U33$ (right) assuming $\nu > 0$, $A0, s > A0$, and a dissociative adsorption rate law (model, solid lines) is fit to data (dashed lines)

for $pO2$ of 0.01 (blue), 0.10 (green), and 1 atm (red) and 550 (top), 600 (middle), and 650°C (bottom).....108

Figure 6.1: The thermodynamic state (T, $p_{O2,eff}$) of various H_2-H_2O blends (solid lines) is compared to that of LCF-91 at values of constant nonstoichiometry (dashed lines). 113

Figure 6.2: The predicted scaled linear voltage response, $U11$, is given for $A0 = 1.01$ and varying values of tv(vacancy transference number) and κ (scaled surface reaction rate). 117

Figure 6.3: Predicted transport properties of LCF-91 based on measured values for LSF-91 [12], [29]..... 118

Figure 6.4: The NLEIS setup used for H_2-H_2O analysis is identical to that used for O_2 studies, with the addition of a temperature-controlled humidifier and gas blending system.....120

Figure 6.5: Cross-sectional SEM of the LCF-YSZ electrode-electrolyte interface.....121

Figure 6.6: XRD of a 50-50 wt% LCF-YSZ pellet exposed to a 10:1 H_2-H_2O blend at 850°C for 87 hours. 122

Figure 6.7: The linear impedance data measured in a 2.8% H_2 and 1.4% H_2O blend at 750°C shows a strong time variance in two high-frequency features over 8 days. 124

Figure 6.8: The characteristic (a) resistance, (b) frequency, and (c) capacitance for the half-cell shown in Figure 6.7 are tracked over 200 hours of exposure to a 2.8% H_2 and 1.4% H_2O gas blend at 750°C. 125

Figure 6.9: The second and third harmonic NLEIS spectra are shown for a 2.8% H_2 - 1.4% H_2O blend at 750°C after 193 hours of exposure. Phasor lines indicate the peak frequency of the low-frequency feature ($\omega 1$), and labeled frequencies near the origin indicate the highest frequency resulting in a measurable nonlinear response. 126

Figure 6.10: The full-cell impedance of the LCF-YSZ cell is measured in air (left) before and after exposure to two reducing gases (right). 127

Figure 6.11: EIS measurements of a dense pellet of LCF with gold mesh current collectors exposed to both (a) oxidizing and (b) reducing conditions.....128

Figure 6.12: EIS measurements of a dense pellet of LCF with gold-painted current collectors exposed to both (a) oxidizing and (b) reducing conditions.....129

Figure 6.13: Full-cell EIS measurements of an LCF-YSZ button cell with gold-painted current collectors performed before, during, and after switching from air to H_2-H_2O at 750°C. 130

Figure 6.14: The characteristic (a) resistance and (b) capacitance of both the high and low frequency features shown in Figure 6.13 are monitored over 80 hours in a 49% H_2 – 1.2% H_2O environment. 130

List of Tables

Table 1.1: Typical gas composition exiting a biomass-fed steam gasifier at 870°C [10]. 3

Table 2.1: Comparison of the standard reaction enthalpies to those found in the literature. The reported error corresponds to a 99% confidence interval for the linear regression analysis and includes one standard deviation of the error in fitting the equilibrium constants shown in Figure 2.6. The fitted values for ΔS_{ox}^{0}, ΔS_{r}^{0}, and ΔS_{i}^{0} for LCF-91 are -94, 34, and -55 J/molK, respectively. 33

Table 3.1: The 1D macrohomogeneous model is nondimensionalized using the above dimensional groups. 53

Table 3.2: Microstructural parameters appearing in the 2D cylindrical model are defined in terms of those appearing in the 1D macrohomogeneous. 54

Table 3.3: The 2D cylindrical model is nondimensionalized using the above dimensional groups. 56

Table 6.1:Definitions of the dimensionless variables and parameters used in the 1D macrohomogeneous model. 116

1. Introduction

1.1 SOLID OXIDE FUEL CELLS AND ELECTROLYSIS CELLS

Increasing global fuel consumption, coupled with the limited supply of fossil fuels and the environmental and political drawbacks associated with them, has shifted the focus of energy research to more efficient and sustainable conversion and storage technologies. High temperature solid oxide fuel cells (SOFCs) and electrolysis cells (SOECs) potentially facilitate efficient, decentralized, and environmentally sustainable interconversion of electricity and carbon-containing fuels.

The working principle behind both SOFCs and SOECs is shown in Figure 1.1. Both cells consist of two predominantly electronically conducting electrodes separated by a purely ionic oxygen-conducting ceramic electrolyte, typically doped zirconia or ceria for their stability and high ionic conductivity [1]. In the case of a SOFC, an oxygen-containing stream (typically air) is reduced at the cathode and a reducing fuel stream (typically containing H_2) is oxidized at the anode. The large chemical driving force between fuel and oxidant drives the two half-cell reactions—oxygen ions through the electrolyte, and electrons through an external load—generating electrical work, avoiding the intermediate conversion of heat to mechanical work required by classical combustion techniques.

Conversely, for an SOEC, applied electrical work drives the thermodynamically "uphill" reduction of an oxidized fuel (typically H_2O or CO_2) to a high-grade fuel (H_2, CO) at the cathode, generating pure oxygen at the anode. The application of SOECs can range from hydrogen and synthetic fuel generation from renewable energy sources to on-site energy storage and fuel upgrading [2].

Current SOFC anode research includes the reduction of fuels including H_2, syngas, natural gas, landfill gas, and light hydrocarbons at temperatures ranging from 500-1000°C [3], [4]. The high operating temperatures and exothermic nature of SOFCs allow for efficient integration into combined heat and power plants [4]. One major concern for pure hydrogen SOFC applications is where to get pure hydrogen sustainably: approximately 95% of hydrogen generation derives from partial oxidation or steam reforming of coal and natural gas [5].

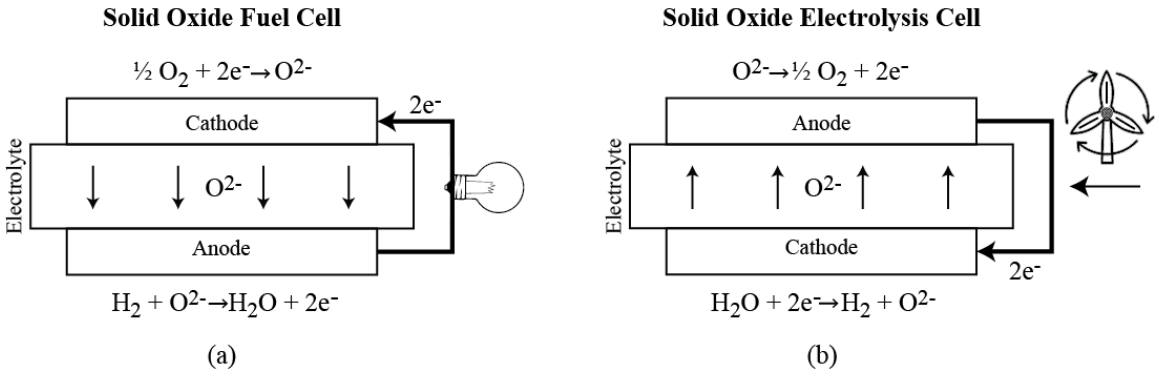

Figure 1.1: The working principle behind (a) SOFCs and (b) SOECs is shown for the simplified case of O_2 and H_2-H_2O streams.

A potentially renewable supply for SOFCs is the syngas (H_2, CO, H_2O, CO) resulting from gasification (partial oxidation) of cellulosic biomass [6]. Biomass gasification integrates well with existing coal gasification infrastructure, while containing significantly less sulfur detrimental to many electrode materials [7]. However, compared to coal, biomass is a heavily oxygenated fuel source, resulting

in a syngas with higher concentrations of H_2O and CO_2, especially in the case of steam gasification [8], illustrated by Table 1.1.

This syngas stream typically goes through a series of lower temperature water-gas shift reactors to increase the H_2 concentration with the penalty of generating more CO_2, which requires prohibitively expensive amine separation [7], [9]. The sum of these unit operations between gasification and syngas consumption amounts to oxygen separation.

Biomass Gasifier Product	**Yield** (mol%)
H_2O	46%
H_2	13%
CO_2	7%
CO	23%
CH_4	8%
C_2-C_6	<3%

Table 1.1: Typical gas composition exiting a biomass-fed steam gasifier at 870°C [10].

Figure 1.2 presents an alternative method where a low-grade, heavily oxygenated fuel (such as biomass-derived syngas exiting a gasifier) is partitioned into two streams across an SOEC. An applied potential reduces the top stream into an upgraded fuel, rich in H_2 and CO, with the potential for liquid-fuel conversion via Fischer Tropsch synthesis [7]. The second stream acts as both an oxygen sink for the first stream and a fuel source for a parallel SOFC, partially driving the SOEC or providing additional electricity. The open circuit voltage of a typical H_2/H_2O stream versus air at intermediate temperatures (500-800°C) is around -1 to -1.2 V, all of which must be overcome to drive the SOEC. An advantage of the SOEC in Figure 1.2 is its nominal equilibrium potential of 0 V (for two identical streams); compared to a typical fuel|O_2 SOEC, this operation is closer to being reversible,

avoiding the losses associated with oxygen generation at the anode. Additionally, this arrangement allows flexible adjustment between the relative amount of SOEC fuel upgrading and storage when excess power is available (potentially from an intermittent source) versus low-grade SOFC fuel conversion when electricity is required.

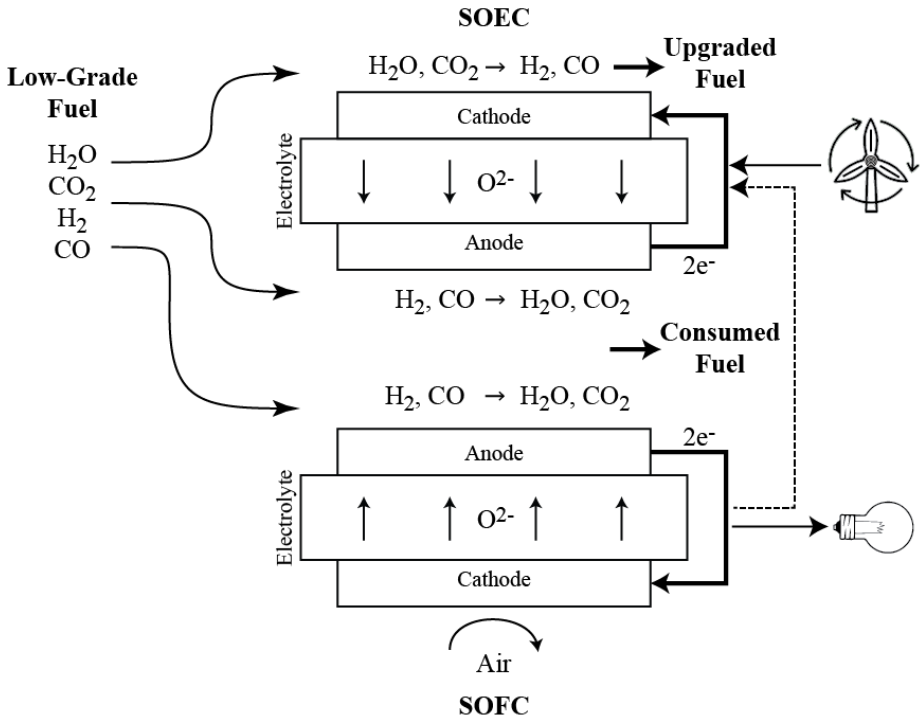

Figure 1.2: A potential application of a combined solid oxide electrolysis and fuel cell system which simultaneously functions as both a fuel upgrader and electricity generator depending on the demand for each.

A principal engineering challenge for both SOFCs and SOECs is to reduce the operating temperature from >1000°C to 500-800°C, allowing for the use of lower cost interconnect materials (e.g. stainless steel) and increased durability without significantly decreasing the overall performance. Due to the higher activation energy of the electrode processes relative to the electrolyte and the push towards using thinner electrolytes with electrode-supported cells, voltage losses from lowering the operating temperature originate primarily from the electrodes,

motivating both the search for new electrode materials and a better understanding of the phenomena controlling electrode performance [11].

1.2 MIXED-CONDUCTING PEROVSKITE ELECTRODES

The key design criteria for successful solid oxide electrodes include favorable electronic and ionic transport properties, low chemical expansion, thermal expansion compatible with that of the electrolyte, high catalytic activity, mechanical and thermodynamic stability across the full range of operating temperatures and gas environments, and low cost. Mixed ionic and electronic conducting (MIEC) perovskites, with the structure shown in Figure 1.3, meet these criteria and have been widely adopted as oxygen electrodes in both industry and research. Whereas classical, purely electronically-conducting electrodes limit electrochemical reactions (involving gaseous species, electrons, and ions) to the gas-electrode-electrolyte three-phase boundary (TPB), MIECs extend the active portion of the electrode by enabling ionic transport through the electrode.

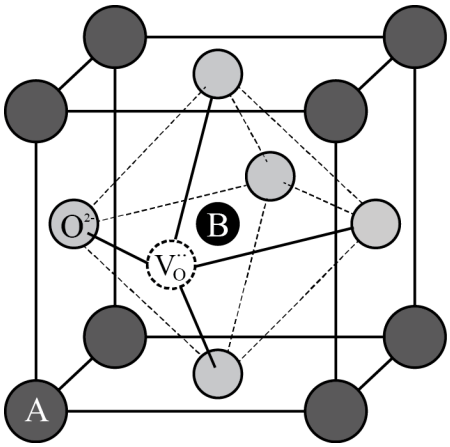

Figure 1.3: The perovskite crystal structure has a cubic unit cell of ABO_3, where A and B are typically rare earth or alkaline and transition metal cations, respectively.

On the fuel side (SOFC anodes, SOEC cathodes), the most common electrodes are based on cermets of Ni and yttria-stabilized zirconia (Ni-YSZ) and have a strong tendency to deactivate due to coking when exposed to carbon-containing

molecules such as those derived from biomass [12]. As an alternative, MIECs offer similar electronic and ionic transport properties as Ni-YSZ, while also being more resilient to carbon-containing atmospheres [12]. The development of SOFC cathodes has led to the discovery of numerous mixed conductors with high concentrations of catalytically-active oxygen ion vacancies under high partial pressures of oxygen (i.e. $p_{O2} > 10^{-3}$ atm O_2) [11]. While some of these materials (such as $La_{1-x}Sr_xCoO_{3-\delta}$) decompose under the low-p_{O2} conditions of a fuel electrode [13], others may fall in the correct window of thermodynamic stability for use in reducing environments.

1.2.1 Thermodynamic Properties

The most common mixed conducting perovskites consist of rare earth or alkaline metals at the A-site (La, Sr, Ca, etc.) and transition metal cations at the B-site (Fe, Co, Mn, Cr, etc.). Doping of the A-site with a cation of lower valency creates an intrinsic charge imbalance that must be compensated by the creation of positive oxygen vacancies and the reduction of the B-site metal. The creation of oxygen vacancies provides a pathway for ionic transport, while the B-site provides electronic conduction. Therefore, the thermodynamic relationship between the concentration of defect species and the temperature, surrounding gas environment, and dopant level must be understood to accurately study the kinetics and transport involving these electrodes.

The observed thermodynamic behavior of perovskite electrode materials can be largely understood by considering two well-studied extremes, shown in Figure 1.4: either where the measured oxygen stoichiometry $(3 - \delta)$ decreases from the fully stoichiometric state $(\delta = 0)$ with decreasing p_{O_2} to a plateau at one-half the intrinsic A-site doping (x) before continuing to decrease, as in the case of $La_{1-x}Sr_xFeO_{3-\delta}$ (LSF), or where the oxygen stoichiometry continuously decreases until decomposition, as in the case of $La_{1-x}Sr_xCoO_{3-\delta}$ (LSC) [13], [14]. The former scenario has been interpreted using a point defect theory where the B-site iron

changes from its average valency of Fe^{3+} at the plateau to Fe^{4+} upon increasing p_{O_2} (decreasing the number of oxygen vacancies) and to Fe^{2+} upon decreasing p_{O_2} (increasing the vacancy concentration) [14]. This transition between Fe^{2+}-Fe^{3+}-Fe^{4+} is analogous to a p-n transition in a semiconductor, with Fe^{4+} acting as localized holes and Fe^{2+} as electrons.

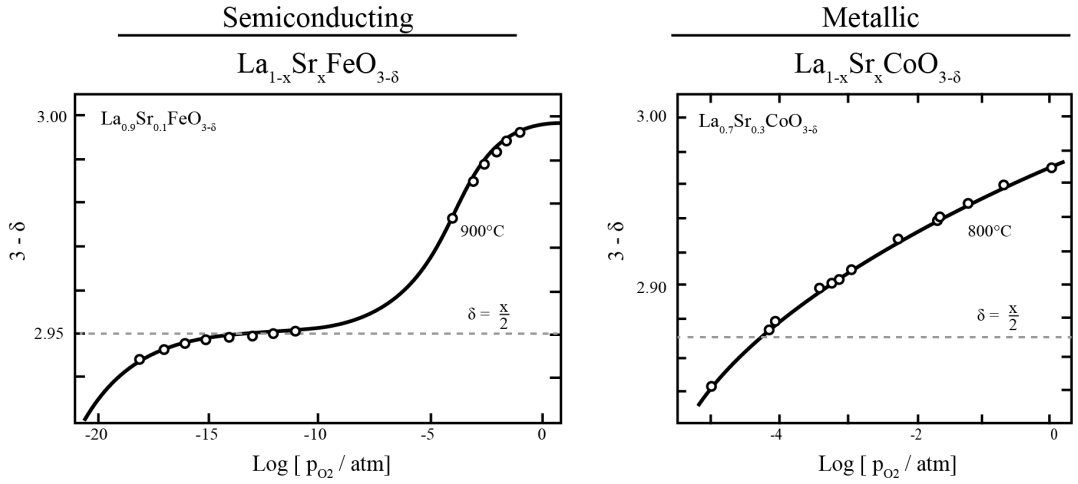

Figure 1.4: Perovskites of the form (a) $La_{1-x}Sr_xFeO_{3-\delta}$ show a plateau of oxygen stoichiometry, $3-\delta$, with changing p_{O_2} occurring at $\delta = \frac{x}{2}$, while (b) $La_{1-x}Sr_xCoO_{3-\delta}$ shows a continuous increase in nonstoichiometry with decreasing p_{O_2} (adapted from [13], [14]).

Alternatively, materials exhibiting the behavior shown in Figure 1.4b, such as $La_{1-x}Sr_xCoO_{3-\delta}$, have similarly been modeled using point defect theory, but instead treat electrons as having a delocalized, metallic structure [15]. In both cases, the vacancy concentration is observed to increase with decreasing p_{O_2} and increasing temperature.

In the case of a fuel electrode, decomposition of the material into its constituent oxides at low effective oxygen partial pressures limits its operating range. Even a 1:1 H_2-H_2O blend at 700°C corresponds to an *effective* p_{O_2} (the p_{O_2} that would be in equilibrium with a given p_{H_2} and p_{H_2O}) of ~10^{-21} atm, well below the decomposition limit of many mixed conducting oxygen electrodes, such as those based on LSC [13].

As a tradeoff between the high performance of LSC electrodes and the thermodynamic stability of LSF, $La_{1-x}Sr_xCo_{1-y}Fe_yO_{3-\delta}$ (LSCF), has gained interest as a potential oxygen electrode. Researchers have interpreted thermodynamic data for LSCF using both metallic (as in LSC) and semiconductor models (as in LSF); the former were more successful for Co-rich compositions, while the latter were more successful for Fe-rich compositions [16], [17]. For the composition $La_{0.6}Sr_{0.4}Co_{0.2}Fe_{0.8}O_{3-\delta}$ (LSCF-6428), as shown in Figure 1.5, a semiconductor model was found to be more consistent [16]. LSCF-6428 exhibits a compressed p-n transition and decomposition at higher p_{O_2} than its Co-free counterpart [18]. Because of the tendency of Co to decompose under reducing conditions, even for materials with low Co-doping such as LSCF-6428, the application of LSCF is typically limited to oxygen electrodes.

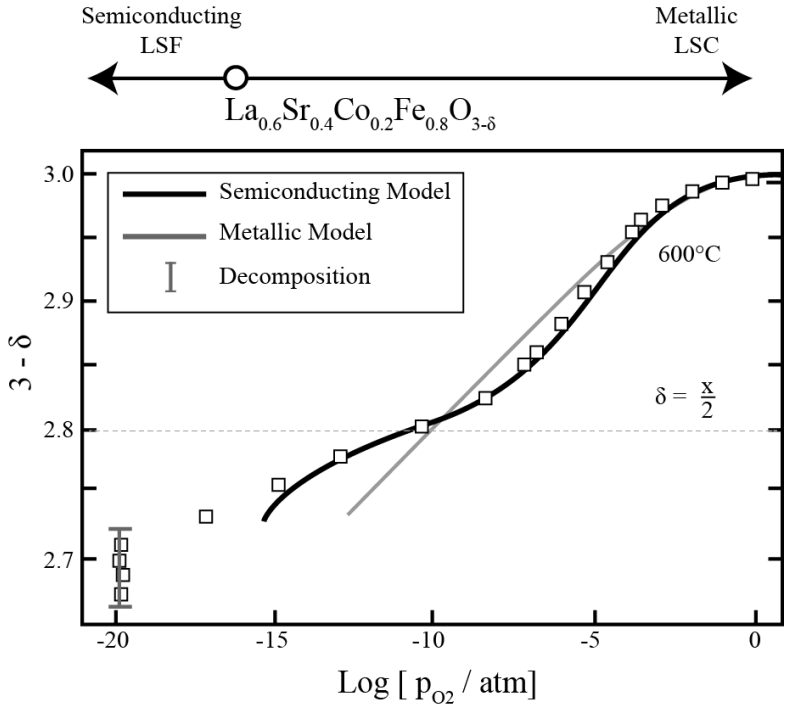

Figure 1.5: The observed thermodynamic behavior of $La_{0.6}Sr_{0.4}Co_{0.2}Fe_{0.8}O_{3-\delta}$ measured to decomposition, interpreted using both a metallic and semiconducting model (adapted from [16]).

The two materials studied in this work, $La_{0.9}Ca_{0.1}FeO_{3-\delta}$ (LCF-91) and $La_{0.6}Sr_{0.4}Co_{0.2}Fe_{0.8}O_{3-\delta}$ (LSCF-6428), are categorized alongside the semiconducting lanthanum ferrites represented in Figure 1.4a, and as such, much of the modeling and theory presented within is intended to be general to this class of mixed conductors. $La_{1-x}Ca_xFeO_{3-\delta}$, has predominantly been studied as an oxygen electrode, and therefore the thermodynamic understanding of the defect-p_{O_2}-temperature relationship for LCF is limited to either studies in air [19], or for $(La_{0.8}Ca_{0.2})_{0.95}FeO_{3-\delta}$ between 10^{-3}-1 atm O_2, where only p-type behavior has been observed [20], [21]. Additionally, LCF has been shown to be stable in reducing conditions and environments with high p_{CO_2}, supporting its possible application as either an oxygen or fuel electrode [22], [23].

In addition to an isolated material's thermodynamic stability, an electrode must show thermodynamic compatibility with an electrolyte, typically doped-zirconia.

LSCF electrodes, for example, are typically studied with a gadolinium-doped ceria (GDC) protective interlayer between the electrode and YSZ electrolyte, due to the risk of forming insulating phases such as lanthanum zirconate [24]. LCF electrodes were not observed to produce tertiary phases with YSZ electrolytes, though the possibility of cation incorporation between phases exists [25], [26].

1.2.2 Transport Properties

While the ionic conductivity of mixed conducting electrons can be significant, most are principally electronic conductors. In the limit of an electronic transference number approaching unity, the measured total conductivity, such as that from a four-probe DC method, shown in Figure 1.6a for LSF-91, approaches that of electronic conductivity. For semiconducting electrodes such as LSF and LCF, the total conductivity at p_{O_2} above the p-n transition is dominated by hole transport, while electron transport dominates at lower p_{O_2}. The total electrical conductivity reaches a minimum at the p_{O_2} corresponding to the center of the p-n transition shown Figure 1.4a, where the total concentration of Fe^{2+} and Fe^{4+} species is expected to be a minimum; at this point the electrical conductivity can drop to the order of the p_{O_2}-independent ionic conductivity [27]. For conditions of 600-800°C in air, LCF-91 appears to show an electrical conductivity (~10 $\Omega^{-1}cm^{-1}$) similar to that of LSF-91 [28]. Under these oxidizing conditions, both LCF-91 and LSCF-6428 are expected to have electronic transference numbers approaching unity.

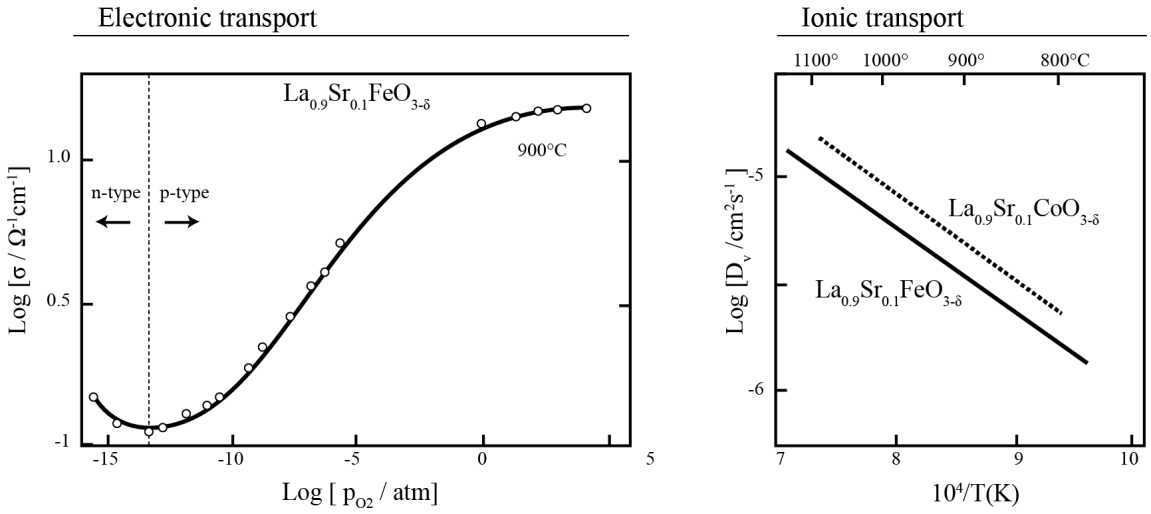

Figure 1.6: (left) The total electrical conductivity of LSF-91 shows a minimum at the center of its p-n transition, the plateau shown in Figure 1.4a (adapted from [29]). (right) The p_{O2}-independent vacancy diffusivity is inferred for LSF-91 and LSC-91 (adapted from [12]).

Bulk ionic transport in mixed conductors is assumed to follow that of moderately-dilute non-ideal systems, driven by gradients in electrochemical potential (μ_v), and scaling with vacancy concentration (c_v) [30],

$$N_v = -\frac{D_v c_v}{RT}\nabla\mu_v\,, \qquad 1.1$$

where N_v is the molar flux of vacancies and D_v is the vacancy diffusivity. Figure 1.6b shows the inferred vacancy diffusivity as a function of temperature for various mixed conducting electrodes in oxidizing environments. While the trend is not shown, the vacancy diffusivity, as defined by Eq. 1.1, is taken to be independent of p_{O2}. Also not shown, the ionic conductivity of LCF-82 was observed to be nearly an order of magnitude lower than that of LSF-82 at high p_{O2} and between 600-800°C [31].

In addition to an ionic pathway through the bulk of the electrode, the possibility exists for the transport of species along the surface of the microstructure—as in the cases of Pt and $La_{1-x}Sr_xMnO_{3-\delta}$ (LSM) electrodes [32], [33]. Lu *et al.* found that, while a predominantly bulk pathway was sufficient to model the linear impedance

response of porous LSC-64, a parallel surface path was required for the less nonstoichiometric LSC-82 [34]. Of the surface mechanisms considered, only one with an inverse dependence on vacancy concentration yielded sensible trends for D_v when fit to the data, leading Lu *et al.* to propose a surface model with itinerant interstitial oxygen species assumed to be in equilibrium with bulk vacancies. While this two-dimensional model was able to capture the linear response of LSC-82, it was unable to do so quantitatively for the full nonlinear response, leaving the exact role and mechanism of surface transport on mixed conducting electrodes incompletely understood.

1.3 ELECTRODE KINETICS

1.3.1 Oxygen Reduction on Mixed Conducting Electrodes

The overall oxygen reduction reaction, given below in Kröger-Vink notation, involves oxygen in the gas phase consuming two bulk oxygen vacancies ($V_{\ddot{O}}$) and four electrons (e') to produce two filled oxygen sites (O_O^x).

$$O_2(g) + 2V_{\ddot{O}} + 4e' \rightleftharpoons 2O_O^x \qquad 1.2$$

In the case of porous mixed conducting oxygen electrodes, cells are rarely limited by purely kinetic processes. Instead, these materials usually exist in a regime co-limited by both reaction and diffusion phenomena [35]. Because of this, any reported of kinetic rate relies on some degree of modeling or interpretation pertaining to the rate-determining behavior. Workers often report the kinetics of the above reaction as some form of equilibrium surface exchange rate, $\mathcal{R}_0$. Techniques used to measure this rate, such as conductivity relaxation or isotope exchange experiments performed at various temperatures and p_{O_2}, require interpretation through a reactive-diffusion model to separate the processes of overlapping timescales. Conductivity relaxation experiments on $La_{1-x}Sr_xCoO_{3-\delta}$ yielded a p_{O_2} dependence of $\mathcal{R}_0 \sim p_{O2}^n$ where n decreased with increasing Sr-doping (e.g. $n \approx$ 0.2-0.6 for LSC-82, 0.7-1.0 for LSC-64), however, this dependence was

observed to greatly weaken upon reaching the conditions of lowest vacancy concentration (i.e. $x = 0.2$, $p_{O2} > 0.1$ atm, and low temperatures). $La_{1-x}Sr_xFeO_{3-\delta}$ showed a more constant trend of $n \approx 0.5$-1.0, even at high p_{O_2} [36], [37].

For these experiments, large changes in temperature and p_{O2}—typically over long periods of time—are required in order to infer the nonlinear nature of the oxygen reduction process, therefore allowing different rate-limiting phenomena to be distinguished. However, these indirect measurements of electrode nonlinearities are convoluted with secondary processes affecting electrode performance, such as decomposition and long-term equilibration processes. More recent work has begun to probe the nonlinear impedance behavior of MIEC electrodes, suggesting that a dissociative adsorption-limited mechanism (discussed in later chapters) is consistent with the observed nonlinear response of oxygen reduction on LSC-64 and LSC-82 electrodes [38], [39]. Compared to LSC, the oxygen reduction mechanism for LCF or LSCF is even less understood.

1.3.2 Fuel Kinetics

The vast majority of literature on H_2-H_2O kinetics on SOFC anodes is based on Ni-YSZ cermets. Conduction is typically assumed to be purely electronic through Ni and purely ionic through YSZ, limiting charge transfer reactions to the gas-electrode-electrolyte triple phase boundary. However, for porous cermet anodes, this region can extend large distances from the electrode and is sensitive to slight variations in manufacturing or sintering conditions. To overcome this, a large portion of quantitative H_2-H_2O studies on Ni-YSZ use well-characterized, micro-patterned thin-film Ni electrodes on dense YSZ [40]–[43]. While not directly applicable to mixed conducting electrodes, elementary mass-action kinetic and surface diffusion models based on these electrodes provide insight into the relevant surface species, mechanisms, and transport and kinetic parameters [40], [44]. Ni-YSZ has also been studied in the context of CO-CO_2 exchange, but has shown poor activity toward CO_2; in the case of co-electrolysis of CO_2/H_2O on Ni-

YSZ, CO_2 reduction is thought to occur predominantly through water-gas shift equilibrium with H_2/H_2O [45]–[48].

Mixed conductors have gained interest as SOFC anodes and SOEC cathodes because of some limitations of Ni-YSZ-based electrodes: particularly, activity towards carbon deposition in hydrocarbon environments, sensitivity to sulfur poisoning, and instability in oxidizing environments [49]. A variety of perovskite and fluorite compositions have been studied, including doped lanthanum chromites and manganites [50]–[52] and doped ceria [53], [54]. However, the focus of most mixed conducting fuel electrode research is on overall cell performance as a function of cell composition and gas environment, leaving the mechanistic understanding of the rate determining phenomena under-developed.

1.4 ELECTROCHEMICAL IMPEDANCE TECHNIQUES

Both linear and nonlinear electrochemical impedance spectroscopy (EIS, NLEIS) allow for the separation of rate-determining phenomena by timescale. The former technique, well-established in the field, considers only the *linear* response to a small sinusoidal (current or voltage) perturbation of varying frequency; the impedance at a given frequency is characteristic of physical processes occurring at timescales of 1/frequency. However, many of the electrode phenomena of interest, such as kinetic rate laws, are *nonlinear*, yet when linearized produce indistinguishable responses. Therefore, the majority of electrochemical techniques used to probe rate-limiting phenomena (such as EIS, or conductivity relaxation experiments), require large changes in temperature and p_{O2}—typically over long periods of time—in order to infer the nonlinear nature of the oxygen reduction process, therefore allowing different phenomena to be distinguished. These indirect measurements of the electrode nonlinearities are convoluted with secondary processes affecting electrode performance, such as decomposition and long-term equilibration.

NLEIS extends EIS to larger amplitude perturbations capable of exciting these characteristic nonlinearities, increasing the near-equilibrium perturbations typical for EIS to driving forces more representative of SOFC/SOEC operating conditions. This provides a direct measurement of the nonlinear electrode behavior. NLEIS has been used to provide insight regarding the nature of the oxygen reduction mechanism on $La_{1-x}Sr_xCoO_{3-\delta}$ porous and thin-film electrodes [39].

Whereas EIS studies typically express the linear impedance, $Z(\omega)$, as a complex function parametric in perturbation frequency, ω, NLEIS captures the nonlinear impedance using dimensionless second and third-order Fourier voltage coefficients, $U_{22}(\omega)$ and $U_{33}(\omega)$, tied to the second and third voltage harmonics resulting from a current perturbation, $i = \tilde{\imath}\, cos(\omega t)$, formally defined in ref. [39]. Figure 1.7 illustrates these two techniques, and presents example spectra using Nyquist plots parametric in perturbation frequency.

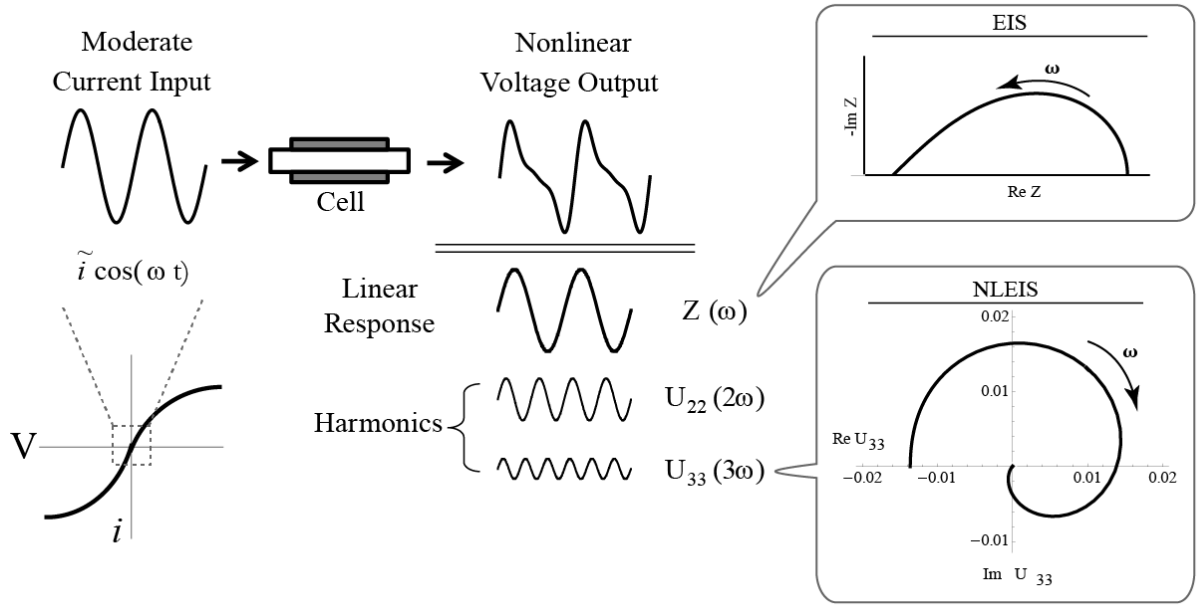

Figure 1.7: NLEIS and EIS techniques are qualitatively illustrated, and example spectra for each are shown on the right.

1.5 PRESENT WORK

The primary goal of the work presented in this dissertation is to improve the understanding of the rate-limiting phenomena affecting the performance of semiconducting MIEC electrodes in both oxidizing and reducing conditions. Two materials, $La_{0.9}Ca_{0.1}FeO_{3-\delta}$ and $La_{0.6}Sr_{0.4}Co_{0.2}Fe_{0.8}O_{3-\delta}$ were selected as candidate electrodes; the former for its stability in both oxidizing and reducing conditions, and the latter for its high performance as an air electrode.

In order to interpret the electrochemical behavior of these electrodes, a thorough understanding of the material's thermodynamics is required, particularly how its defect chemistry (affecting kinetic and transport phenomena) responds to changes in cell environment. While a large body of thermodynamic data has been collected for LSCF, minimal measurements exist for LCF. Chapter 2 presents coulometric titration data, measuring changes in the oxygen nonstoichiometry of

LCF-91 across a wide range of temperature and p_{O2}, and interprets these results using a point-defect model.

Using this defect model, Chapter 3 presents a porous electrode model general to p-type MIECs, considering various thermodynamic, kinetic, and transport assumptions. Both one-dimensional analytical and two-dimensional numerical formulations are given. Chapters 4 and 5 compare linear and nonlinear electrochemical impedance results collected at various temperatures and oxygen environments for LCF-91 and LSCF-6428, respectively, to those predicted in Chapter 3.

Chapter 6 presents the linear and nonlinear impedance spectra of LCF-91 electrodes in reducing hydrogen-water environments. This chapter focuses on the difficulties, both thermodynamic and transport-related, that arise when studying n-type MIECs under these conditions. Chapter 7 summarizes the results of this dissertation.

2. Oxygen Nonstoichiometry and Defect Chemistry of $La_{0.9}Ca_{0.1}FeO_{3-\delta}$

The equilibrium oxygen nonstoichiometry, δ, for the mixed ionic and electronic conducting perovskite $La_{0.9}Ca_{0.1}FeO_{3-\delta}$ (LCF-91) was measured for oxygen partial pressures, p_{O_2}, between 10^{-3} and 10^{-21} atm and temperatures of 750 to 900°C using a tubular, two-probe Pt|YSZ|LCF coulometric titration cell. X-ray diffraction experiments confirmed that LCF-91 remains a single phase perovskite under the reducing conditions of a fuel electrode, and reveal no evidence of reaction with the zirconia electrolyte. The p_{O_2}-nonstoichiometry relationship was interpreted using a dilute-solution point-defect model, and the resulting equilibrium constants were reported.

2.1 BACKGROUND

$La_{1-x}Ca_xFeO_{3-\delta}$ (LCF), while not very active as an oxygen electrode [31], potentially offers favorable ionic and electronic transport properties under reducing conditions, as well as low chemical expansion, adjustable thermal expansion, and low rates of creep under mechanical stress.[23], [28] In this study, a low calcium doping ($x = 0.1$) was selected to avoid secondary phase formation at the expense of ionic conductivity. LCF has been studied previously as an oxygen separation membrane[23], [28], [55], and as a methane, hydrogen, carbon monoxide, and soot

oxidation catalyst [56]–[60]. LCF's crystallographic properties, thermal expansion, and ionic and electronic conductivity are also known.[21], [28], [61]–[63]

Interpretation of electrochemical kinetic studies of LCF as a fuel electrode requires knowledge of the equilibrium relationship between electronic and ionic defect concentrations and the effective p_{O_2} of the fuel stream. However, published thermogravimetry and conductivity studies of $(La_{0.8}Ca_{0.2})_{0.95}FeO_{3-\delta}$, have focused on oxidizing (cathodic) conditions ($p_{O_2} = 10^{-3} \sim 1$ atm).[20], [21] Understanding the performance of this material under the reducing environment of a renewable fuel stream ($p_{O_2} \sim 10^{-20}$ atm) requires acquisition of a wider range of thermodynamic data at the specific doping levels of interest.

2.2 COULOMETRIC TITRATION

Coulometric titration can be used to relate the oxygen nonstoichiometry, δ, of an $ABO_{3-\delta}$ perovskite sample to the p_{O_2} in equilibrium with it. In its most basic form illustrated in Figure 2.1, this technique consists of a sealed cell containing the oxide sample, separated from a reference electrode by an oxygen-conducting electrolyte. Holding the inner electrode at constant potential forces oxygen into or out of the sample until the sample reaches its equilibrium oxygen nonstoichiometry. Assuming the electrolyte is a pure ion conductor, the p_{O_2} in equilibrium with the sample can be determined by measuring the equilibrium (Nernst) potential:

$$V = \frac{RT}{4F} \ln \left[\frac{P_{O2}}{P_{O2}^{ref}} \right], \qquad 2.1$$

where p_{O2}^{ref} is the oxygen partial pressure of the reference electrode and F is Faraday's constant. This provides a measurement of the sample's oxygen activity, even at the extremely low p_{O_2} of interest in this study.

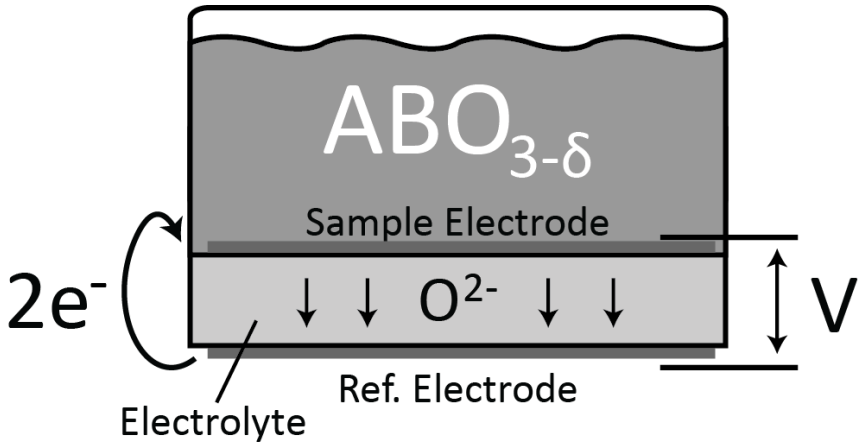

Figure 2.1: Diagram of the working principle behind coulometric titration for the perovskite sample $ABO_{3-\delta}$.

The flux of oxygen into or out of the cell resulting from changes in the sample's oxygen stoichiometry can be precisely measured as a Faradaic current, making this technique ideal for samples with low oxygen nonstoichiometry, such as $La_{0.9}Ca_{0.1}FeO_{3-\delta}$ [64]. However, even for a perfectly sealed cell, the oxygen electrolyte, typically doped zirconia, possesses minor electronic conductivity at elevated temperatures and large p_{O_2} driving forces, resulting in an ambipolar flux of oxygen ions and electrons through the electrolyte at open circuit conditions [65]. For experiments with long equilibration times and small changes in oxygen stoichiometry, this leak current can account for a significant portion of the total measured current [64]. When potentiostatically controlling the cell, the measured equilibration current will decay to the leak current at steady state, making identification of the leak rate straightforward (as opposed to galvanostatic operation). At potentiostatic steady state, the applied potential suppresses transport of oxygen vacancies, resulting in a purely electronic flux through the electrolyte. Heyne shows for this scenario of suppressed permeation, even at significant leak currents, the applied voltage is purely Nernstian upon reaching steady state, given by Eqn. 2.1 [66].

Integrating the current response, *I(t)*, over the equilibration time, neglecting changes in the amount of oxygen in the dead volume of the cell, yields the change in oxygen nonstoichiometry, δ, for a potentiostatic step, [67]

$$\Delta\delta = \frac{M}{2Fm_{sample}}\int_0^\infty [I(t) - I_{ss}]\,dt \qquad 2.2$$

where M is the molecular weight of the oxide at $\delta = 0$, m_{sample} is the sample mass at δ = 0, and I_{ss} is the steady-state leak current, assumed to remain constant throughout each voltage step (discussed later in this chapter).

2.3 EXPERIMENTAL

2.3.1 LCF Samples

The $La_{0.9}Ca_{0.1}FeO_{3-\delta}$ powder studied in this work was fabricated by Air Products and Chemicals, Inc. via solid-state reaction. Powders of lanthanum oxide, calcium carbonate, and iron oxide were blended, then calcined at 1190°C for 10 hours. The resulting coarse powder was subsequently milled via hammer, attrition, and vibratory processes resulting in a surface area of approximately 6 m^2/g. This fine powder was fired at 1200°C for 36 hours and then cooled to room temperature over a period of 12 hours to ensure equilibration with air.

A portion of the powder was mixed with organics (α-terpineol, ethyl cellulose, oleic acid) and milled, resulting in an electrode ink with 50% solids loading. To determine the optimal LCF sintering conditions, the LCF ink was screen printed onto YSZ pellets and sintered at various temperatures (1000~1150°C). The cross section of the LCF-YSZ interface was then observed via SEM. The best electrode firing temperature (1050°C) resulted in a well-adhered electrode with uniform fine porosity and particle necking.

2.3.2 Coulometric Titration Cell

While various implementations of coulometric titration have been reported in the literature [64], we employed a tubular two-electrode cell, as illustrated in Figure

2.2. The cell consisted of a dense closed-end yttria-stabilized zirconia (YSZ) tube, with a Pt reference electrode on the outside surface (exposed to air), and a sealed inner electrode made from the sample material itself. The open end of the tube (which sits outside the furnace) was attached using a Viton o-ring compression seal to a gas manifold with positive shut-off valve and electrical feedthrough for a wire to the inner electrode.

As shown by Mizusaki *et al* [68], this approach has two principle advantages over other designs [69]. First, the sample itself acts as the inner electrode, allowing direct monitoring of the sample's electrochemical potential and providing a continuous solid-state pathway for oxygen ion transport, thereby avoiding limitations imposed by gaseous diffusion of O_2 at low p_{O_2}. Secondly, the long tubular geometry allows all gas seals to remain at room temperature, avoiding the use of high-temperature seals.

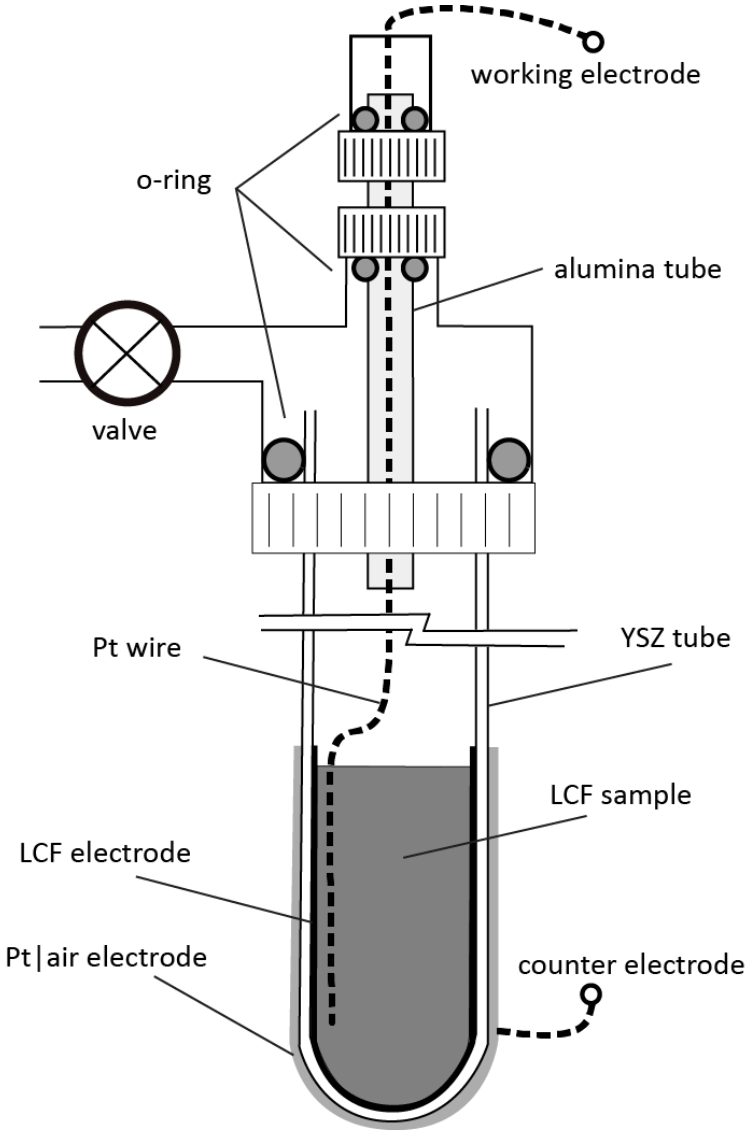

Figure 2.2: Schematic of the sealed, two-probe, coulometric titration cell, where the LCF sample is maintained at constant temperature.

In our implementation, the closed-end YSZ tube (10.5 mol% yttria) was 30 cm long and had a diameter of 0.64 cm. The LCF ink was painted on the inside bottom 4 cm of the YSZ tube using a narrow brush and sheath, and sintered at 1050°C for 30 minutes to act as the inner electrode. An equal length of Pt ink (Engelhard, A6016XD) was painted on the outside of the YSZ tube and fired at 1000°C to act as the outer air electrode. A current-collecting wire (platinum or gold) was placed in the empty tube. Approximately 2 g of loose LCF powder was ground, weighed in

air, then funneled and packed into the bottom of the YSZ tube, ensuring good contact with both the LCF electrode and current-collecting wire. The sample mass was confirmed to be large enough to make changes in YSZ nonstoichiometry at low p_{O_2} negligible in comparison [70]. A helium leak detector was used to verify the integrity of the seals and gas-tightness of the electrolyte down to 10^{-11} atm before and after each experiment.

2.3.3 Coulometric Titration Method

Following initial heating in ambient air to the desired temperature, the two-probe titration cell was sealed and maintained at a series of equilibrium voltages (using a Solartron 1287A potentiostat) while the current was continuously recorded. Equilibrium with the applied potential was determined by measuring the current following establishment of a steady potential, and examining when the current reached a steady-state value (I_{ss}). Equilibration times varied from several hours to several days, depending primarily on cell temperature. The potential sweep usually began at -150 mV (sample electrode vs. air electrode), which corresponds to a low enough p_{O_2} that the amount of oxygen gas in the dead volume of the sealed cell is negligible compared to the lattice oxygen in the sample. Potential steps then proceeded in 50 mV increments of decreasing p_{O_2} until the full spectrum of the p_{O_2}-nonstoichiometry relationship was captured. The sweep direction was then switched, returning to the initial p_{O_2} to confirm thermodynamic reversibility. This procedure was then repeated for all cell temperatures.

2.3.4 X-Ray Diffraction

Powder X-ray diffraction (XRD) was performed *ex situ* on the LCF coulometry samples before and after measurements to test for additional phases using a Bruker AXS D8 Discoverer spectrometer with CuK_α radiation at an average wavelength of 1.54226 Å. One cell operating at 850°C was cooled 4 °C/min at its most reduced state (-1150 mV) before XRD testing, while the remainder of cells

were first returned to their high-p_{O_2} starting condition. Two additional tests were performed to verify the stability of LCF across all operating conditions. First, samples of well-mixed 50-50 wt% LCF and 8%-YSZ were pressed and sintered at 1200°C and 1050°C. The powder XRD pattern of these samples was then compared to that of an unfired mixture. Second, LCF was exposed to a gas blend of 20:1 H_2-H_2O by mass at 850°C for 48 hours, corresponding to the most reducing conditions studied via coulometry ($\delta \approx 0.06$), before examining phase purity using powder XRD.

2.4 RESULTS AND DISCUSSION

2.4.1 LCF Characterization and Stability

Figure 2.3 shows the cross-sectional interface of an LCF-YSZ pellet fired at 1050°C. The particle radii vary between 0.2–1.0 μm. Sintering at higher temperatures caused excessive joining of particles, closing off gas diffusion pathways. Sintering at lower temperatures did not provide adequate contact between the electrode and electrolyte.

Figure 2.4 compares the XRD spectra of 50-50 wt% LCF-YSZ pellets sintered at 1050 and 1200°C to that of an unfired sample. All peaks can be indexed to the ABO_3 perovskite electrode and 8%-YSZ, except for two peaks identified as ZrO_2—later confirmed to be a minor constituent of the electrolyte. As previously found by Anderson *et al.*, no insulating lanthanum or calcium zirconate phases were detected [25].

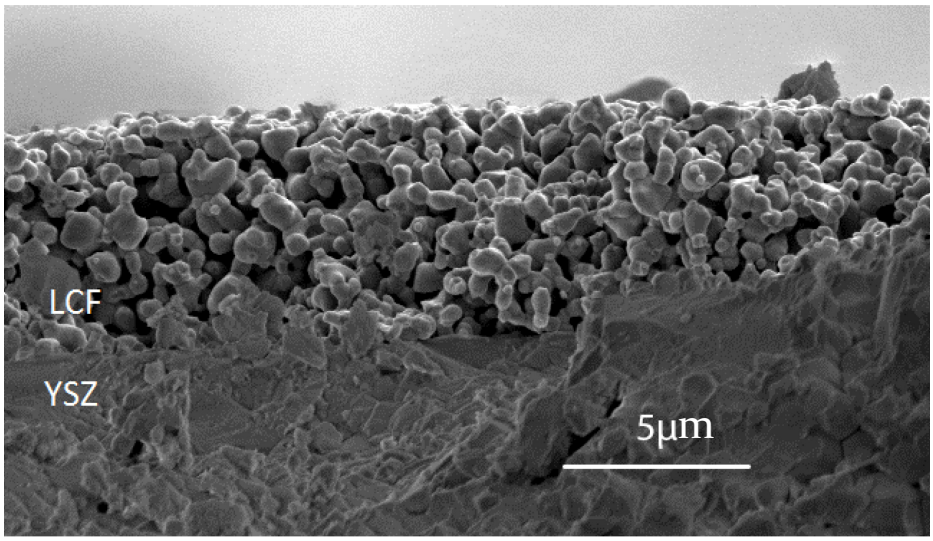

Figure 2.3: Cross-sectional SEM image of screen-printed LCF ink sintered at 1050°C on a YSZ pellet, showing good adhesion of the electrode to the electrolyte.

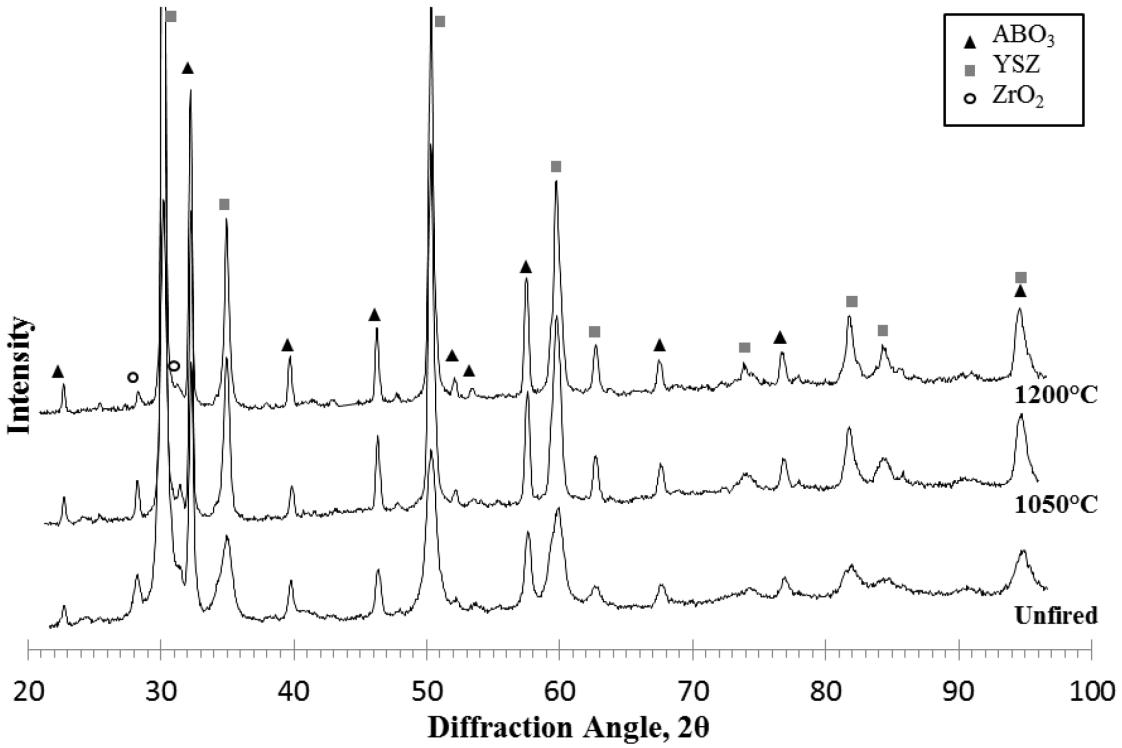

Figure 2.4: . XRD spectra of 50-50 wt% samples of LCF & YSZ unsintered, and sintered at 1050˚ and 1200˚C.

Figure 2.5 compares the XRD spectrum of LCF powder exposed to a reducing blend of 20:1 H_2-H_2O at 850°C for 48 hours to that exposed to air. In both samples, all peaks could be indexed to a perovskite structure. Additionally, XRD analysis of the post-coulometry samples, including the sample quenched at its most reduced state, showed only a perovskite phase. Thus, it appears that LCF is stable under the most reducing conditions reached during the coulometric titration measurements.

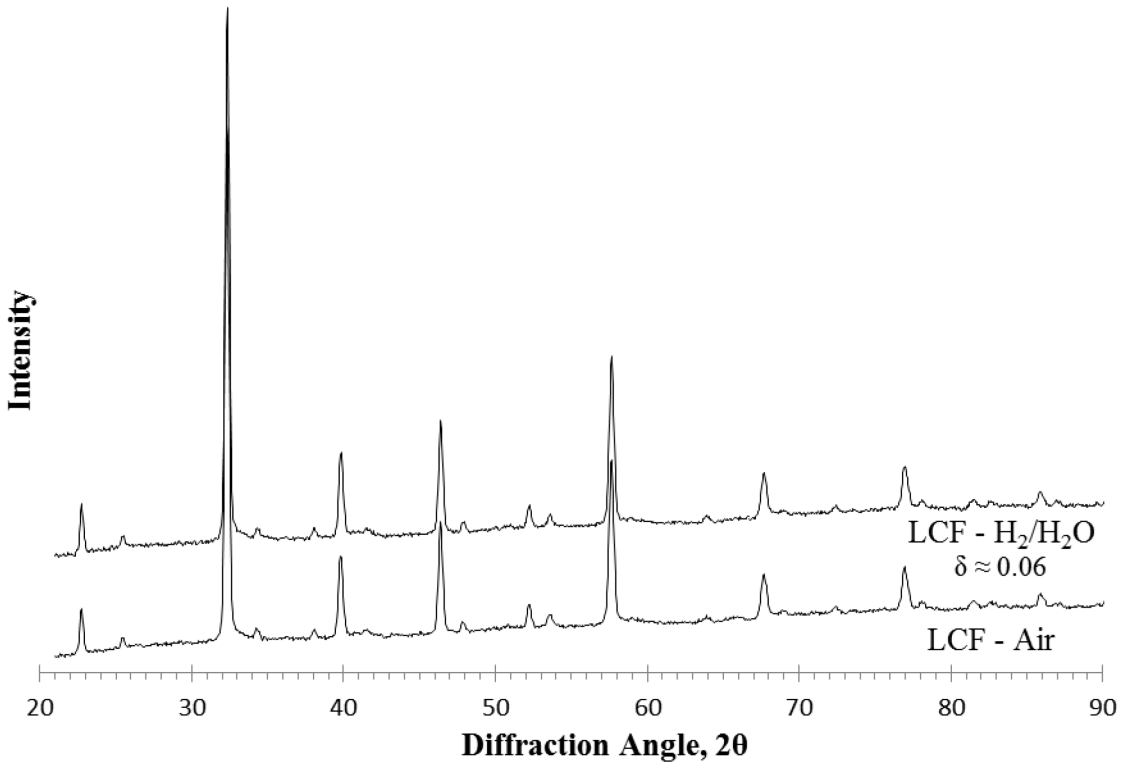

Figure 2.5: XRD spectra of two samples of LCF powder: one exposed to a 20:1 blend of H_2-H_2O at 850°C for 48 hours, the other exposed to air.

2.4.2 Oxygen Nonstoichiometry

Figure 2.6 shows the oxygen stoichiometry (3-δ) of $La_{0.9}Ca_{0.1}FeO_{3-\delta}$ (calculated from Eqn. 2.2) as a function of the p_{O_2} in equilibrium with it (calculated from Eqn.

2.1), measured at 750°, 800°, 850° and 900°C. Each temperature, except for 800°C, corresponds to an independent sample and titration cell. Replicate sweeps on unique cells were performed at 850 and 900°C but not shown in Figure 2.6.

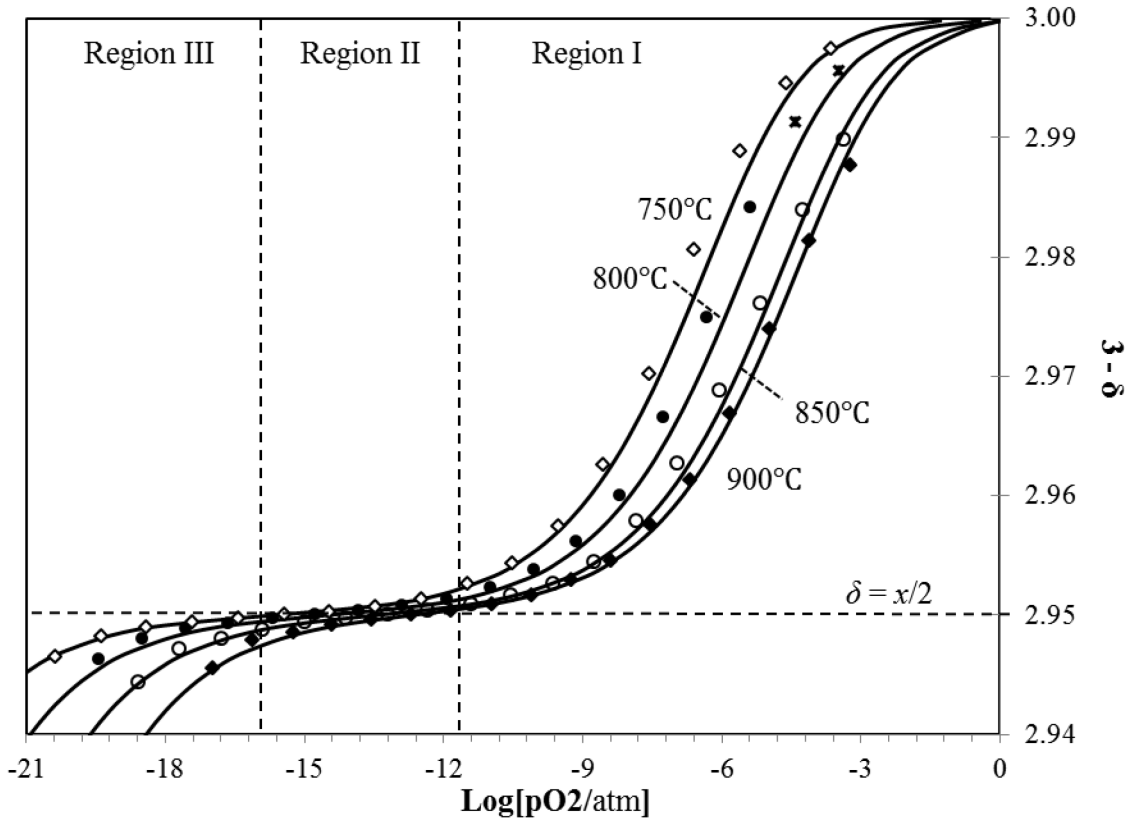

Figure 2.6: Measured nonstoichiometry of $La_{0.9}Ca_{0.1}FeO_{3-\delta}$ as a function of p_{O_2} at 750°,800°, 850°, and 900°C. Solid curves were calculated from the model discussed in the following section. The two high-p_{O_2} points at 800°C (*) were not fully equilibrated and not used in the fit.

The $\delta - p_{O2}$ relationship for LCF is qualitatively the same as that observed for $La_{1-x}Sr_xFeO_{3-\delta}$ (LSF), exhibiting three unique regimes: two with 3-δ decreasing with $log\ p_{O2}$ (Regions I and III), and the middle (Region II) forming a plateau [14]. Data from the return sweep (increasing p_{O_2}) are not shown; the discrepancy in the cumulative change in oxygen versus the forward sweep (decreasing p_{O_2}) varies from below 2% at 900°C to nearly 10% at 750°C. As previously discussed, powder diffraction revealed no additional phases, even in the sample found to show a 10%

oxygen hysteresis. Cycling the potential between the highest p_{O_2} (-150 mV) and the center of the plateau (-700 mV) at 850°C revealed no hysteresis. Additionally, all observed cases of hysteresis indicated a loss in oxygen mass upon increasing p_{O_2} relative to the initial sweep of decreasing p_{O_2}. Morphological changes in the packed LCF powder at the lowest p_{O_2} offer a possible explanation for this phenomenon: poor contact between LCF particles would greatly inhibit oxygen transport at low p_{O_2}, potentially isolating sections of LCF, thus drastically increasing the re-equilibration time for part of the sample on the return sweep. In this scenario, hysteresis on the return sweep is indicative of insufficient equilibration time between potentiostatic steps; as such, only the initial forward sweep was used for fitting.

2.4.3 Defect Model

The nonstoichiometry data were fit to a dilute-solution point-defect model developed by Mizusaki *et al.* for $La_{1-x}Sr_xFeO_{3-\delta}$ (LSF) [14]. The model consists of two equilibrium reactions, expressed in Kroger-Vink notation as:

$$\frac{1}{2}O_2(g) + V_O^{\bullet\bullet} + 2Fe_{Fe}^{x} \rightleftharpoons O_O^{x} + 2Fe_{Fe}^{\bullet} \quad 2.3$$

$$2Fe_{Fe}^{x} \rightleftharpoons Fe_{Fe}^{\prime} + Fe_{Fe}^{\bullet} \quad 2.4$$

Eqn. 2.3 expresses the reaction of oxygen gas with an oxygen vacancy ($V_O^{\bullet\bullet}$) to create a lattice oxygen (O_O^{x}) and oxidizing Fe^{3+} (Fe_{Fe}^{x}) to Fe^{4+} ($Fe_{Fe}^{\bullet}$). Eqn. 2.4 represents the disproportionation of neutral Fe^{3+} into positive $Fe_{Fe}^{\bullet}$ (Fe^{4+}, holes) and negative $Fe_{Fe}^{\prime}$ (Fe^{2+}, electrons) charge carriers, which can also be interpreted as an electron-hole equilibrium.

The model also includes B-site conservation and electroneutrality:

$$[Fe_{Fe}^{x}] + [Fe_{Fe}^{\prime}] + [Fe_{Fe}^{\bullet}] = 1, \quad 2.5$$

$$[Ca_{La}^{\prime}] + [Fe_{Fe}^{\prime}] = 2[V_O^{\bullet\bullet}] + [Fe_{Fe}^{\bullet}], \quad 2.6$$

where brackets indicate moles of species per mole unit cell.

All measured values of δ are relative; in order to establish an absolute nonstoichiometry, it is necessary to measure or define the nonstoichiometry at one point. Mizusaki *et al.* has shown for LSF that at the point where $\partial\delta/\partial Log\ p_{O2}$ is a minimum (occurring at the inflection point in Region II of Figure 2.6), the total electronic carrier concentration reaches a minimum, simplifying Eqn. 2.6 to $\delta \approx x/2$, where $\delta = [V_O^{\cdot\cdot}]$ and $x = [\mathrm{Ca}'_{\mathrm{La}}]$ [14], [71]. At this point (determined by numerically interpolating the $\delta - Log\ p_{O2}$ data), we assigned the value of the absolute nonstoichiometry to be $\delta_0 = x/2 = 0.05$.

Introducing mass-action equilibrium constants for Eqns. 2.3 and 2.4, designated as K_{ox} and K_i, respectively, and combining Eqns. 2.3-2.6 yield the following.

$$K_{\mathrm{ox}} = \frac{[O_O^x][\mathrm{Fe}_{\mathrm{Fe}}^{\bullet}]^2}{{P_{\mathrm{O2}}}^{1/2}[V_O^{\bullet\bullet}][\mathrm{Fe}_{\mathrm{Fe}}^x]^2} = \frac{(3-\delta)[\mathrm{Fe}_{\mathrm{Fe}}^{\bullet}]^2}{{P_{\mathrm{O2}}}^{1/2}\delta[\mathrm{Fe}_{\mathrm{Fe}}^x]^2} \qquad 2.7$$

$$K_i = \frac{[\mathrm{Fe}_{\mathrm{Fe}}^{\bullet}][\mathrm{Fe}_{\mathrm{Fe}}']}{[\mathrm{Fe}_{\mathrm{Fe}}^x]^2} \qquad 2.8$$

$$\frac{(2\delta - x + 1)\delta^{1/2}{P_{\mathrm{O2}}}^{1/4}}{(2\delta - x)(3-\delta)^{1/2}} = \frac{K_i}{K_{\mathrm{ox}}}\left[\frac{(3-\delta)^{1/2}(1+x-2\delta)}{(2\delta - x)\delta^{1/2}{P_{\mathrm{O2}}}^{1/4}}\right] - {K_{\mathrm{ox}}}^{-1/2} \qquad 2.9$$

Equation 2.9, expressed in slope-intercept form, allows K_{ox} and K_i to be fit to a $\delta - P_{\mathrm{O2}}$ dataset at a single temperature. The solid curves in Figure 2.6 represent the results of these fits.

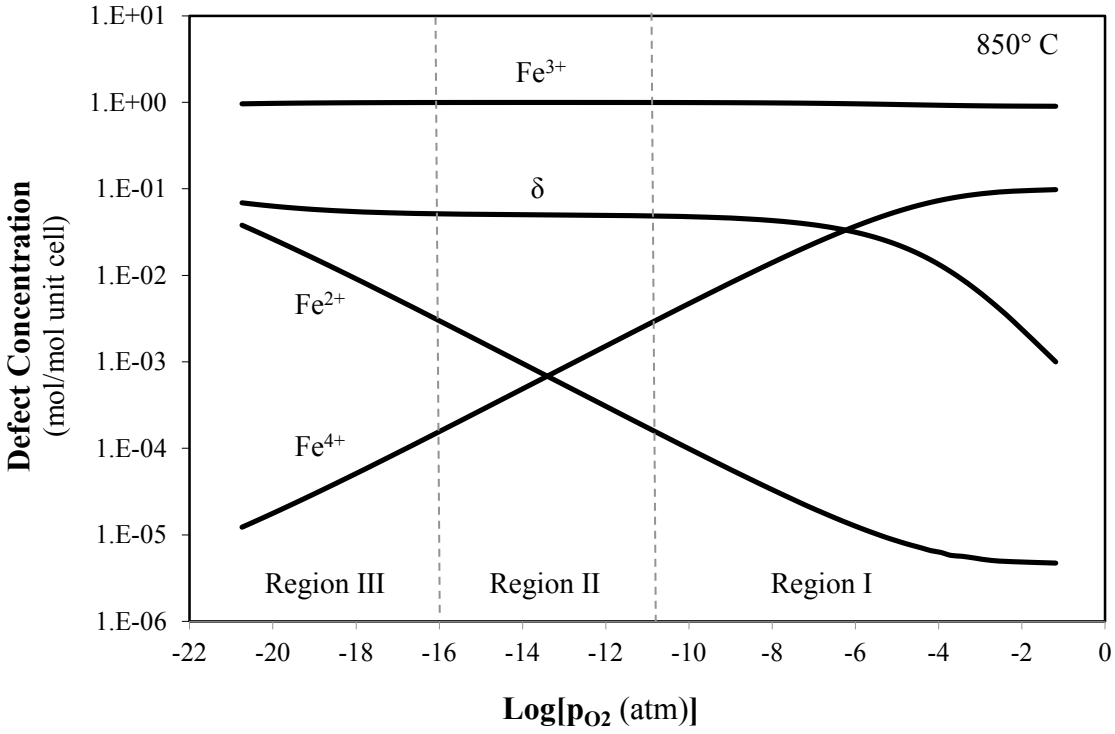

Figure 2.7: Calculated defect concentrations as a function of p_{O_2}, given at 850°C.

Using the equilibrium constants fit to the 850°C data, Figure 2.7 shows the model's defect composition as a function of p_{O_2}. The model predicts positive charge carriers to dominate electronic conduction in Region I, negative charge carriers to dominate in Region III, and total carrier concentration to be a minimum at $\delta = 0.05$ in Region II.

Combining Eqns. 2.3 and 2.4 yields a third equilibrium relationship (with equilibrium constant K_r), representative of the oxygen incorporation reaction at low p_{O_2}.

$$\frac{1}{2}O_2(g) + V_O^{\bullet\bullet} + 2Fe'_{Fe} \rightleftharpoons O_O^x + 2Fe_{Fe}^x \qquad 2.10$$

$$K_r = \frac{(3-\delta)[Fe_{Fe}^x]^2}{P_{O2}{}^{1/2}\delta[Fe'_{Fe}]^2} = \frac{K_{ox}}{K_i{}^2} \qquad 2.11$$

Although K_r provides redundant information to K_{ox} and K_i, it is as a useful *comparative metric* of reducibility under low-p_{O_2} conditions. K_{ox} represents the ease of incorporating oxygen at high p_{O_2} (where electron holes are the dominant electronic species); K_r represents the ease of incorporating oxygen at low p_{O_2} (where electrons are the dominant electronic species).

Figure 2.8 shows the temperature dependence of the two oxygen incorporation equilibrium constants, K_{ox} and K_r, and compares them to values reported for $La_{0.9}Sr_{0.1}FeO_{3-\delta}$ (LSF-91) measured by Mizusaki *et al*. [14]. Equations 2.7 and 2.11 show that increasing K_{ox} or K_r shifts the equilibria to a smaller δ for a given p_{O_2}. Thus, the data in Figure 2.8 imply that LCF is slightly less reducible than LSF at high p_{O_2} and more reducible than LSF at low p_{O_2}, despite having the same 10% aliovalent A-site doping.

The linear dependences shown in Figure 2.8 imply an Arrhenius relationship for $K_{ox}(T)$ and $K_r(T)$. Assuming the standard enthalpies of reaction for Eqs. 2.3, 2.4, and 2.10, 4 are independent of temperature, the data in Figure 2.8 can be fit using linear regression to obtain ΔH and ΔS for each reaction:

$$-RT\ln K_{ox} = \Delta H_{ox}^0 - T\Delta S_{ox}^0 \qquad 2.12$$

$$-RT\ln K_r = \Delta H_r^0 - T\Delta S_r^0 \qquad 2.13$$

$$-RT\ln K_i = \Delta H_i^0 - T\Delta S_i^0 \qquad 2.14$$

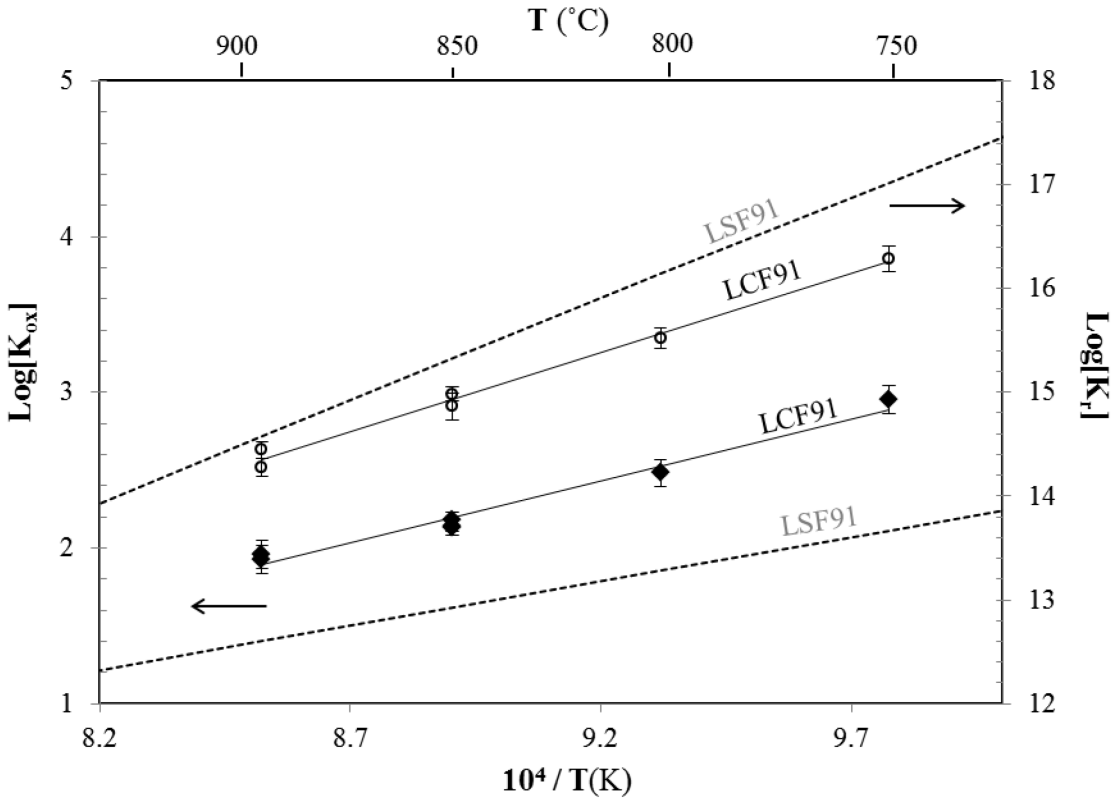

Figure 2.8: Arrhenius plot of the equilibrium constants, K_{ox} and K_r, for $La_{0.9}Ca_{0.1}FeO_{3-\delta}$. Lines represent least-squares fits. Error bars indicate the mean variance of each model fit shown in Figure 2.6. Dotted lines indicate the model fit for $La_{0.9}Sr_{0.1}FeO_{3-\delta}$ [14].

	ΔH^0_{ox} (kJ/mol)	ΔH^0_r (kJ/mol)	ΔH^0_i (kJ/mol)
$La_{0.9}Ca_{0.1}FeO_{3-\delta}$ (this work)	-152±6	-284±8	66±5
$La_{0.9}Sr_{0.1}FeO_{3-\delta}$ (Ref. [14])	-109	-456	174
$(La_{0.8}Ca_{0.2})_{0.95}FeO_{3-\delta}$ (Ref. [20])	-38	-	-

Table 2.1: Comparison of the standard reaction enthalpies to those found in the literature. The reported error corresponds to a 99% confidence interval for the linear regression analysis and includes one standard deviation of the error in fitting the equilibrium constants shown in Figure 2.6. The fitted values for ΔS^0_{ox}, ΔS^0_r, and ΔS^0_i for LCF-91 are -94, 34, and -55 J/molK, respectively.

The results of this regression are shown in Table 2.1, along with values for LSF-91 and 20%-doped LCF, $(La_{0.8}Ca_{0.2})_{0.95}FeO_{3-\delta}$. This comparison shows that under oxidizing conditions (high p_{O_2}), the enthalpy of oxygen incorporation for LCF-91 (ΔH^0_{ox} = -152 kJ/mol) is higher than that for LSF-91 (-109 kJ/mol) [14]. At low p_{O_2} (reducing conditions), LCF-91 has a smaller enthalpy of oxygen incorporation (-284 kJ/mol) than does LSF-91 (-456 kJ/mol) [14]. Also, in comparison to $(La_{0.8}Ca_{0.2})_{0.95}FeO_{3-\delta}$, 10% doped LCF-91 shows a larger ΔH^0_{ox}. These comparisons imply that Ca doping plays a greater role than just aliovalency [20]. Indeed, Figure 2.8 shows a narrowing gap between K_r and K_{ox} for LCF-91 compared to LSF-91, which implies a narrowing of the electronic band gap for Ca vs. Sr [14].

2.5 SUMMARY

The equilibrium oxygen nonstoichiometry for the perovskite $La_{0.9}Ca_{0.1}FeO_{3-\delta}$ (LCF-91) was determined for oxygen partial pressures between 10^{-3} and 10^{-21} atm and temperatures of 750-900°C. The appearance of three unique regimes in the oxygen partial pressure-nonstoichiometry data suggests that LCF behaves similarly to LSF, obeying a defect model consistent with localized electronic charge carriers. XRD data confirm LCF samples remained a single perovskite phase across all temperatures and p_{O_2} studied. In comparison to LSF-91, LCF-91 is slightly less reducible at high p_{O_2}, but slightly more reducible at low p_{O_2}, suggesting LCF has a smaller electronic band gap at the same doping concentration. In light of its thermodynamic stability and significant n-type carrier concentration under the reducing conditions, we consider LCF to be an interesting candidate for future kinetic studies.

2.6 APPENDIX A: ADAPTATION FOR FUTURE ELECTRODE MODELS

When modeling the electrochemical behavior of $La_{0.9}Ca_{0.1}FeO_{3-\delta}$ electrodes in later chapters, it will be useful to express the oxygen exchange reaction of Eqn. 2.3 in terms of the dominant electronic charge carrier, expressed as either holes or electrons, respectively.

$$\frac{1}{2}O_2(g) + V_O^{\bullet\bullet} \rightleftharpoons O_O^x + 2h^{\bullet} \qquad 2.15$$

$$\frac{1}{2}O_2(g) + V_O^{\bullet\bullet} + 2e' \rightleftharpoons O_O^x \qquad 2.16$$

The thermodynamic driving force, $\Lambda \equiv \sum_i \nu_i \mu_i$, where ν_i and μ_i are the stoichiometric coefficient and electrochemical potential for species *i*, respectively, for Eq. 2.15 is given below.

$$-\Lambda_p = \frac{1}{2}\mu_{O_2} + \mu_{V_O^{\bullet\bullet}} - 2\mu_{O_O^x} - 2\mu_{h^{\bullet}} \qquad 2.17$$

Assuming dilute species, electroneutrality, a dominant hole concentration relative to electrons, and a formulation of electrochemical potentials similar to that of Newman [72], Eq. 1.2 becomes

$$-\Lambda_p = -\Delta G^0_{rxn,p} + \frac{1}{2}RT\ln\left[f_{O2}^{solid}\right] + RT\ln\left[\frac{x_v}{(x-6x_v)^2}\right], \qquad 2.18$$

where the fugacity f_{O2}^{solid} corresponds to the p_{O_2} that would be in equilibrium with a solid at local vacancy concentration of x_v. Note that Eq. 2.18 is simply a restatement of Eq. 2.7 in the limit of $[Fe_{Fe}^{\bullet}] \gg [Fe_{Fe}']$, where $x_v = \frac{[V_O^{\cdot\cdot}]}{3} = \frac{\delta}{3}$, and $-\Delta G^0_{rxn,p} = RTlnK_{ox}$. Similarly, in the low-$p_{O_2}$ limit of $[Fe_{Fe}^{\bullet}] \gg [Fe_{Fe}']$, Eq. 2.11 can be restated below, where $-\Delta G^0_{rxn,n} = RTlnK_r$.

$$-\Lambda_n = -\Delta G^0_{rxn,n} + \frac{1}{2}RT\ln\left[f_{O2}^{solid}\right] + RT\ln\left[\frac{x_v}{(x-6x_v)^2}\right] \qquad 2.19$$

2.6.1 Thermodynamic Factor

In order to relate the electrochemical potential of vacancies driving kinetic and transport phenomena in future chapters to measurable values of vacancy concentration, a *thermodynamic factor* is defined below [39],

$$A(x_v) = -\frac{1}{2}\frac{\partial \ln\left[f_{O2}^{\text{solid}}\right]}{\partial \ln[x_v]}, \tag{2.20}$$

Setting $\Lambda_p = \Lambda_n = 0$, Eqs. 2.18 and 2.19 can be solved for $A(x_v)$.

$$A(x_v) = 1 - \frac{12x_v}{6x_v - x} \text{ (p-type simplification)} \tag{2.21}$$

$$A(x_v) = 1 + \frac{12x_v}{6x_v - x} \text{ (n-type simplification)} \tag{2.22}$$

In the case where the oxide is in equilibrium with its surrounding gas environment (*i.e.* $f_{O2}^{\text{solid}} = p_{O_2}$), the equilibrium terms $x_v = x_v^0$ and $A(x_v) = A_0(x_v^0)$ are defined, where,

$$A_0(x_v^0) = 1 - \frac{12x_v^0}{6x_v^0 - x} \text{ (p-type simplification)}, \tag{2.23}$$

$$A_0(x_v^0) = 1 + \frac{12x_v^0}{6x_v^0 - x} \text{ (n-type simplification)}. \tag{2.24}$$

Using the values for LCF given in Table 2.1, Eqs. 2.23 and 2.24 can be numerically solved as a function of p_{O_2}. These values of $A_0(p_{O2}, T)$ represent the bulk thermodynamic state of the LCF, and will be referred to throughout the dissertation. Figure 2.9 shows that at high p_{O_2} (>10^{-3} atm), A_0 approaches unity for all temperatures considered, while at extremely reducing conditions, A_0 increases as the p_{O_2}approaches the p-n transition.

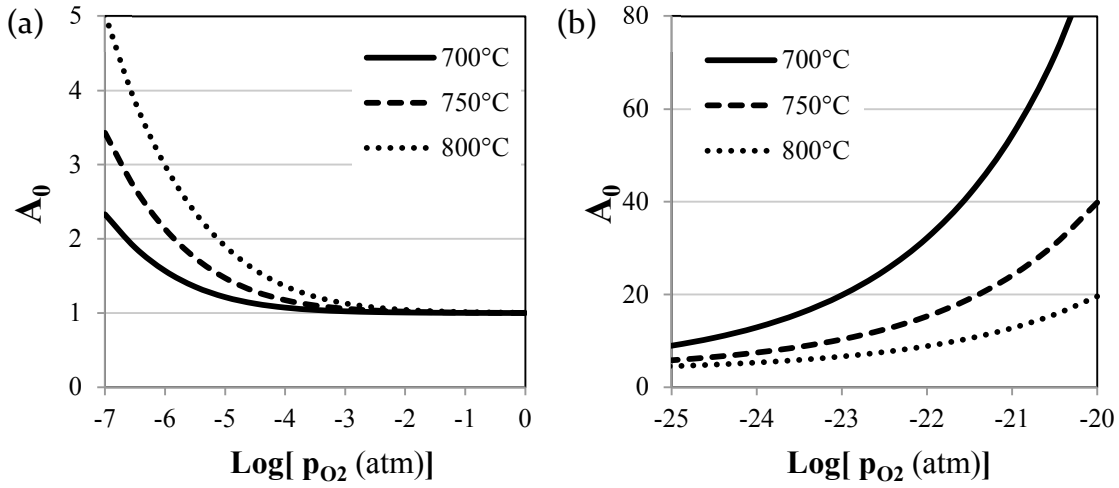

Figure 2.9: Equilibrium thermodynamic factor, $A(x_v^0)$ as function of p_{O_2} in the limit of (a) high $p_{O_2}$and p-type conductivity, and (b) low p_{O_2} and n-type conductivity.

2.7 APPENDIX B: STEADY STATE LEAK CURRENT

Two sources for a non-zero steady state leak current can exist under potentiostatic conditions for the two-probe coulometric titration cell previously described: a purely electronic current through the electroded portion of the electrolyte adjacent to the sample, suppressing ambipolar permeation of oxygen ions, and diffusion of molecular oxygen through microcracks in the zirconia electrolyte or poor seals.

At elevated temperatures and large p_{O_2} gradients, doped zirconia is known to behave as a mixed ionic and electronic conductor, giving rise to ambipolar permeation of the neutral species $\{V_{\ddot{O}} - 2e'\}$ at open circuit [66], [73]. The application of a potential suppresses the vacancy permeation at steady state, leaving a purely electronic flux. The steady state leak current, I_{ss}, for this situation, is expressed below [66],

$$I_{ss} = -\frac{A_r RT}{4FL}\int_I^{II} \sigma_{el}(p_{O2})\, d\ln p_{O2}\ , \qquad 2.25$$

where A_r is the area of the electroded portion of the electrolyte, L is the electrolyte wall thickness, $\sigma_{el}(p_{O2})$ is the total electrical conductivity (i.e. holes and electrons) as a function of p_{O2}, and the integral bounds I & II refer to the air and sample cell environments, respectively. Using Eq. 1.2 and the transport properties measured by Park *et al.* for 8 mol% YSZ [65], Figure 2.10 compares the predicted leak current for suppressed permeation to the measured values.

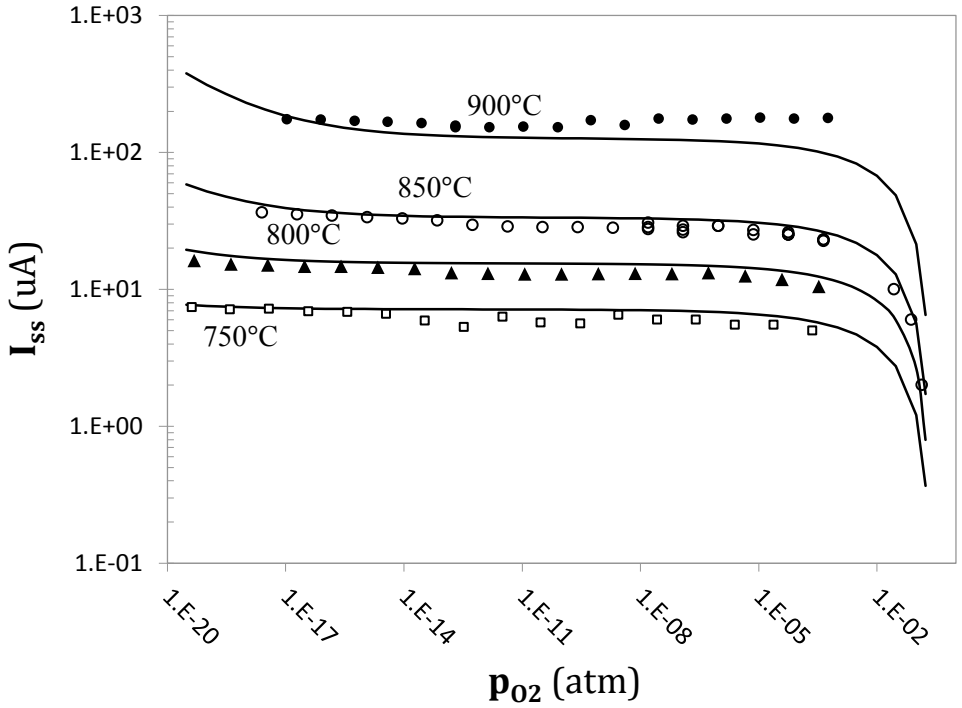

Figure 2.10: Steady-state leak current for each voltage step. Solid lines are given by Eq. 1.2.

The studied p_{O2} range (10^{-3} to 10^{-21} atm) falls mostly within the p-n transition of YSZ, resulting in approximately constant values of the leak current, shown in Figure 2.10—validating the assumption of a constant leak rate used in Eqn. 2.2 between small potentiostatic steps. Although the ionic transference number remains close to unity, the combination of long equilibration times and low vacancy solubility for LCF-91 makes this current non-negligible.

The second source of leak current, diffusion through microcracks in the YSZ, is avoidable through use of gas-tight zirconia tubes. Helium leak detection sensitive to 10^{-12} atm performed on the entire titration apparatus before and after coulometry confirmed the cell's gas tightness. Figure 2.11 shows the average geometrically scaled leak currents of several cells; cells that were found to have microcracks showed a marked increase in leak current.

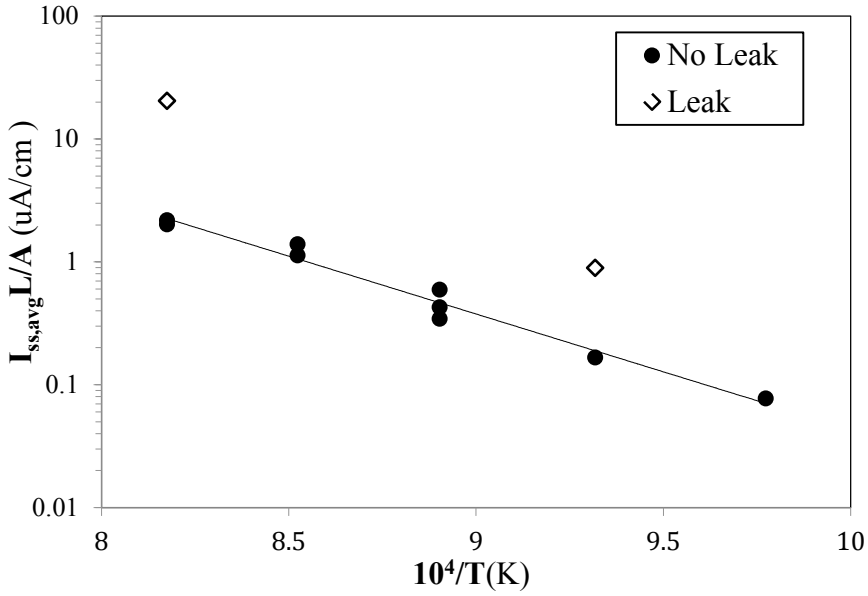

Figure 2.11: Scaled average leak current as a function of inverse temperature. Open symbols indicate cells found to have microcracks via helium leak detection.

In the case of microcracks or poor seals, the oxygen entering the cell must be constantly pumped out through the electrochemically active portion of the electrolyte to keep the cell at constant potential. This net flux of oxygen through the electroded portion of the electrolyte under steady-state polarization invalidates the use of Eqn. 2.1; therefore, data from cells found to have microcracks were discarded.

3. Porous Electrode Modeling Framework for p-Type Mixed-Conducting Electrodes

3.1 INTRODUCTION

The focus of this chapter is to model the relevant phenomena for oxygen reduction on the class of p-type mixed ionic and electronic conductors represented by $La_{0.9}Ca_{0.1}FeO_{3-\delta}$ (LCF-91) and $La_{0.6}Sr_{0.4}Co_{0.2}Fe_{0.8}O_{3-\delta}$ (LSCF-6428). Therefore, we choose to model only processes occurring at the oxygen electrode and neglect effects from the electrolyte and fuel electrode.

For porous mixed-conducting electrodes, the oxygen reduction process, illustrated in Figure 3.1, begins with molecular oxygen diffusing through a porous network before reacting at the electrode surface. The resulting ionic and electronic species may then diffuse through the electrode bulk or along its surface; the ease of these transport pathways will dictate the degree that the active region of the electrode can extend beyond the three-phase boundary. Lastly, oxygen ions are incorporated into the electronically-insulating electrolyte.

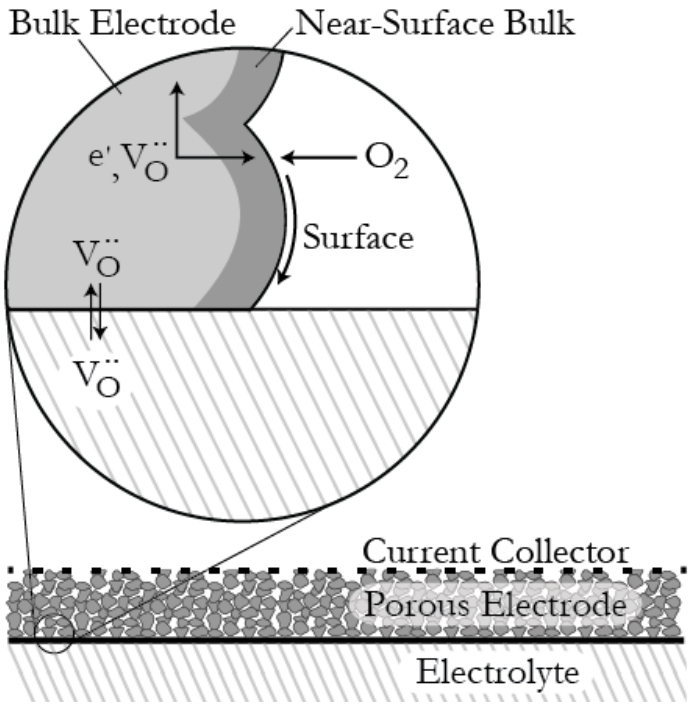

Figure 3.1: Depiction of the oxygen reduction process on a porous mixed-conducting electrode modeled in this chapter.

The extent of modeling can vary in the treatment of the porous electrode's microstructure as well as the degree of multidimensional transport considered. The simplest case is a one-dimensional "macrohomogeneous" model, which considers only transport normal to the electrode-electrolyte interface and uses volume-averaged values for electrode porosity, surface area, and tortuosity. This simplified model has been shown to be appropriate when transport is fast relative to the rate of oxygen exchange; the active region of the electrode extends well beyond the triple phase boundary, allowing transport to be well-approximated by 1D semi-infinite diffusion toward the electrolyte [35], [39].

A more rigorous extreme in porous modeling involves a three-dimensional analysis of an actual electrode microstructure [74]. Due to the time required for such an analysis, intermediate levels of modeling including 2D cylindrical models capturing radial diffusion effects and 3D spherical models capturing more

complicated geometric features, such as electrode particle overlap and contact angle, potentially offer an acceptable degree of modeling detail at a reduced computational cost.

The rate-determining physics relevant to oxygen reduction on $La_{1-x}Ca_xFeO_{3-\delta}$ electrodes (and semiconducting MIECs, in general) will first be treated independent of model geometry, before concluding with formulations specific to 1D macrohomogeneous (analytically-solved) and a 2D cylindrical (numerically-solved) models.

3.2 RATE-DETERMINING PHENOMENA

3.2.1 Thermodynamics

The thermodynamics for oxygen reduction, based on the theory and experiments presented in Chapter 2, serve as the basis for the porous electrode model, affecting both the kinetic and transport driving forces detailed in subsequent sections [75]. The overall reaction in oxidizing conditions is

$$O_2(g) + 2V_O^{\bullet\bullet} \rightleftharpoons 4h^{\bullet} + 2O_O^x, \tag{3.1}$$

where O_2 consumes two bulk oxygen vacancies ($V_O^{\bullet\bullet}$), yielding four holes localized on Fe^{4+} ($h^{\bullet}$, the principal electronic carrier at high p_{O_2}) and two occupied oxygen sites (O_O^x).

The semiconducting nature of LCF's band structure allows the electronic state of the material to be described in terms of electron and hole concentrations [76]. The basis species for the model's material balance is chosen to be oxygen vacancies, the concentration of which is given below per mole of total oxygen lattice sites.

$$x_v = \frac{[V_O^{\cdot\cdot}]}{3} = \frac{\delta}{3} = \frac{\text{mol oxygen vacancies per unit cell}}{\text{mol total oxygen sites per unit cell}}. \tag{3.2}$$

The general assumption of electroneutrality,

$$6x_v + x_h - x_e - x = 0, \tag{3.3}$$

can be further simplified by assuming that the mole fraction of electrons (x_e) is negligible compared to that of holes (x_h) under oxidizing conditions, allowing the

primary electronic species to be expressed in terms of A-site doping (x, 0.1 in the case of LCF-91) and vacancy mole fraction: $x_h \approx x - 6x_v$.

Because the impedance experiments detailed in future chapters were performed as perturbations from a state of equilibrium with the gas environment, it is convenient to define x_v^0 as the value of x_v in equilibrium with the surrounding p_{O_2} and T, and $\chi \equiv \frac{x_v - x_v^0}{x_v^0}$ as the dimensionless departure of x_v from this value.

As discussed in Chapter 2, the model captures the thermodynamic behavior of LCF using a thermodynamic factor, $A(x_v)$, simplified for the case of dominant hole conduction.

$$A(x_v) \equiv -\frac{1}{2}\frac{\partial \ln\left[f_{O2}^{\text{solid}}\right]}{\partial \ln[x_v]} = 1 - \frac{12x_v}{6x_v - x} = 1 + \frac{1+\chi}{\frac{1}{(A_0 - 1)} - \frac{\chi}{2}} \tag{3.4}$$

This parameter allows terms that scale with electrochemical potential (μ_v), such as vacancy diffusion and electrochemical reactions, to be expressed in terms of vacancy concentration. The value of the thermodynamic factor in the case of gas-solid equilibrium, $A_0(x_v^0)$, is defined below.

$$A_0(x_v^0) = 1 - \frac{12x_v^0}{6x_v^0 - x} \tag{3.5}$$

To allow for the possibility of the electrode surface possessing thermodynamics differing from measured bulk values (e.g. resulting from spatial variations in A-site composition), we propose a *near-surface bulk* layer of negligible volume, depicted in Figure 3.1, that is in equilibrium with the adjacent bulk and controls the thermodynamics of both the surface reaction and surface transport. We define a near-surface bulk vacancy mole fraction ($x_{v,s}$) and A-site doping (x_s) unique from the bulk, as well as a surface vacancy thermodynamic factor (A_s) in the same manner as the bulk,

$$A_s(x_{v,s}) \equiv -\frac{1}{2}\frac{\partial \ln f_{O_2}^{surf}}{\partial \ln x_{v,s}} = 1 - \frac{12x_{v,s}}{6x_{v,s}-x} = 1 + \frac{(1+\chi_s)}{(\frac{1}{(A_{0,s}-1)}-\frac{\chi_s}{2})}, \quad 3.6$$

$$A_{0,s}(x_{v,s}^0) = 1 - \frac{12x_{v,s}^0}{6x_{v,s}^0-x}, \quad 3.7$$

where $f_{O_2}^{surf}$ is the activity of oxygen in the near-surface bulk, $x_{v,s}^0$ is the value of $x_{v,s}$ in equilibrium with the surrounding p_{O_2}, $A_{0,s}$is its corresponding equilibrium thermodynamic factor, and $\chi_s = \frac{x_{v,s}-x_{v,s}^0}{x_{v,s}^0}$. Following from the equilibrium statement where the two phases meet ($\mu_{O_2} = \mu_{O_2,s}$) and Eqns. 3.4-3.7, χ_s can be expressed in terms of χ closest to the surface,

$$\chi_s = \frac{A_0}{A_{0,s}}\chi + \frac{(A_0^2 - A_{0,s}^2) + 2(A_{0,s}A_0^2 - A_0A_{0,s}^2)}{4A_{0,s}^3}\chi^2 + \frac{(A_0 - A_{0,s})(A_0^2(1+A_{0,s})^2 + A_0(A_{0,s} - 3A_{0,s}^3) - 2A_{0,s}^3)}{8A_{0,s}^5}\chi^3 + O[\chi^4]. \quad 3.8$$

3.2.2 Oxygen Exchange Kinetics

Two mechanisms, similar to those used to study oxygen exchange on metallic $La_{1-x}Sr_xCoO_{3-\delta}$ by Adler *et al.,* are considered for the overall reaction with the near-surface bulk. The first mechanism consists of the following elementary steps.

$$s + s \rightleftharpoons ss \quad \text{Combination} \quad 3.9$$

$$O_2(g) + ss \rightleftharpoons 2\{s\text{-}O^{2-}\} + 4h^{\bullet} \quad \text{Dissociative Adsorption} \quad 3.10$$

$$\{s\text{-}O^{2-}\} + V_{O,s}^{\cdot\cdot} \rightleftharpoons s + O_{O,s}^{x} \quad \text{Incorporation} \quad 3.11$$

In this mechanism, two single surface sites, *s*, combine to form a double surface site, *ss*. Next, O_2 (g) adsorbs onto this site before dissociating into two surface oxygen species, $s\text{-}O^{2-}$, generating four holes. Finally, $s\text{-}O^{2-}$ is incorporated into the bulk electrode, regenerating the surface vacancies.

A dilute solution approximation is used for all species, allowing the corresponding rate law to be formulated using mass action kinetics. At the high p_{O_2} of interest, $s\text{-}O^{2-}$ is assumed to be the dominant surface species, leading to a

solvent approximation for s-O^{2-}, and thus its exclusion from the rate law. The surface coverage of all other species is assumed small relative to the total site concentration.

In order to propose a testable rate law, one of the three elementary steps is assumed to be rate-determining, leaving the other two equilibrated. For this mechanism, dissociative adsorption (step 3.10) is assumed to be limiting, resulting in a rate law of the form

$$r_{\mathrm{O2,da}} = k_{\mathrm{da}} p_{O2} \Gamma_{ss} - \frac{k_{\mathrm{da}}}{K_{\mathrm{da}}} {x_h}^4, \tag{3.12}$$

where $r_{\mathrm{O2,da}}$ is given on a molar O_2 basis, k_{da} and K_{da} are the forward rate and equilibrium constants for Eq. 3.10, respectively, and Γ_i is the surface coverage of species i. This rate assumes an entirely entropic driving force, where holes are treated as species obeying mass action, according to the defect model in Chapter 2. Mass action equilibria for reactions 3.9 and 3.11 imply the following:

$$K_{\mathrm{comb}} = \frac{\Gamma_{ss}}{{\Gamma_s}^2}, \tag{3.13}$$

$$K_{\mathrm{inc}} = \frac{\Gamma_s}{x_{v,s}}. \tag{3.14}$$

Combining Eqs. 3.12-3.14, yields a dimensional rate law of the form below, with a forward rate dependence of $p_{O2} x_{v,s}^2$,

$$r_{\mathrm{O2,da}} = \frac{k_{\mathrm{da}}}{K_{\mathrm{da}}} \left(K_{\mathrm{rxn}}\, p_{O_2} {x_{v,s}}^2 - {x_h}^4 \right), \tag{3.15}$$

where $K_{\mathrm{rxn}} = K_{\mathrm{comb}} K_{\mathrm{da}} {K_{\mathrm{inc}}}^2$ is the overall equilibrium constant for Eq. 3.1. Using electroneutrality to eliminate x_h, and writing Eq. 3.15 in terms of the previously defined near-surface perturbation variable, χ_s , and surface thermodynamic parameter, $A_{o.s}$, yields

$$r_{\mathrm{O2,da}} = 2A_{0,s} \mathcal{R}^0_{\mathrm{O2,da}} \left[\frac{(1+\chi_s)^2 - (1 - \frac{(A_{0,s}-1)}{2}\chi_s)^4}{2A_{0,s}} \right], \tag{3.16}$$

$$\mathcal{R}^0_{\mathrm{O2,da}} = \left(\frac{k_{\mathrm{da}} K_{\mathrm{rxn}}}{K_{\mathrm{da}}}\right) p_{\mathrm{O2}} {x^0_{v,s}}^2 \ ,$$

where $\mathcal{R}^0_{\mathrm{O2,j}}$ is the forward exchange rate, $\mathcal{R}_{O2,\mathrm{j}}$ (defined by a rate of the form $r_{O_2,j} = \mathcal{R}_{O2,\mathrm{j}}\left[1 - e^{\frac{-\Lambda}{\lambda_j RT}}\right]$, where Λ is the free energy driving force for the overall reaction and λ_j is a stoichiometric factor relating the rate-limiting step j to the overall reaction), in the limit of equilibrium $(\Lambda \to 0)$ [76]. This scenario is henceforth referred to as *dissociative adsorption*.

Alternatively, the mechanism below is proposed,

$$O_2(g) + s \rightleftharpoons s\text{-}{O_2}^- + h^\bullet \qquad \text{Chemisorption} \qquad 3.17$$

$$s\text{-}{O_2}^- + s \rightleftharpoons 3\ h^\bullet + 2\ \{s\text{-}O^{2-}\} \qquad \text{Dissociation} \qquad 3.18$$

$$\{\ s\text{-}O^{2-}\} + V_O^{\cdot\cdot} \rightleftharpoons s + O_O^x \qquad \text{Incorporation} \qquad 3.19$$

where oxygen chemisorbs onto the surface as a diatomic superoxide species, $s\text{-}{O_2}^-$, before consuming an adjacent surface vacancy to dissociate into two surface oxygen species, and finally incorporates into the bulk. The same process described for dissociative adsorption is repeated for this case of *chemisorption* limitation, resulting in the rate law below, with a forward rate dependence of $p_{O2} x_{v,s}$.

$$r_{\mathrm{O2,ca}} = \frac{k_{\mathrm{ca}} K_{\mathrm{inc}}}{K_{\mathrm{rxn}}}\left(K_{\mathrm{rxn}} p_{\mathrm{O2}} x_{v,s} - \frac{{c_h}^4}{x_{v,s}}\right) = 2A_{0,s}\mathcal{R}^0_{\mathrm{O2,ca}}\left[\frac{(1+\chi_s) - \frac{\left(1 - \frac{(A_{0,s}-1)}{2}\chi_s\right)^4}{(1+\chi_s)}}{2A_{0,s}}\right] \qquad 3.20$$

$$\mathcal{R}^0_{\mathrm{O2,ca}} = (k_{\mathrm{ca}} K_{\mathrm{inc}}) p_{\mathrm{O2}} x^0_{v,s}$$

In general, both rate laws can be expressed in the form

$$r_{O_2,j} = 2A_{0,s}\mathcal{R}^0_{\mathrm{O2,j}}\ \mathrm{R}_{O_2,j}(\chi) = 2A_{0,s}\mathcal{R}^0_{\mathrm{O2,ca}}\ \chi_s + O[{\chi_s}^2], \qquad 3.21$$

where $R_{O_2,j}(\chi)$ is the bracketed dimensionless portion of Eqs. 3.16 and 3.20. Note that when linearized, both rate laws reduce to the same form, $r_{O2,j} = 2A_{0,s}\mathcal{R}^0_{\mathrm{O2,j}}\ \chi_s$.

3.2.3 Transport

The model considers two forms of transport: that of oxygen vacancies through the bulk electrode and that of a single species on the electrode surface. While the

former is well-understood, the nature of surface diffusion on MIEC perovskites is largely unknown. As such, two greatly simplified extremes are proposed based on the analysis for $La_{1-x}Sr_xCoO_{3-\delta}$ by Lu *et al.,* summarized in Figure 3.2 [34]. The first case assumes surface vacancies ($\Gamma_{v,s}$) to have a concentration and diffusivity different from the bulk, but remain in mass-action equilibrium with the near-surface bulk,

$$\frac{\theta_{v,s}}{x_{v,s}} = K_{\text{eqm}} \,, \tag{3.22}$$

where $\theta_{v,s}$ is the fractional surface coverage of $\Gamma_{v,s}$ and K_{eqm} is an equilibrium constant. The second case instead assumes the primary mobile surface species to be an adsorbed interstitial oxygen species (Γ_I), which has a surface coverage (θ_I) in equilibrium with the near-surface bulk vacancy concentration.

$$\theta_I x_{v,s} = K_{\text{eqm}} \tag{3.23}$$

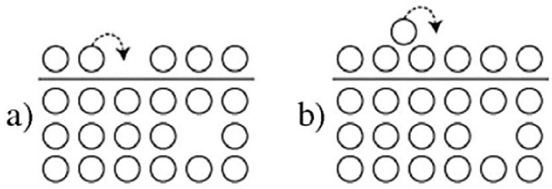

Figure 3.2: Two surface diffusion models are considered with differing mobile species: a) surface oxygen vacancies with $x_{v,s}$, and b) oxygen interstitials scaling inversely with $x_{v,s}$. Adapted from Ref. [34].

Both bulk vacancies and mobile surface species are assumed to be moderately dilute, implying all species diffuse independently, beyond sharing a common quasi-electric potential [30]. Under these assumptions, the molar flux (N_i) within the electrode for species *i* is

$$N_i = -\frac{D_i c_i}{RT} \nabla \mu_i \tag{3.24}$$

where D_i , c_i , and μ_i are the diffusivity, concentration, and electrochemical potential of species *i*, respectively.

The electrode is assumed to be predominantly an electronic conductor in oxidizing conditions, supported by combining the observed defect chemistry for LCF with estimates for hole and vacancy mobilities for LSF [29], [75]. Therefore, gradients in hole electrochemical potentials are neglected and local equilibrium implies $\nabla\mu_v \approx -\frac{1}{2}\nabla\mu_{O2,solid}$ for the bulk. Combining these assumptions yields expressions for the molar flux of bulk vacancies (N_v), surface vacancies ($N_{\Gamma_{v,s}}$), and surface interstitials (N_I),

$$N_v = -\frac{D_v c_O x_v}{RT}\nabla\mu_v \approx -\frac{D_v c_O x_v}{RT}\left(-\frac{1}{2}\frac{\partial \ln f_{\mathrm{O2}}^{\mathrm{solid}}}{\partial \ln x_v}\right)\nabla \ln x_v = -c_O D_v\, A(x_v)\,\nabla x_v \qquad 3.25$$

$$N_{\Gamma_{v,s}} = -\Gamma_0 K_{\mathrm{eqm}} D_{\Gamma_{v,s}} A_s(x_{v,s})\nabla x_{v,s} \qquad 3.26$$

$$N_I = \frac{\Gamma_0 K_{\mathrm{eqm}} D_I}{{x_{v,s}}^2} A_s(x_{v,s})\nabla x_{v,s} \qquad 3.27$$

where c_O is the concentration of bulk oxygen sites, Γ_0 is the concentration of surface oxygen sites, and $N_{\Gamma_{v,s}}$ and N_I have been expressed in terms of $x_{v,s}$ using Eqs. 3.22 & 3.23.

3.3 1D MACROHOMOGENOUS MODEL

The one-dimensional macrohomogeneous model, illustrated in Figure 3.3, only considers transport normal to the electrode-electrolyte interface, positioned at $y = 0$. In cases where gradients in vacancy concentration extend to lengths much greater than those of the electrode particles, the effects of transport in other dimensions can be neglected, supporting the use of a one-dimensional model. When the active region of the electrode is confined very close to the triple phase boundary, treatment of multi-dimensional transport may be required. In this model, the dimensionality of the electrode microstructure is captured by volume-averaged properties.

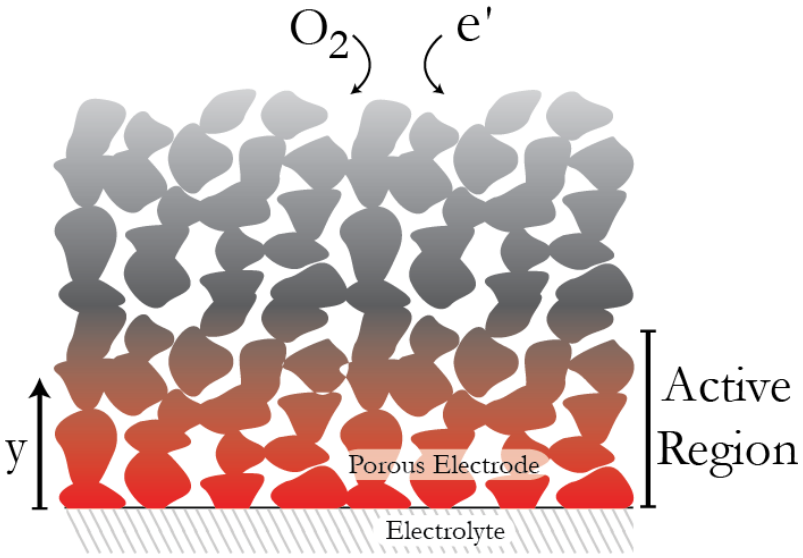

Figure 3.3: The 1D macrohomogeneous model is represented with color corresponding to gradients in vacancy concentration.

A molar vacancy balance over the superficial electrode volume serves as the model's governing equation, equating bulk vacancy accumulation to the sum of bulk transport, surface transport (oxygen interstitials, in this case), and surface kinetics terms,

$$c_O(1-\epsilon)\frac{\partial x_v}{\partial t} = -\frac{\partial N_v}{\partial y} + \frac{\partial N_I}{\partial y} - 2ar_{O_2,j} \tag{3.28}$$

where ϵ is the volume-average porosity and a is the volume-specific surface area. Substituting Eqs. 3.21, 3.25, and 3.27 into Eq. 3.28 yields

$$c_O(1-\epsilon)\frac{\partial x_v}{\partial t} = c_O D_v \frac{\partial}{\partial y}\left[A(x_v)\frac{\partial x_v}{\partial y}\right] + \Gamma_0 D_I K_{eqm}\frac{\partial}{\partial y}\left[\frac{A_s(x_{v,s})}{{x_{v,s}}^2}\frac{\partial x_{v,s}}{\partial y}\right] - 4aA_{0,s}\mathcal{R}^0_{O2,j}\mathrm{R}_{O_2,j} \tag{3.29}$$

where D_v and $\mathrm{D}_{O_2,s}$ are effective diffusivities that scale with $\frac{1-\epsilon}{\tau_v}$, τ_v is the volume-average electrode tortuosity, and index j represents the rate-determining step.

Finally, the electrode thickness is assumed to be semi-infinite, implying that at distances extremely far from the interface no net flux of vacancies in the bulk electrode exists.

$$\left.\frac{\partial x_v}{\partial y}\right|_{y\to\infty} = 0 \qquad 3.30$$

Electrochemically Measurable Terms

For the case of a galvanodynamic impedance experiment, the superficial current density, *I(t)*, is given by Faraday's law, and assumed to have a perturbation amplitude $\tilde{\imath}$ and frequency $\tilde{\omega}$.

$$\frac{I(t)}{2F} = \frac{\tilde{\imath}}{2F}\cos(\tilde{\omega}\, t) = c_o D_v \,\mathrm{A}(x_v)\left.\frac{\partial x_v}{\partial y}\right|_{y=0} + \frac{\Gamma_0 D_I K_{eqm} A_s(x_{v,s})}{{x_{v,s}}^2}\left.\frac{\partial x_{v,s}}{\partial y}\right|_{y=0} \qquad 3.31$$

The measured voltage difference between a reference electrode in equilibrium with the surrounding p_{O_2} and the electrode-electrolyte interface (at $y = 0$) of the working electrode is given by the Nernst equation,

$$V = \frac{RT}{4F}\ln\left[\frac{f_{O_2,solid}}{p_{O_2}}\right]_{y=0}. \qquad 3.32$$

3.3.2 Nondimensionalization and Scaling

Nondimensionalizing Eqs. 3.29-3.31 using the variables defined in Table 3.1, and writing entirely in terms of perturbation variables χ and χ_s and thermodynamic parameters A_o and $A_{o,s}$, yields the following system of equations for the case of surface interstitial diffusion.

$$\frac{\partial \chi}{\partial \tau} = \frac{\partial}{\partial \xi}\left[\left(1 + \frac{(1+\chi)}{\left(\frac{1}{(A_0-1)} - \frac{\chi}{2}\right)}\right)\frac{\partial \chi}{\partial \xi}\right] + \nu\frac{\partial}{\partial \xi}\left[\left(\frac{1+\frac{(1+\chi_S)}{\left(\frac{1}{(A_{0,S}-1)} - \frac{\chi_S}{2}\right)}}{(1+\chi_S)^2}\right)\frac{\partial \chi_S}{\partial \xi}\right] - A_{0,s}R_{O_2,j}(\chi_s) \qquad 3.33$$

$$\left(1 + \frac{(1+\chi)}{\left(\frac{1}{(A_0-1)} - \frac{\chi}{2}\right)}\right)\left.\frac{\partial \chi}{\partial \xi}\right|_{\xi=0} + \nu\left(\frac{1+\frac{(1+\chi_S)}{\left(\frac{1}{(A_{0,S}-1)} - \frac{\chi_S}{2}\right)}}{(1+\chi_S)^2}\right)\left.\frac{\partial \chi_S}{\partial \xi}\right|_{\xi=0} = \alpha\cos(\sigma\tau) \qquad 3.34$$

$$\left.\frac{\partial \chi}{\partial \xi}\right|_{\xi\to\infty} = 0 \qquad 3.35$$

$$U = \ln\left[\frac{(1-\frac{(A_0-1)}{2}\chi)^2}{(1+\chi)}\right]_{\xi=0} \qquad 3.36$$

The remaining dimensionless group in Eqs. 3.33 and 3.34, ν, defined below, represents the rate of surface diffusion of oxygen ad-atoms relative to that of bulk vacancy diffusion. In the case where $\nu = 0$, the model simplifies to one-dimensional bulk diffusion only.

$$\nu = \frac{\Gamma_0 D_I K_{\text{eqm}}}{c_o D_v x_v^0 x_{v,s}^0} \propto \frac{surface\ interstitial\ diffusion}{bulk\ vacancy\ diffusion} \tag{3.37}$$

For the case of surface vacancy diffusion described by Eq. 3.26, Eqs. 3.33, 3.34, & 3.37 become,

$$\frac{\partial \chi}{\partial \tau} = \frac{\partial}{\partial \xi}\left[\left(1 + \frac{(1+\chi)}{\left(\frac{1}{(A_0-1)} - \frac{\chi}{2}\right)}\right)\frac{\partial \chi}{\partial \xi}\right] + \nu \frac{\partial}{\partial \xi}\left[\left(1 + \frac{(1+\chi_s)}{\left(\frac{1}{(A_{0,s}-1)} - \frac{\chi_s}{2}\right)}\right)\frac{\partial \chi_s}{\partial \xi}\right] - A_{0,s} R_{O_2,j}(\chi_s) \tag{3.38}$$

$$\left(1 + \frac{(1+\chi)}{\left(\frac{1}{(A_0-1)} - \frac{\chi}{2}\right)}\right)\frac{\partial \chi}{\partial \xi}\Big|_{\xi=0} + \nu\left(1 + \frac{(1+\chi_s)}{\left(\frac{1}{(A_{0,s}-1)} - \frac{\chi_s}{2}\right)}\right)\frac{\partial \chi_s}{\partial \xi}\Big|_{\xi=0} = \alpha \cos(\sigma\tau) \tag{3.39}$$

$$\nu = \frac{\Gamma_0 D_{\Gamma_{v,s}} K_{eqm} x_{v,s}^0}{c_0 D_v x_v^0} \propto \frac{surface\ vacancy\ diffusion}{bulk\ vacancy\ diffusion} \tag{3.40}$$

Because we are only interested in the periodic steady state solution to χ relevant for a current-controlled impedance experiment, we assume the solution of $\chi(\xi, \tau)$ has the form below, expanded in a perturbation series around the dimensionless current amplitude α [39],

$$\begin{aligned}\chi(\xi, \tau; \alpha, \sigma) &= \alpha \frac{1}{2}\left[\chi_{11}(\xi)e^{j\sigma\tau} + \chi_{11}^* e^{-j\sigma\tau}\right] \\ &+ \alpha^2\left[\chi_{02}(\xi) + \frac{1}{2}\left(\chi_{22}(\xi)e^{2j\sigma\tau} + \chi_{22}^*(\xi)e^{-2j\sigma\tau}\right)\right] \\ &+ \alpha^3\left[\frac{1}{2}\left(\chi_{13}(\xi)e^{j\sigma\tau} + \chi_{13}^* e^{-j\sigma\tau}\right) + \frac{1}{2}\left(\chi_{33}(\xi)e^{3j\sigma\tau} + \chi_{33}^* e^{-3j\sigma\tau}\right)\right] + O(\alpha^4)\end{aligned} \tag{3.41}$$

where $\chi_{m,n}(\xi; \sigma)$ and its complex conjugate $\chi_{m,n}^*(\xi; \sigma)$are time and amplitude-independent complex vacancy concentration Fourier coefficients corresponding to the m^{th} harmonic of σ and current perturbation of order α^n, and $j^2 = -1$. Substitution of Eq. 3.41 into 3.33-3.35 allows the Fourier coefficients to be solved

sequentially in order of increasing harmonics. Finally, substituting Eq. 3.41 (evaluated at $\xi = 0$) into Eq. 3.36 and assuming the solution of U to have the form

$$\begin{aligned} U = {} & \alpha \frac{1}{2}\left[\eta_{11}(\sigma)e^{j\sigma\tau} + \eta_{11}^{*}(\sigma)e^{-j\sigma\tau}\right] \\ & + \alpha^2\left[\eta_{02}(\sigma) + \frac{1}{2}\left(\eta_{22}(\sigma)e^{2j\sigma\tau} + \eta_{22}^{*}(\sigma)e^{-2j\sigma\tau}\right)\right] + \\ & \alpha^3\left[\frac{1}{2}\left(\eta_{13}(\sigma)e^{j\sigma\tau} + \eta_{13}^{*}e^{-j\sigma\tau}\right) + \frac{1}{2}\left(\eta_{33}(\sigma)e^{3j\sigma\tau} + \eta_{33}^{*}e^{-3j\sigma\tau}\right)\right] + O(\alpha^4)\,, \end{aligned} \tag{3.42}$$

defines the Fourier voltage coefficient, $\eta_{m,n}(\sigma)$, and its complex conjugate, $\eta_{m,n}^{*}(\sigma)$, where indices m and n share the same meaning as in $\chi_{m,n}(\xi;\sigma)$.

In order to scale the modeling results for $\eta_{m,n}(\sigma)$ in a manner comparable to experiments, a characteristic magnitude U_c and characteristic frequency σ_c are implicitly defined for the linear voltage coefficient $\eta_{11}(\sigma)$ such that

$$U_{11}(\sigma) = \frac{\eta_{11}\left(\sigma \to \frac{\sigma}{\sigma_c}\right)}{U_c} = \frac{2\sqrt{2}}{\sqrt{1 + j\,\sigma\sqrt{3}}}\,, \tag{3.43}$$

where the right-hand side of Eq. 3.43 represents a Gerischer arc with a minimum imaginary component ("arc height") of -1 occurring at $\sigma = 1$ [77]. The second and third order voltage coefficients, $\eta_{22}(\sigma)$ and $\eta_{33}(\sigma)$, are scaled to the linear response using this definition of U_c and σ_c.

$$U_{22}(\sigma) = \frac{\eta_{22}\left(\sigma \to \frac{\sigma}{\sigma_c}\right)}{{U_c}^2} \tag{3.44}$$

$$U_{33}(\sigma) = \frac{\eta_{33}\left(\sigma \to \frac{\sigma}{\sigma_c}\right)}{{U_c}^3} \tag{3.45}$$

Quantity	Dimensional Form	Dimensionless Form	Dimensional Group
Position	y	$\xi = \frac{y}{y^*}$	$y^* = \sqrt{\frac{c_O x_v^0 D_v}{4a\mathcal{R}_{0,j}}}$
Time	t	$\tau = \frac{t}{t^*}$	$t^* = \frac{c_O x_v^0 (1-\epsilon)}{4a\mathcal{R}_{0,j}}$
Bulk Vacancy Mole Fraction	x_v	$\chi = \frac{x_v - x_v^0}{x_v^0}$	x_v^0
Near-Surface Bulk Vacancy Mole Frac.	$x_{v,s}$	$\chi_s = \frac{x_{v,s} - x_{v,s}^0}{x_{v,s}^0}$	$x_{v,s}^0$
Voltage	V	$U = \frac{V}{V^*}$	$V^* = \frac{RT}{2F}$
Current Amplitude	$\tilde{\imath}$	$\alpha = \frac{\tilde{\imath}}{i^*}$	$i^* = 2F\sqrt{4a\mathcal{R}_{0,j} c_o x_v^0 D_v}$
Frequency	$\tilde{\omega}$	$\sigma = \tilde{\omega}\, t^*$	$t^* = \frac{c_O x_v^0 (1-\epsilon)}{4a\mathcal{R}_{0,j}}$

Table 3.1: The 1D macrohomogeneous model is nondimensionalized using the above dimensional groups.

3.4 2D CYLINDRICAL MODEL

When the active region of the electrode is limited close to the three-phase boundary, gradients in the electrode can no longer be approximated by one-dimensional transport. To address this regime, the electrode microstructure is modeled as an array of cylinders, as shown in Figure 3.4, of radius R, length L, and inter-particle spacing b. Assuming each cylinder behaves identically, the model considers a single axisymmetric cylinder. Microstructural parameters can be related to cylindrical parameters, as shown in Table 3.2.

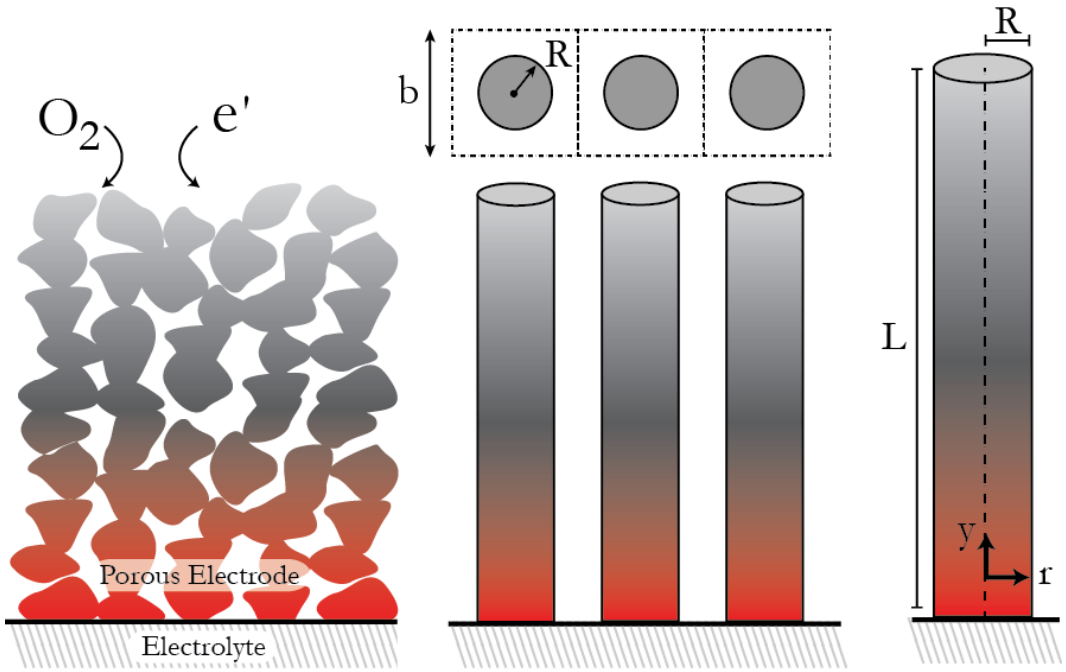

Figure 3.4: The 2D cylindrical model represents the porous electrode (left) as an array of cylinders (right), considering axial and radial transport.

Quantity	1D Macro-homogeneous	2D Cylindrical
Electrode Porosity $\left[\frac{electrode\ cm^3}{total\ cm^3}\right]$	$(1-\epsilon)$	$\frac{\pi R^2}{b^2}$
Specific Surface Area $\left[\frac{elec.surface\ cm^2}{total\ cm^3}\right]$	a	$\frac{2\pi R}{b^2}$
Bulk Oxygen Site Concentration	$c_0\left[\frac{mol\ oxygen\ sites}{total\ cm^3}\right]$	$c_0\left[\frac{mol\ oxygen\ sites}{electrode\ cm^3}\right]$
Surface Oxygen Site Concentration	$\Gamma_0\left[\frac{mol\ oxygen\ sites}{total\ cm^3}\right]$	$\Gamma_0\left[\frac{mol\ oxygen\ sites}{electrode\ cm^2}\right]$

Table 3.2: Microstructural parameters appearing in the 2D cylindrical model are defined in terms of those appearing in the 1D macrohomogeneous.

The molar oxygen vacancy balance for the cylindrical model only considers processes occurring in the bulk of the electrode; surface and interfacial processes are implemented as boundary conditions.

$$\frac{\partial x_v}{\partial t} = \frac{\partial}{\partial y}\left[D_v A(x_v)\frac{\partial x_v}{\partial y}\right] + \frac{1}{r}\frac{\partial}{\partial r}\left[rD_v A(x_v)\frac{\partial x_v}{\partial r}\right] \quad 3.46$$

Performing a shell balance on the electrode surface and assuming surface interstitial transport with a linear flux N_I' and unit vectors $\boldsymbol{e}_r$ and $\boldsymbol{e}_y$, the boundary condition becomes,

$$\Gamma_0 \frac{\partial \theta_I}{\partial t} = \frac{\partial}{\partial y}\left(\boldsymbol{e}_y \cdot \boldsymbol{N_I'}\right) - \boldsymbol{e}_r \cdot \boldsymbol{N}_v|_{r=R} + 2\, r_{O_2}. \quad 3.47$$

At the electrode-electrolyte interface, the superficial current density for a galvanodynamic impedance experiment will equal the sum of ionic current from the electrode bulk and surface.

$$\frac{\tilde{i}\,\cos(\tilde{\omega}\mathrm{t})}{2F} b^2 = -2\pi \int_0^R \boldsymbol{e}_y \cdot \boldsymbol{N_v}\,|_{y=0} r\partial r + 2\pi R \boldsymbol{e}_y \cdot \boldsymbol{N_I'}|_{y=0} \quad 3.48$$

Scaling and nondimensionalizing Eqs. 3.46-3.48 and the axisymmetric and semi-infinite diffusion boundary conditions using the definitions in Table 3.3 results in the following system.

$$A_0 \frac{\partial \chi}{\partial \tau} = \frac{\partial}{\partial \xi}\left[A(\chi)\frac{\partial \chi}{\partial \xi}\right] + \frac{1}{\rho}\frac{\partial}{\partial \rho}\left[\rho A(\chi)\frac{\partial \chi}{\partial \rho}\right] \quad 3.49$$

$$\varphi \frac{A_{0,s}}{(1+\chi_s)^2}\frac{\partial \chi_s}{\partial t} = -A(\chi)\frac{\partial \chi}{\partial \rho}|_{\rho=1} + \nu \frac{\partial}{\partial \xi}\left[\frac{A_s(\chi_s)}{(1+\chi_s)^2}\frac{\partial \chi_s}{\partial \xi}\right] - \kappa A_{0,s} R_{O_2}(\chi_s) \quad 3.50$$

$$\alpha \cos(\sigma\tau) = \int_0^1 A(\chi)\frac{\partial \chi}{\partial \xi}(\rho\, \partial \rho)|_{\xi=0} + \nu \left[\frac{\mathrm{A_s}(\chi_s)}{(1+\chi_s)^2}\frac{\partial \chi_s}{\partial \xi}\right]_{\xi=0,\rho=1} \quad 3.51$$

$$\frac{\partial \chi}{\partial \rho}|_{\rho=0} = 0 \quad 3.52$$

$$\frac{\partial \chi}{\partial \xi}|_{\xi\to\infty} = 0 \quad 3.53$$

Quantity	Dimensional Form	Dimensionless Form	Dimensional Group
Axial Position	y	$\xi = \frac{y}{y^*}$	$y^* = \mathrm{R}$
Radial Position	r	$\rho = \frac{r}{y^*}$	$y^* = \mathrm{R}$
Time	t	$\tau = \frac{t}{t^*}$	$t^* = \frac{R^2}{A_0 D_v}$
Bulk Vacancy Mole Fraction	x_v	$\chi = \frac{x_v - x_v^0}{x_v^0}$	x_v^0
Near-Surface Bulk Vacancy Mole Frac.	$x_{v,s}$	$\chi_s = \frac{x_{v,s} - x_{v,s}^0}{x_{v,s}^0}$	$x_{v,s}^0$
Voltage	V	$U = \frac{V}{V^*}$	$V^* = \frac{RT}{2F}$
Current Amplitude	$\tilde{\imath}$	$\alpha = \frac{\tilde{\imath}}{i^*}$	$i^* = 2Fc_0 x_v^0 D_v a$
Frequency	$\widetilde{\omega}$	$\sigma = \widetilde{\omega}\, t^*$	$t^* = \frac{R^2}{A_0 D_v}$

Table 3.3: The 2D cylindrical model is nondimensionalized using the above dimensional groups.

The three remaining dimensionless groups, φ, ν, and κ, relate to surface oxygen storage, surface interstitial diffusion, and surface reaction rate.

$$\varphi = \frac{A_0 \Gamma_0 K_{\mathrm{eqm}}}{A_{0,s} R c_o x_v^0 x_{v,s}^0} \propto \frac{surface\ oxygen\ capacity}{bulk\ vacancy\ capacity} \tag{3.54}$$

$$\nu = \frac{\Gamma_0 K_{\mathrm{eqm}} D_I}{R c_o D_v x_v^0 x_{v,s}^0} \propto \frac{surface\ interstitial\ diffusion}{bulk\ vacancy\ diffusion} \tag{3.55}$$

$$\kappa = \frac{4\mathcal{R}_O R}{c_o D_v x_v^0} \propto \frac{surface\ reaction}{bulk\ vacancy\ diffusion} \tag{3.56}$$

3.4.1 Finite-Element Solution and Skin Layer Formulation

In order to obtain a numerical solution to the above nonlinear partial differential equation and boundary conditions, the heat transfer package for the finite-element software Comsol Multiphysics v4.2 was used. Triangular mesh elements were selectively refined in the cylinder body near the edges at $\xi = 0$ and $\rho = 1$, and,

particularly, at the corner $(\xi, \rho) = (0,1)$. Rectangular mesh elements were used along the cylinder surface $\rho = 1$.

Due to the difficulty of finding a mesh-independent solution for $\nu > 0$ that satisfies Eq. 3.50—an inhomogeneous radial Neumann boundary condition containing second-order axial derivatives—a numerical representation of the surface is used to simplify the problem. As shown in Figure 3.5, a continuous "skin layer" function, $\phi(\tilde{\rho}, \tau)$, is applied near the cylinder surface, defined by the system,

$$\frac{\partial \phi}{\partial \tau} = \frac{\partial^2 \phi}{\partial \tilde{\rho}^2} \tag{3.57}$$

$$\phi|_{\tilde{\rho}=0} = 1, \quad \phi|_{\tilde{\rho}\to\infty} = 0, \quad \phi|_{\tau=0} = 0, \tag{3.58}$$

where $\tilde{\rho} = 1 - \rho$ and all gradients are assumed to dissipate before reaching the cylinder axis. Using a similarity transform, the solution becomes,

$$\phi(\tilde{\rho}, \tau) = \operatorname{erfc}\left[\frac{\tilde{\rho}}{\delta(\tau)}\right], \tag{3.59}$$

where $\delta(\tau) = \sqrt{4\tau}$. Solving Eq. 3.59 at $\tau = \tau_0$ defines a time-independent skin layer function $\bar{\phi} = \phi(\tilde{\rho}, \tau_0) = \operatorname{erfc}\left[\frac{\tilde{\rho}}{\delta(\tau_0)}\right]$ with a characteristic decay length, $\delta(\tau_0)$. Instead of appearing as a boundary condition, surface diffusion can now be implemented as a bulk process weighted by a sharply decaying "surface": $\int_0^\infty \bar{\phi}(\tilde{\rho}, \tau_0)\partial\tilde{\rho}$. Because both bulk and surface diffusion fluxes can be expressed in the form $f(\chi, \chi_s)\nabla\chi$, both processes can be combined into a single flux with an effective diffusivity, $D_0(1 + \gamma\phi)$, where D_0 represents the dimensionless *bulk* diffusivity, and γ is a concentration-dependent coefficient for surface diffusion. In order to ensure surface diffusion occurs only along a surface defined by normal vector $\boldsymbol{n}$, the total (surface & bulk) dimensionless flux, $\boldsymbol{N} = -\boldsymbol{D} \cdot \boldsymbol{\nabla}\chi$, takes the form

$$\boldsymbol{N} = -D_0(1 + \gamma\bar{\phi})\boldsymbol{\nabla}\chi + D_0\gamma\bar{\phi}(\boldsymbol{n} \cdot \boldsymbol{\nabla}\chi)\boldsymbol{n} \,. \tag{3.60}$$

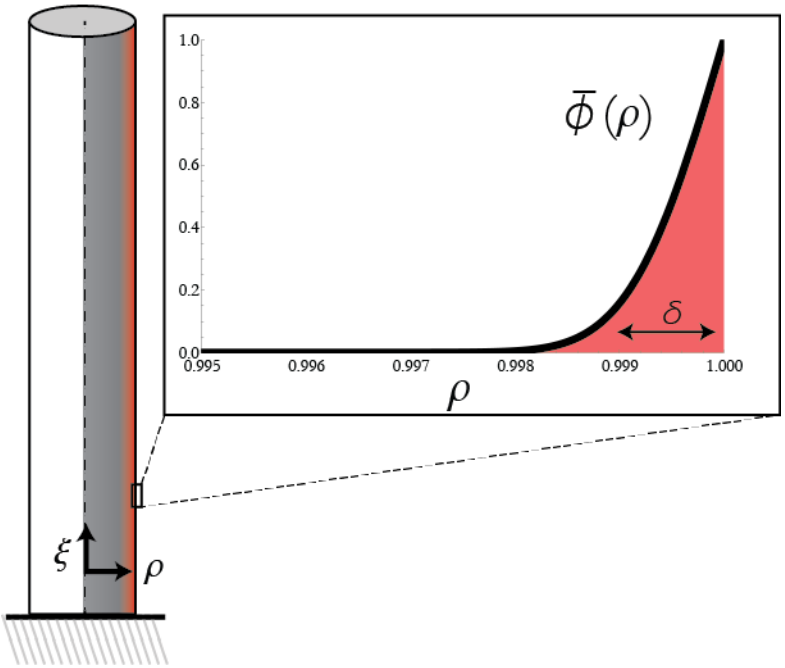

Figure 3.5: A zero-volume electrode "surface" is numerically represented by a radial decay function, $\bar{\phi}(\rho)$, staining the electrode surface with a dimensionless decay length $\delta = 0.001$.

A major advantage of this formulation is its application to any surface of arbitrary geometry, with normal vector $\boldsymbol{n} \equiv \frac{\boldsymbol{\nabla}\bar{\phi}}{|\nabla\bar{\phi}|}$. Substituting this normal vector into Eq. 3.60 and rewriting in Einstein notation defines the effective diffusivity tensor $\boldsymbol{D} = D_{ij}$,

$$D_{ij} = D_0(1 + \gamma\bar{\phi})\delta_{ij} - D_0\gamma\frac{\bar{\phi}}{(\nabla\bar{\phi})^2}\frac{\partial\bar{\phi}}{\partial x_i}\frac{\partial\bar{\phi}}{\partial x_j}, \qquad 3.61$$

where x_i represents orthogonal coordinates and δ_{ij} is the Kronecker delta. Simplifying Eq. 3.61 for the cylindrical ρ- ξ system of interest yields

$$D_{ij} = \begin{bmatrix} D_{\rho\rho} & D_{\xi\rho} \\ D_{\rho\xi} & D_{\xi\xi} \end{bmatrix} = \begin{bmatrix} D_0 & 0 \\ 0 & D_0(1 + \gamma\bar{\phi}) \end{bmatrix}. \qquad 3.62$$

In order to define γ, linking this numerical skin layer formulation to the analytical formulation, the dimensional linear surface flux N_I is equated to a

surface flux in the desired form $N_v^* = -A(x_v)c_0 D_v \gamma \phi \frac{\partial x_v}{\partial z}$, integrated over the skin layer.

$$\gamma = \frac{\nu}{\int_0^\infty \bar{\phi}(\tilde{\rho})\partial\tilde{\rho}} \frac{1}{(1+\chi)(1+\chi_s)} \tag{3.63}$$

3.5 1D MACROHOMOGENEOUS MODEL RESULTS

3.5.1 Dimensional Analysis of Linear 1D Solution

The linear Gerischer response for the one-dimensional model given by Eq. 3.43 and shown in Figure 3.6, is general to co-limited reaction-diffusion models [11], and its scaled form is independent of p_{O_2} and the relative degree of surface diffusion, ν. The Gerischer response, $Z_G(\Omega \cdot cm^2)$—the unscaled, dimensional form of U_{11}—predicted by the macrohomogeneous model has a dimensional arc height, R_c, and peak frequency, ω_c, defined below in terms of model parameters.

$$Z_G = \frac{V^* \eta_{11}(\sigma)}{i^*} = R_c \frac{2\sqrt{2}}{\sqrt{1+j\frac{\omega}{\omega_c}\sqrt{3}}} \tag{3.64}$$

$$R_c = \frac{\mathrm{RT}}{8F^2\sqrt{8a\mathcal{R}_{0,j}c_O x_v^0 D_v(1+\nu)}} \tag{3.65}$$

$$\omega_c = \frac{4a\mathcal{R}_{0,j}}{c_O x_v^0 (1-\epsilon)A_0\sqrt{3}} \tag{3.66}$$

Eq. 3.65 shows the magnitude of the linear response is dependent on both kinetic and transport effects, while Eq. 3.66 shows that the characteristic frequency is influenced predominantly by the exchange kinetics and thermodynamics. These expressions for R_c and ω_c are general to both rate laws and surface diffusion scenarios. Therefore, measuring their dependence on experimental conditions (particularly p_{O2}) can potentially provide information about the exchange rate or surface diffusion. For example, in the high-p_{O2} limit shown in Chapter 2 for LCF where $x_v^0 \propto p_{O2}^{-1/2}$ and $A_0 \propto p_{O2}^{\sim 0}$, equilibrium exchange rates for dissociative adsorption ($\mathcal{R}_{0,da} \propto p_{O2} x_v^{0\,2}$) and chemisorption ($\mathcal{R}_{0,ca} \propto p_{O2} x_v^0$) predict $\omega_c \propto p_{O2}^{1/2}$ and $\omega_c \propto p_{O2}$, respectively.

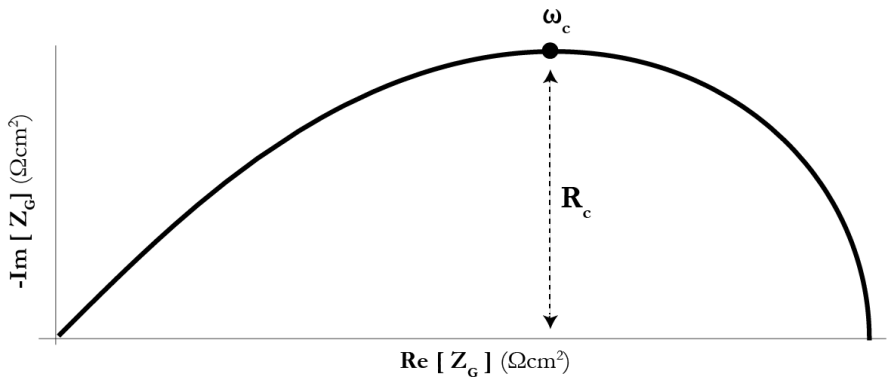

Figure 3.6: A Nyquist plot of the linear impedance, Z_G, results from the 1D macrohomogeneous model with dimensional arc height R_c and peak frequency ω_c.

3.5.2 Nonlinear Harmonics for 1D Model

In this section, key trends in the nonlinear response predicted by the 1D macrohomogeneous model will be highlighted. In order to simplify discussion, only the cases of surface interstitial diffusion with either a dissociative adsorption or chemisorption rate law will be analyzed.

For the simplified case of just bulk diffusion ($\nu = 0$) and fixed surface thermodynamics ($A_0 = A_{0,s}$), Figure 3.7 gives the predicted harmonic voltage responses (U_{22}, U_{33}) for a current perturbation of amplitude α and frequency σ. Phasor lines are drawn through dimensionless frequencies of $\frac{1}{2}$ and $\frac{1}{3}$ for U_{22} and U_{33}, respectively, to indicate the time constant of the linear response shown in Figure 3.6. The thermodynamic factors used in Figure 3.7 correspond to the values measured in Chapter 2 at 0.01, 0.21, and 1 atm O_2 and 800°C; the values $A_0 \approx 1$ indicate a very small change in vacancy concentration for even moderate changes in p_{O_2}. For these conditions, both models predict a weak p_{O_2} dependence. Though difficult to see, both bulk models show the low-frequency real intercept, representative of the magnitude of the harmonic response relative to the linear signal, moving in the negative real direction, and the phasor line rotating counter-clockwise for increasing A_0 (decreasing p_{O_2}) for both U_{22} and U_{33}. Additionally,

compared to the dissociative adsorption-limited model, chemisorption predicts a slightly smaller magnitude of harmonic response relative to the linear response.

According to the surface diffusion model assuming mobile interstitial oxygen species, the relative amount of surface diffusion, ν, is expected to increase with increasing p_{O_2}. Because both A_0 and ν are dependent on p_{O_2}, it is not physically consistent to vary them independently. However, because the p_{O_2} dependence of A_o is extremely weak for such a slightly doped material in an oxidizing environment, any strong p_{O_2} dependence in the data will arise from changes in ν (if assuming identical bulk and surface thermodynamics). In order to isolate the predicted effect of ν on the nonlinear response, a constant value of $A_0 = A_{0,s} = 1.01$ is assumed, and ν is independently varied. Figure 3.8 shows the modeling results for values of $\nu = 0$ (i.e. bulk-only diffusion), 0.5, 1, and 10 for either a dissociative adsorption or chemisorption rate law, with arrows highlighting the trends of phasor rotation and low-frequency intercept with increasing p_{O2}. Not only do both models exhibit a strong dependence on ν, but the nature of this dependence is sensitive to the assumed rate law.

Finally, allowing the surface thermodynamics to deviate from measured bulk values ($A_{0,s} > A_0$) also has a unique impact on the predicted nonlinear response. Figure 3.9 captures this relationship by plotting the low-frequency intercept of U_{22} and U_{33} versus ν parametric in $A_{0,s}$. For both rate laws, values of ν and $A_{0,s}$ exist that cause the harmonic features to shift from positive to negative real values; furthermore, U_{33} can pass through a point of nullification where its magnitude is approximately zero for all frequencies. The values of ν and $A_{0,s}$ at which these trends are observed provide another degree of sensitivity for distinguishing between rate laws.

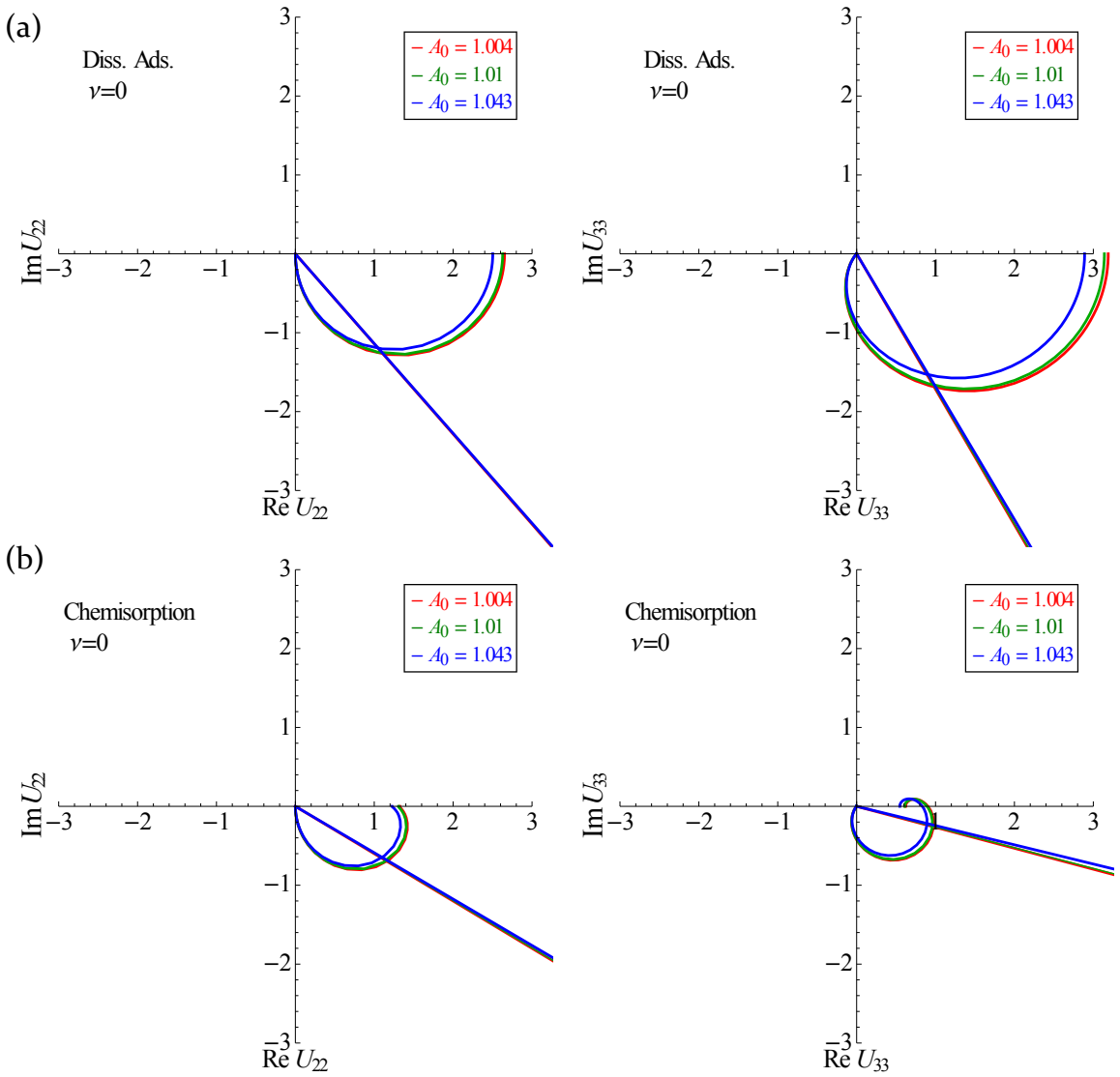

Figure 3.7: The case of no surface diffusion ($\nu = 0$) at thermodynamic values corresponding to p_{O_2} of 1 (red), 0.21 (green), and 0.01 atm (blue) at 800°C shows an identical linear response for (a) dissociative adsorption and (b) chemisorption-limiting rate law. Both scenarios show a very weak variation with thermodynamic state.

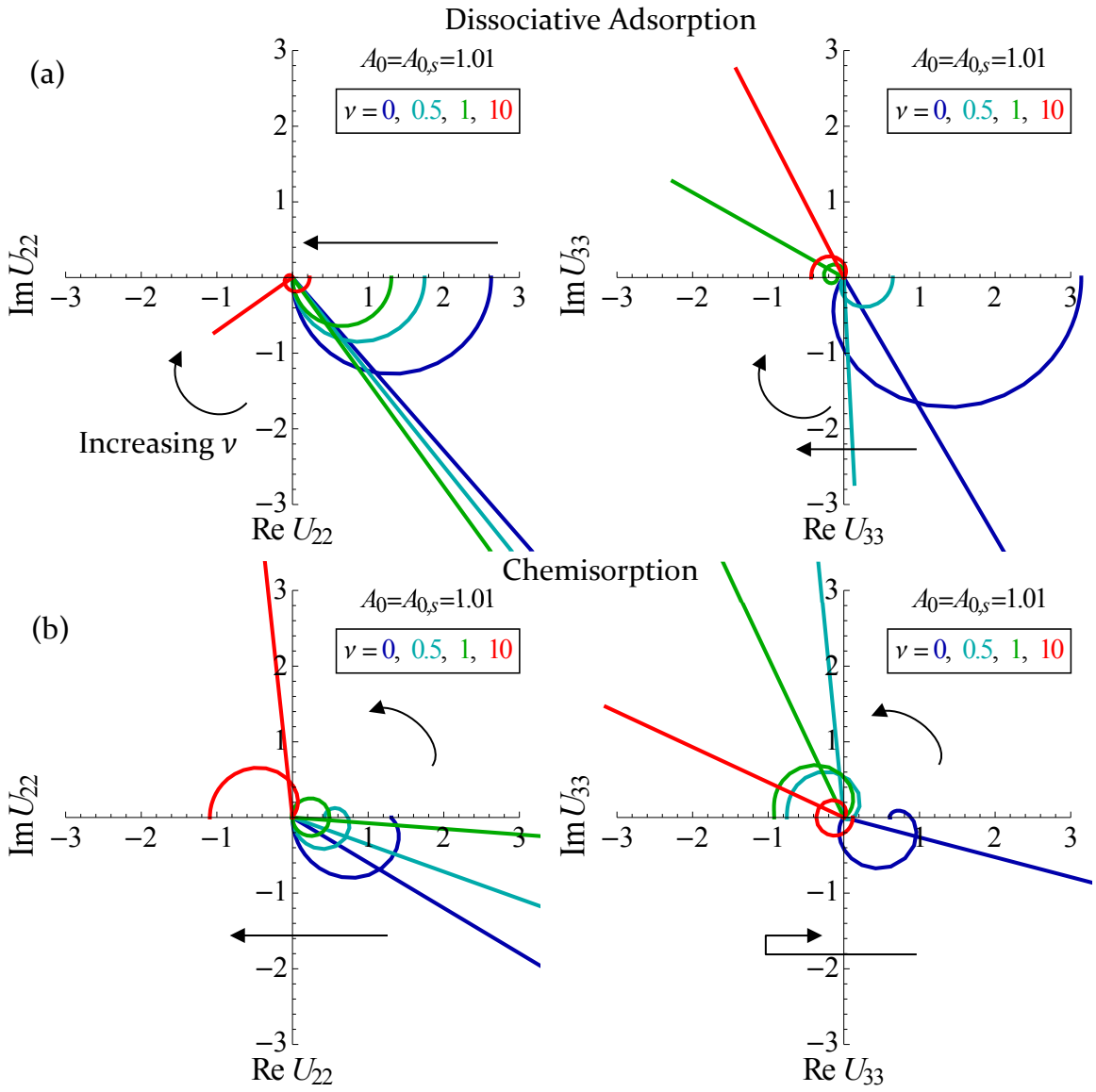

Figure 3.8: The nonlinear response predicted for a bulk and surface diffusion model assuming a constant value of $A_0 = A_{0,s} = 1.01$, shows a strong dependence on the parameter ν, the rate of surface diffusion relative to bulk diffusion, for both (a) dissociative adsorption and (b) chemisorption-limited models. Arrows indicate the direction of phasor rotation and shifting low-frequency intercept with increasing values of ν = 0, 0.5, 1, and 10.

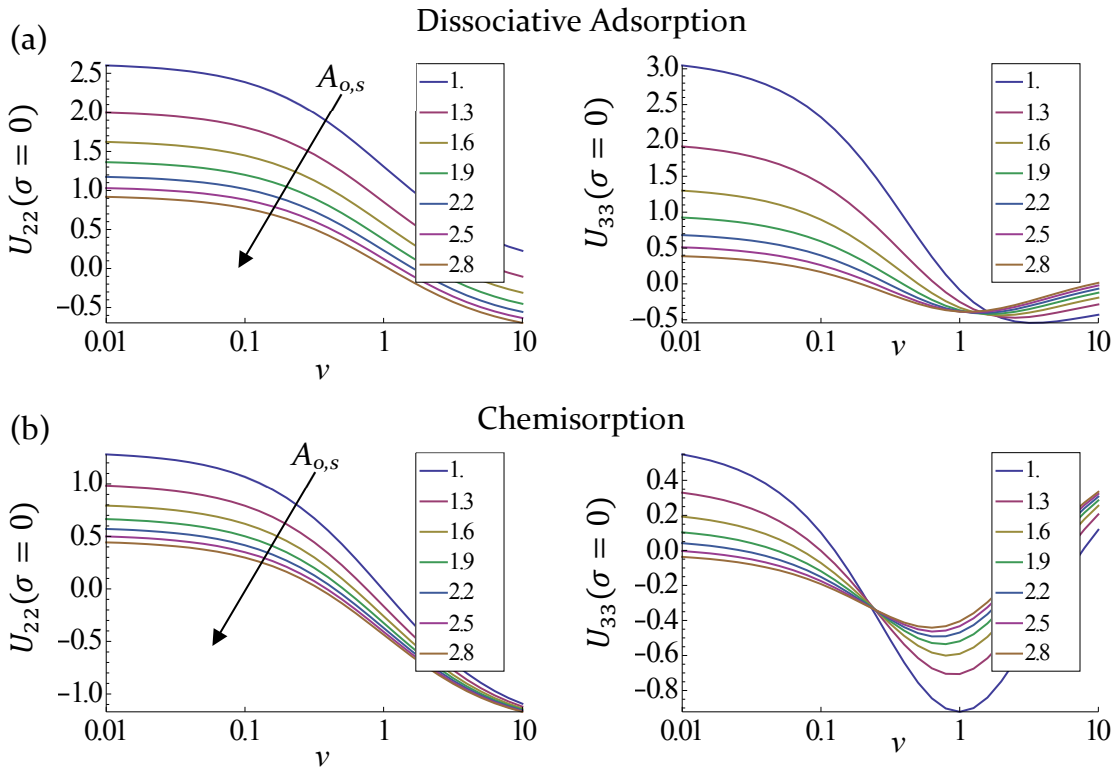

Figure 3.9: The low-frequency real intercept of U_{22} and U_{33} is shown for both (a) dissociative adsorption, and (b) chemisorption rate laws, assuming $A_0 = 1.01$ and parametric in $A_{0,s}$. U_{33} shows an inversion of its trend with $A_{0,s}$ at small values of ν.

3.6 2D CYLINDRICAL MODEL RESULTS

Unpublished work performed by Kon and Adler has shown that for values of both ν and $\kappa < 100$, a linearized numerical model with a skin layer decay length $\delta = 0.001$ yields results within 5% of the analytical solution given by Lu *et al.* [34]. Therefore, for this model, a value of 0.001 is chosen for δ, using quadrilateral surface mesh elements with thickness $\delta/10$. In the case of high values of ν and low κ where the active length of the electrode extends far from the electrolyte, a cylinder with $L/R = 30$ was used; for all other cases $L/R = 15$ was adequate. For all results presented below, surface interstitial transport, a dissociative adsorption rate law, $A_0 = A_{0,s} = 1.01$, and $\varphi = 0$ were assumed. The total degrees of freedom for the nonlinear model ranged from 50,000 to 200,000, resulting in solution times for a frequency sweep ranging from 30 min to 12 hours for single set of κ, ν, and $A_{0,s}$.

Figure 3.10 shows 2D axisymmetric distributions of the real portion of the dimensionless linear, second, and third-order vacancy Fourier coefficients, χ_{11}, χ_{22}, and χ_{33} for $\kappa = 1$ and $\nu = 2$. At a frequency $\sigma = 0.01$, the solution nears its steady-state distribution, with gradients dissipating at $\xi > 3$. For a fast polarization frequency of $\sigma = 100$, gradients are confined close to the electrolyte ($\xi = 0$) and surface ($\rho = 1$). The solutions for χ_{22}, and χ_{33} show that the nonlinear portions of the response require a higher degree of mesh refinement near the electrode surface than required by the linear response.

Figure 3.11 shows the linear impedance predicted by the cylindrical model for various values of κ and ν. These results show good agreement of the numerical model using the skin layer surface approximation with the linear analytical solution given by Lu *et al.* [34]. At small values of κ and ν, an impedance response approaching that of the 1D is predicted. Upon increasing, κ and ν, corresponding to conditions of increased radial gradients, a depressed Gerischer shape is observed.

Lastly, Figure 3.12 shows the nonlinear voltage coefficients, U_{22} and U_{33} as a function of increasing κ for $\nu = 0$, 0.2, 2, and 20. Good agreement with the nonlinear 1D analytical solution presented in this chapter is achieved at $\kappa \leq 0.2$ for all values of ν. Therefore, comparing the spectra at higher κ to $\kappa = 0.2$ shows the deviation between 1D and 2D models. Surprisingly, the deviation between 1D and 2D models at $\nu < 20$ is smaller than one would expect due solely to scaling errors between the linear solution. For example, if scaling the linear response of a cell known to exhibit significant 2D effects to a fixed *arc height* results in an *arc width* deviating from the 1D model by a factor ϵ, scaling errors on the order of $(1+\epsilon)^2$ and $(1+\epsilon)^3$ would be expected for U_{22} and U_{33}, respectively. Figure 3.12 shows that for $\nu \leq 2$ and $\kappa \leq 10$, the effect of 2D transport on the magnitude of the nonlinear response is negligible for U_{22} and small for U_{33}, while their frequencies are more strongly affected.

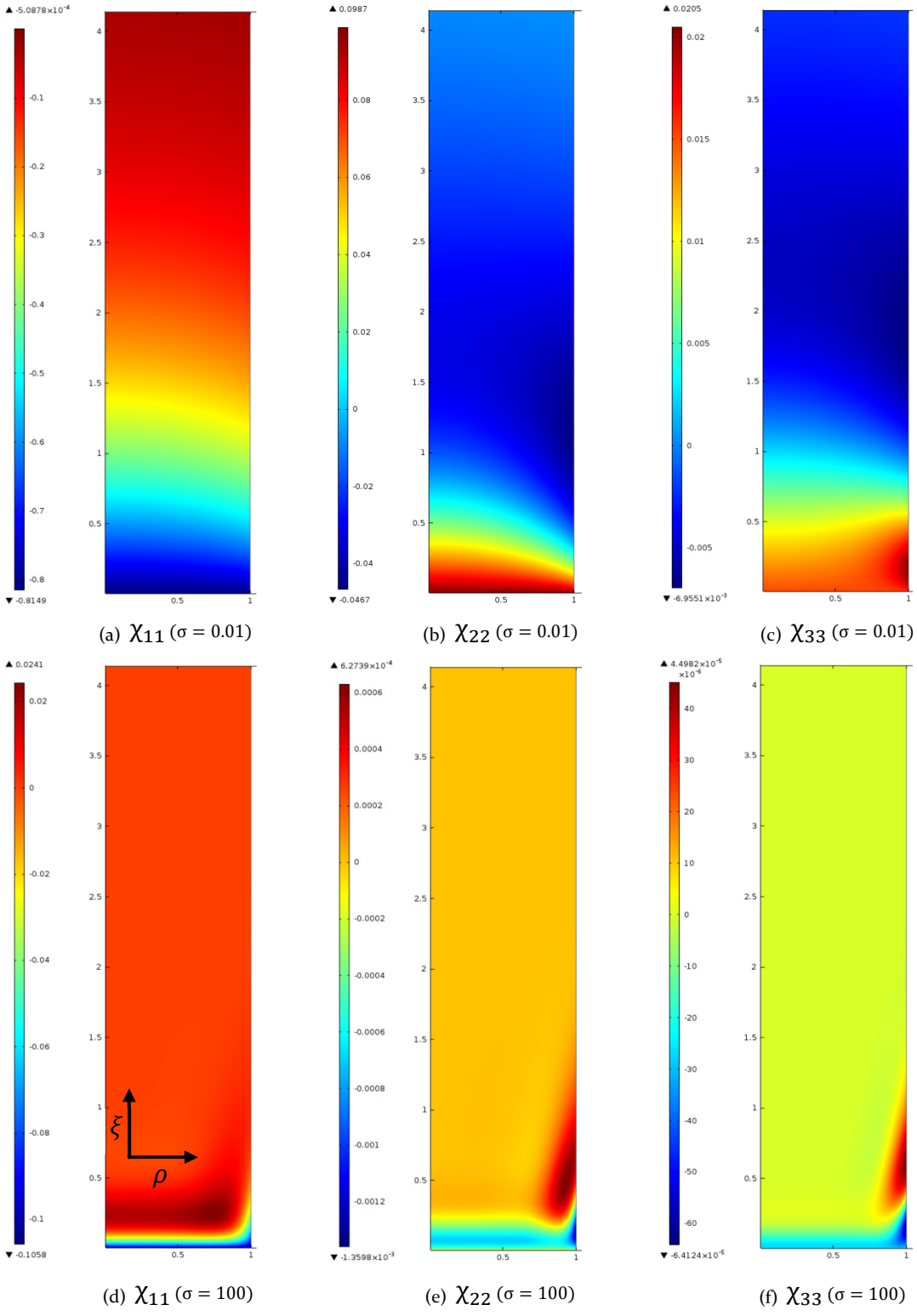

(a) χ_{11} (σ = 0.01) (b) χ_{22} (σ = 0.01) (c) χ_{33} (σ = 0.01)

(d) χ_{11} (σ = 100) (e) χ_{22} (σ = 100) (f) χ_{33} (σ = 100)

Figure 3.10: The 2D dimensionless vacancy concentration profiles for χ_{11} (left), χ_{22} (middle), and χ_{33} (top) are evaluated at $\sigma = 0.01$ (top) and $\sigma = 100$ (bottom) with $\kappa = 1$, $\nu = 2$, and $A_{0,s} = 1.01$.

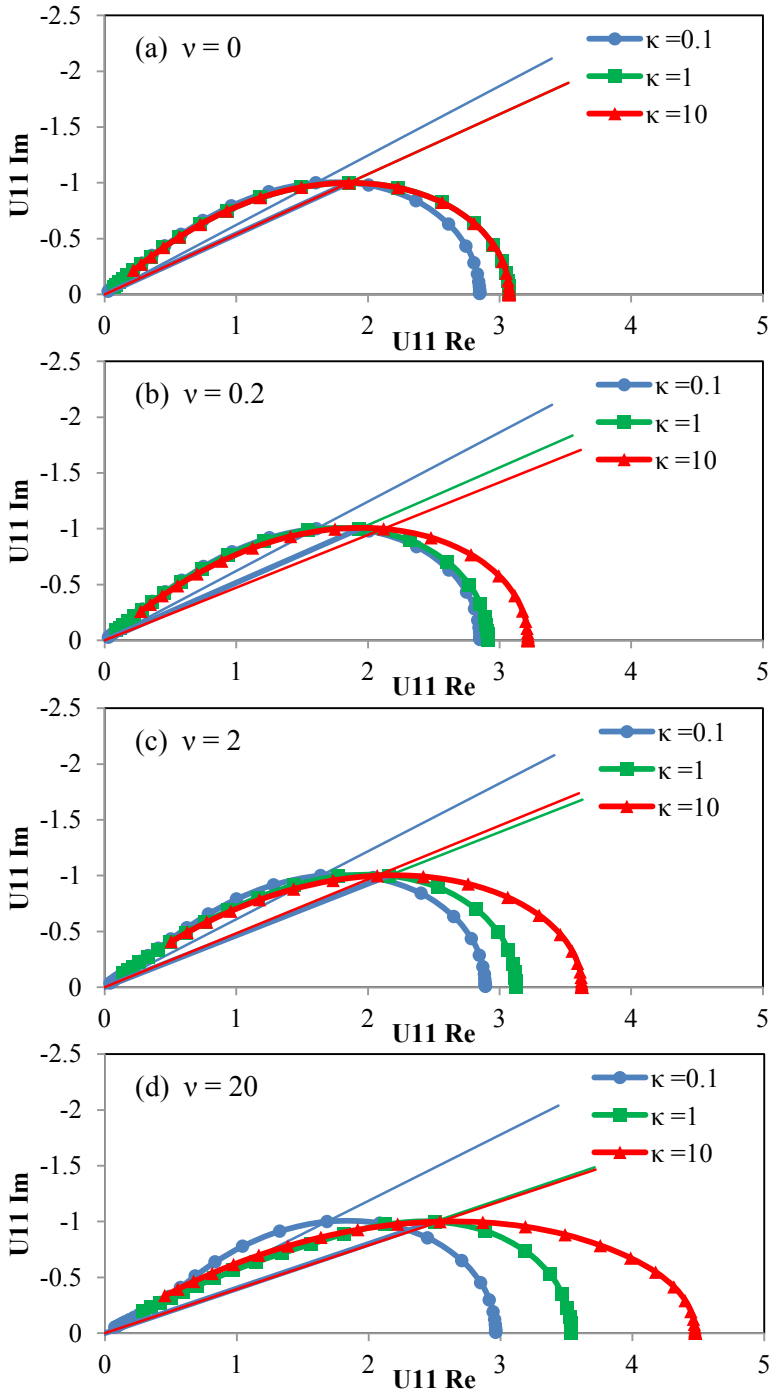

Figure 3.11: The linear impedance response for the 2D model using a skin layer approximation shows a depression of the arcs from a true Gerischer shape upon increasing κ and ν.

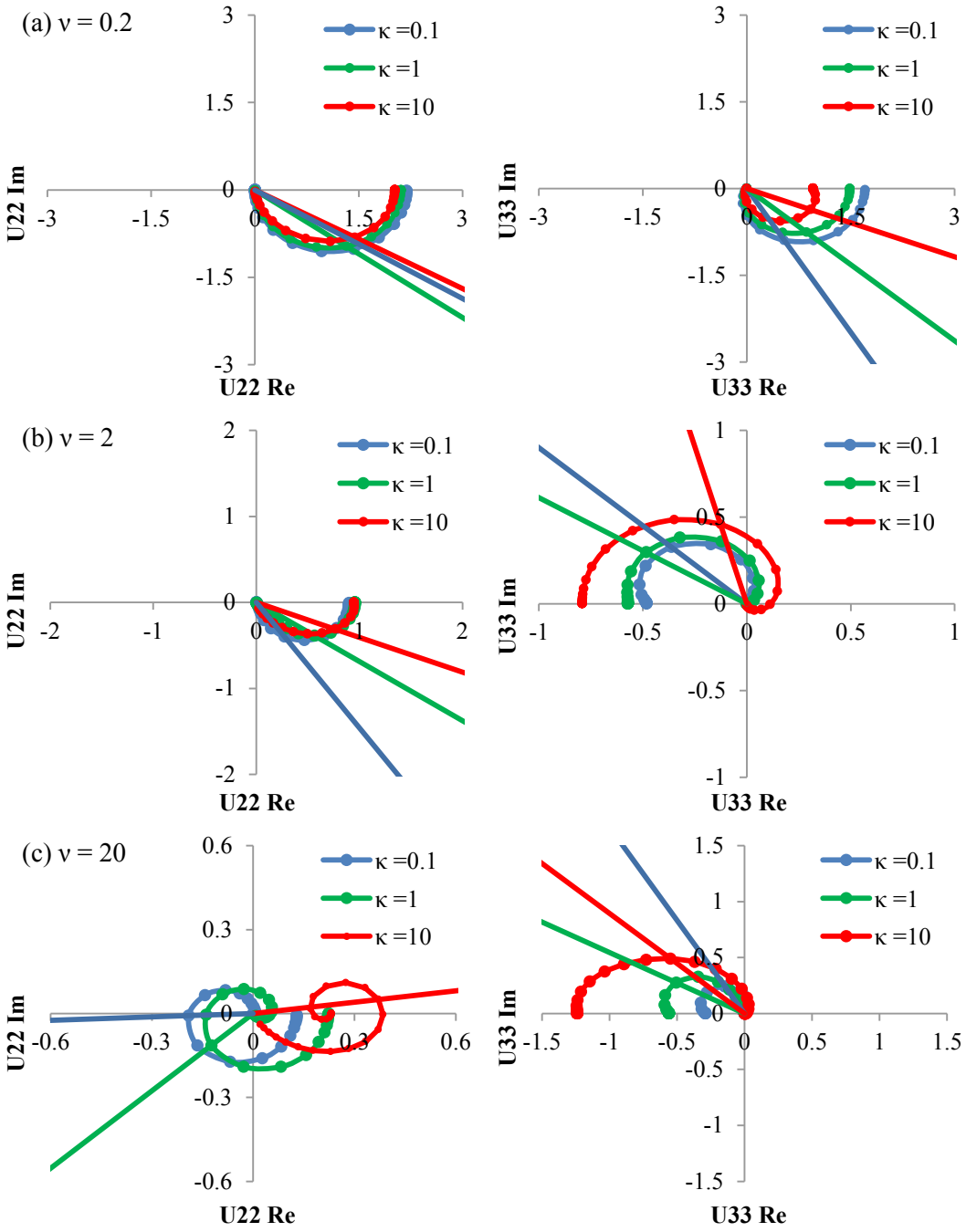

Figure 3.12: The second (left) and third-order (right) voltage responses are predicted for (a) $\nu = 0.2$, (b) $\nu = 2$, and (c) $\nu = 20$.

3.7 SUMMARY

This chapter develops a modeling framework applicable for studying oxygen reduction on porous p-type mixed conducting electrodes. The thermodynamic model presented in Chapter 2 is incorporated into a reaction-diffusion model considering different scenarios for surface diffusion mechanisms, varying surface thermodynamics, and multiple reaction rate laws. These phenomena are applied to both one-dimensional "macrohomogeneous" and two-dimensional "cylindrical" models predicting the linear and nonlinear electrochemical impedance response for this class of electrode material. The predicted nonlinear responses were particularly sensitive to varying assumptions for the rate-limiting phenomena.

The two-dimensional numerical model introduced a "skin layer" approximation of the electrode surface which greatly improved the model's ability to find a mesh-independent solution. This approximation also simplifies treatment of more complicated electrode geometries. Comparison with analytical models in two simplified limits (the nonlinear 1D model in the limit of $\kappa \to 0$ and the linear 2D model), supports the validity of the numerical surface approximation. The cylindrical model showed that, for $\kappa \leq 10$ and $\nu \leq 2$, the effects of two-dimensional transport appear as a depression of the linear impedance and slight shifts in frequencies of U_{22} and U_{33}, with a minor effect on the magnitude of the nonlinear responses.

4. Oxygen Reduction on Porous LCF-91 Electrodes

4.1 INTRODUCTION

In this chapter, the thermodynamic understanding of $La_{0.9}Ca_{0.1}FeO_{3-\delta}$ developed in Chapter 2 and the porous electrode models presented in Chapter 3, are used to analyze linear and nonlinear electrochemical impedance data collected on LCF|YSZ cells at various temperatures and oxygen partial pressures. By studying oxygen reduction on LCF-91 electrodes, the current understanding of the phenomena affecting cell performance for this class of p-type mixed-conducting electrodes is gaining interest for SOFC cathode and SOEC anode application can be extended.

4.2 EXPERIMENTAL

4.2.1 Symmetric Cell Fabrication

Approximately 1.3 g of 10 wt% Y_2O_3-doped ZrO_2 (YSZ, Zircar Inc.) was uniaxially pressed in a 1.8 cm diameter die at 5,000 psi for 4 minutes, then fired at 1600°C for four hours, ramping at 2°C/min to produce a single electrolyte pellet.

The $La_{0.9}Ca_{0.1}FeO_{3-\delta}$ electrode powder studied in this work was fabricated by Air Products and Chemicals, Inc. via solid-state reaction. Powders of lanthanum oxide, calcium carbonate, and iron oxide were blended, then calcined at 1190°C for 10 hours. The resulting coarse powder was subsequently milled via hammer, attrition,

and vibratory processes resulting in a surface area of approximately 6 m^2/g. This powder was fired at 1200°C for 36 hours and then cooled to room temperature over a period of 12 hours to ensure equilibration with air. The powder was mixed with organics (α-terpineol, ethyl cellulose, oleic acid) and three-roll milled, resulting in an electrode ink with a 50% solids loading. The ink was printed on both sides of the electrolyte pellet using a stainless steel screen mesh resulting in a wet thickness of ~20 μm. A reference electrode was painted around the pellet circumference using a paint brush. The symmetric cell was then fired with 100 sccm dry air at 1050°C for 30 min, ramping 1°C/min up and 2°C/min down. The finished cell, shown in Figure 4.1, had a superficial electrode area of 0.26 cm^2.

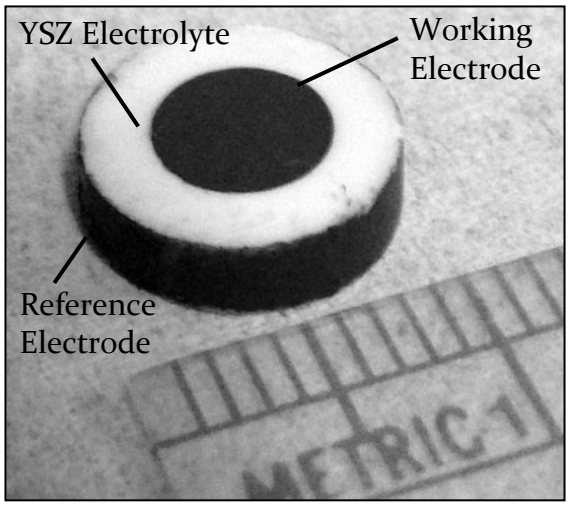

Figure 4.1: A picture of a symmetric cell used in electrochemical testing shows LCF-91 working (identical counter not shown) and reference electrodes on a YSZ pellet.

4.2.2 Cell Characterization

The cross section of the LCF-YSZ interface was then observed via SEM after fracturing a symmetric cell in half. Figure 4.2 shows a well-adhered electrode with good inter-particle contact, ~12 μm thickness, and particles ranging from 0.2-1 μm diameter.

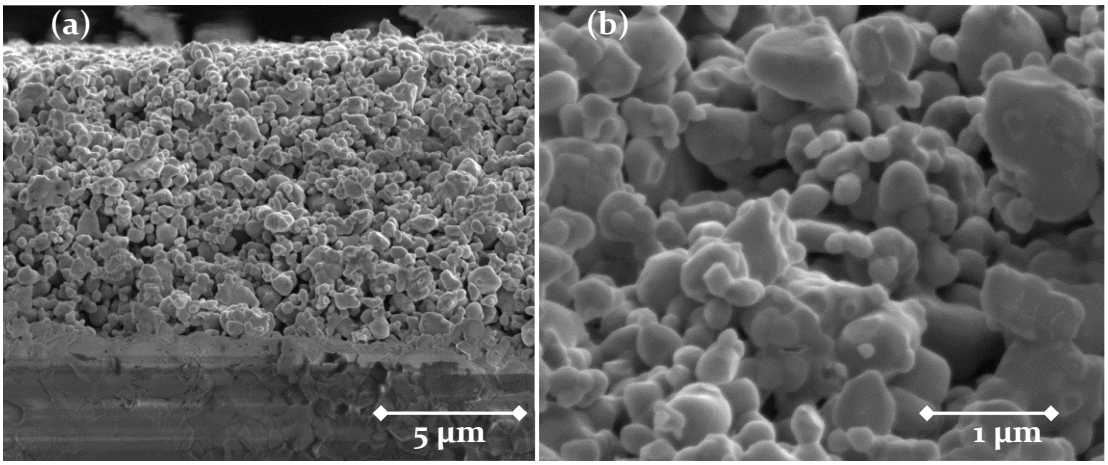

Figure 4.2: SEM of (a) the electrode-electrolyte interface shows a cell thickness between 10-15 µm and good electrode contact to the YSZ, and (b) shows particle diameters ranging from 0.2-1 µm.

In order to assess the stability of the LCF-YSZ interface, 50-50 wt% samples of LCF & YSZ were sintered in oxidizing conditions as described in Chapter 2, showing that powder X-ray diffraction was unable to detect additional phases. In addition to tertiary phase formation, electrode-electrolyte reactions can take the form of cation incorporation into the opposing phase [25]. To test for this, energy-dispersive X-ray spectroscopy (EDS) was performed on the fractured cell using an Oxford Instruments Silicon Drift Detect X-Max^N attached to the SEM chamber, and a beam voltage of 20 kV. The elemental mapping of the EDS results, shown in Figure 4.3, qualitatively shows a clear separation of electrolyte (Y, Zr) and electrode (La, Ca, Fe) species at the interface. The non-uniform distribution of the interface into the plane of detection limits the positional accuracy of EDS, accounting for some noise in the elemental concentrations near the interface. The only elemental map possibly indicating migration into the opposing phase is that of calcium, the least sensitive of those pictured to EDS. Figure 4.3 does not indicate significant incorporation of Y^{4+} into the perovskite B-site, nor does the XRD spectra indicate a peak shift from the corresponding increase in unit cell volume, as observed for the LSF-20|YSZ system [25].

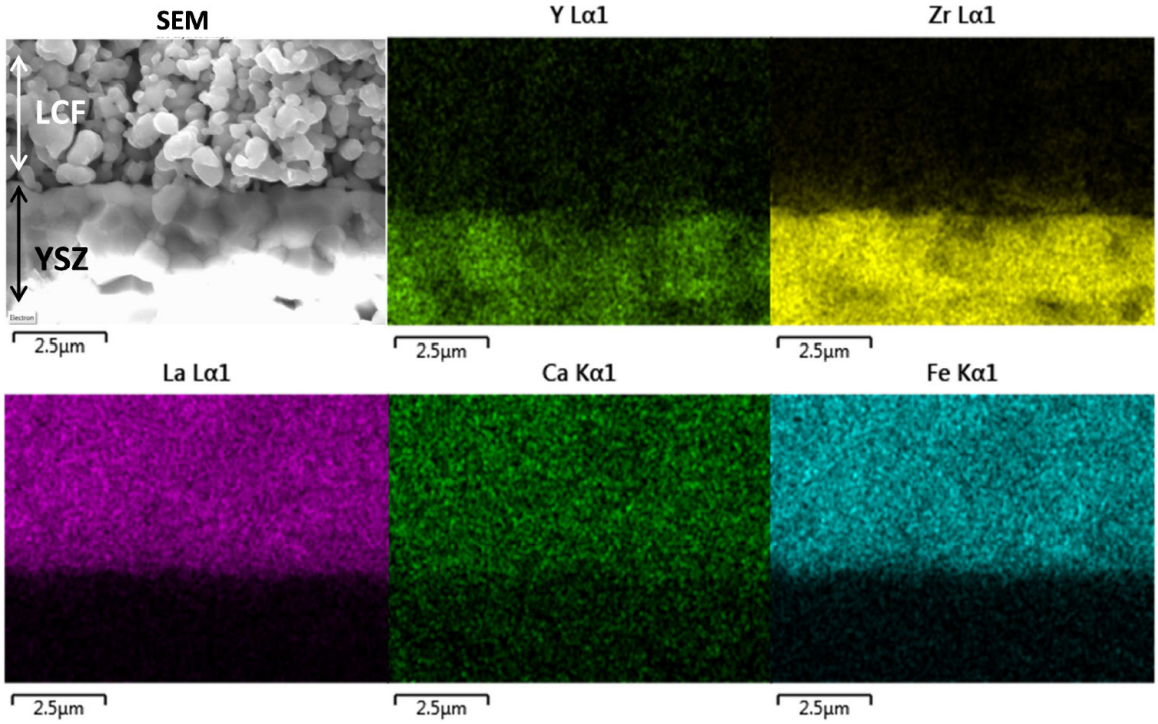

Figure 4.3: The elemental mapping from EDS based on the 20 kV SEM image in the top left shows a clear separation of electrolyte (Y, Zr) and electrode (La, Ca, Fe) species at the interface.

4.2.3 Impedance Measurements

The working and counter electrodes of the symmetrical cell shown in Figure 4.1 were contacted with gold mesh current-collectors, and the reference electrode was wrapped in gold wire. The cell was placed in a NorECs Probostat, as shown in Figure 4.4 and connected to a Solartron 1287a potentiostat. The gas inlet was positioned just under the cell, and the outlet was placed at the bottom of the larger sealed alumina tube, encouraging an even gas distribution near the cell. The outlet stream was fed to a Pt|YSZ|Pt oxygen sensor operating at 750°C to confirm the gas composition of 1%, 21%, or 100% O_2, with a balance of nitrogen, fed at 50 sccm. A blend of 1% O_2 and balance helium was used at 750°C to rule out the possibility of gas phase limitation under the most dilute conditions.

Nonlinear electrochemical impedance spectroscopy (NLEIS), described in detail by Wilson *et al.* [39], was performed on the half-cell arrangement shown in Figure 4.4 for all gas concentrations at 700°, 750°, and 800°C. Galvanostatic zero-bias AC perturbations corresponding to half-cell voltage response amplitudes between 10 mV (most linear) to 120 mV (most nonlinear) and perturbation frequencies ranging from 100 MHz to 5 mHz were performed once the system was allowed to equilibrate with the new gas and temperature environment for at least 24 hours. A full amplitude (20) and frequency (10/decade) sweep at a single temperature and p_{O_2} lasted between 4 and 12 hours depending principally on the lowest frequency selected.

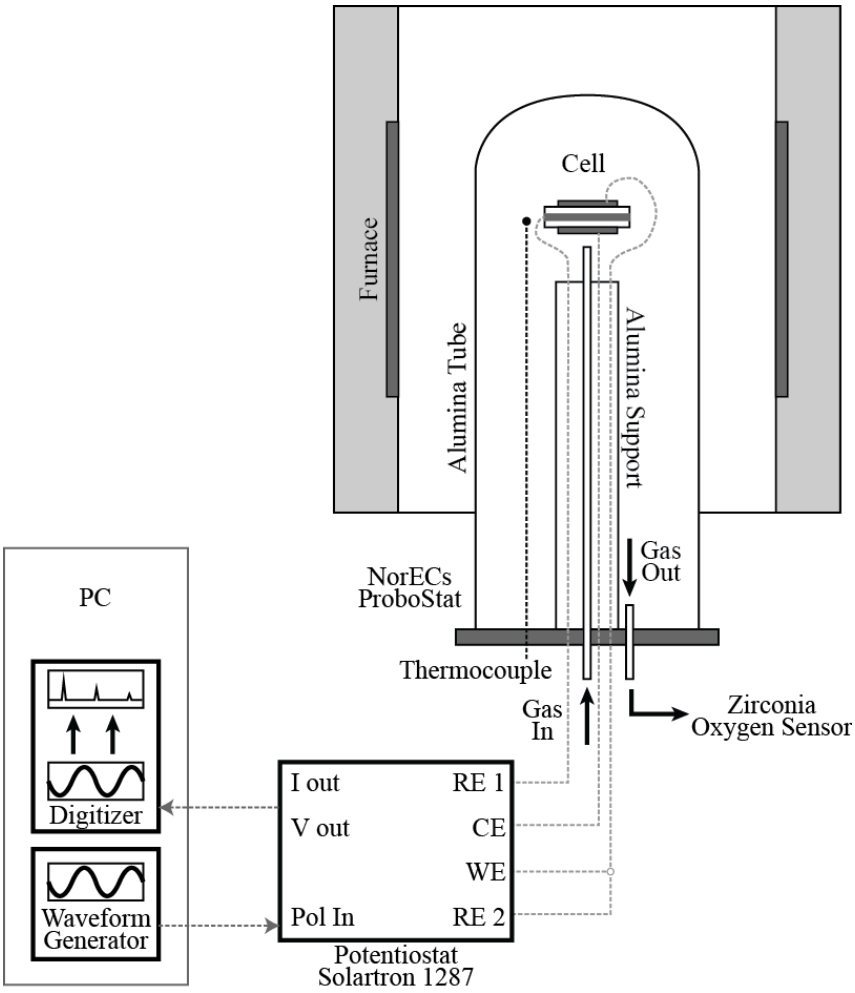

Figure 4.4: The NLEIS setup consists of a Probostat housing the gas and electrical feed-throughs to the cell, connected to a potentiostat applying a current waveform (generated by a National Instruments PCI-5421) and measuring the voltage response (sent to an NI PCI-5122 High-Speed Digitizer).

4.3 RESULTS & DISCUSSION

4.3.1 Linear Impedance Spectroscopy Results

The half-cell performance of LCF|YSZ cells can be analyzed by measuring the EIS response under different temperature and p_{O2} conditions. Monitoring the dimensional groups of the linear response under these different experimental conditions—particularly the characteristic frequency and resistance, ω_c and R_c,

defined in the previous chapter—allows for a better understanding of kinetic and transport phenomena controlling overall performance.

Figure 4.5 shows the area-specific linear EIS spectra taken from the full NLEIS dataset prior to nondimensionalizing, measured in 1%, 21%, and 100% oxygen environments at 700, 750, and 800°C. The series resistance (R_Ω), presumed to correspond to ohmic transport losses in the electrolyte has been subtracted. While the shape resembles the linear Gerischer response of a 1D model predicted in the previous chapter, supporting a co-limitation of kinetics and diffusion, some differences exist. The spectra, particularly at 0.01 atm, reveal the presence of a second feature at high frequencies (closest to the origin), potentially corresponding to an electrode-electrolyte interfacial resistance. This process occurs at frequencies higher than that affecting the nonlinear spectra discussed in the following section, making its presence insignificant beyond obscuring the *arc width* of the chemical feature. For this reason, the imaginary *arc height*, R_c, was chosen as the characteristic resistance.

In order to quantify changes in cell resistance and time constant, Figure 4.5 compares the temperature and p_{O2} dependence of R_c and ω_c. The characteristic cell resistance exhibits a weak inverse p_{O2} dependence and a strong thermal activation (~ -220 kJ/mol). Compared to that of LSC-82, LCF-91 shows values of R_c several times larger, occurring at longer time scales, indicating that LCF-91 is a relatively poor oxygen electrode [38].

Figure 4.5b shows that the peak frequency (ω_c) of the linear response, representing the time constant ($1/\omega_c$) of the chemical feature, exhibits a strong p_{O2} dependence, $\omega_c \propto p_{O2}^n$, where $n \approx 0.8$ at 700-750°C and $n \approx 0.96$ at 800°C. The strong dependence of ω_c on p_{O_2} is close to what has been observed for LSC-64 ($n \approx 0.7–1$) and LSF-91 ($n \approx 0.5–1$), but the lack of p_{O_2} dependence on R_c ($n \approx$ -0.05–-0.02) deviates from the inverse dependence observed for LSC-64 ($n \approx$ -0.4–-0.7) and LSC-82 ($n \approx$ -0.15–-0.4) [36], [38]. Based on the discussion in Section 3.5.1 assuming the bulk thermodynamics of Chapter 2, the p_{O2} dependence of ω_c at 700

and 750°C falls somewhere between that predicted by dissociative adsorption ($\mathcal{R}_{0,da} \propto p_{O2} {x_v^0}^2$, $n \approx 0.5$) and chemisorption ($\mathcal{R}_{0,ca} \propto p_{O2} x_v^0$, $n \approx 1$) rate laws, while at 800°C the cell is more consistent a chemisorption rate law. Similarly for R_c, $\mathcal{R}_{0,da}$ predicts $R_c \propto p_{O2}^{-1/4}(1+\nu)^{-1/2}$, while $\mathcal{R}_{0,ca}$ predicts $R_c \propto (1+\nu)^{-1/2}$ for the 1D model. The observed weaker p_{O2} dependence of R_c is more consistent with that of a chemisorption rate law. This analysis assumes the surface thermodynamics mirror that of the bulk, measured in Chapter 2, and that any transient behavior is negligible. The validity of both assumptions will be questioned later in this chapter.

Figure 4.6d plots the p_{O2} dependence of the capacitance of the chemical feature, $C = 1/\omega_c R_c$, showing a strong increasing upon decreasing $p_{O2}$for all temperatures. Kawada *et al.* demonstrate that changes in bulk vacancy concentration (δ) with changing oxygen environment ($2\mu_O = \mu_{O_2}$) produce a "nonstroichiometric capacitance" (C_δ) for kinetically-limited dense films of LSC-64 [78],

$$C_\delta = -\frac{4F^2 L_\delta}{V_m(1-\epsilon)}\frac{\partial \delta}{\partial \mu_O} = \frac{12F^2 L_\delta}{V_m(1-\epsilon)RT}\frac{x_v}{A(x_v)}, \qquad 4.1$$

where L_δ is the length of the active electrode region undergoing changes in nonstoichiometry and V_m is the molar electrode volume. Upon assuming the equilibrium values for x_v and $A(x_v)$ to be those given in Chapter 2, a porosity of $\epsilon \approx 0.5$, and that the measured capacitance, C, in Figure 4.6d is independent of diffusional effects and represents the bulk nonstoichiometric capacitance of Eq. 4.1, the length of the active region of the electrode can be roughly estimated. Figure 4.7 shows that the active region of the electrode increases with vacancy concentration at constant temperature and decreases at higher temperatures. More importantly, based on these assumptions, the active electrode region extends less than the average particle diameter from the triple phase boundary, suggesting that radial transport effects will become important, and a 1D macrohomogeneous model may not sufficiently capture these phenomena.

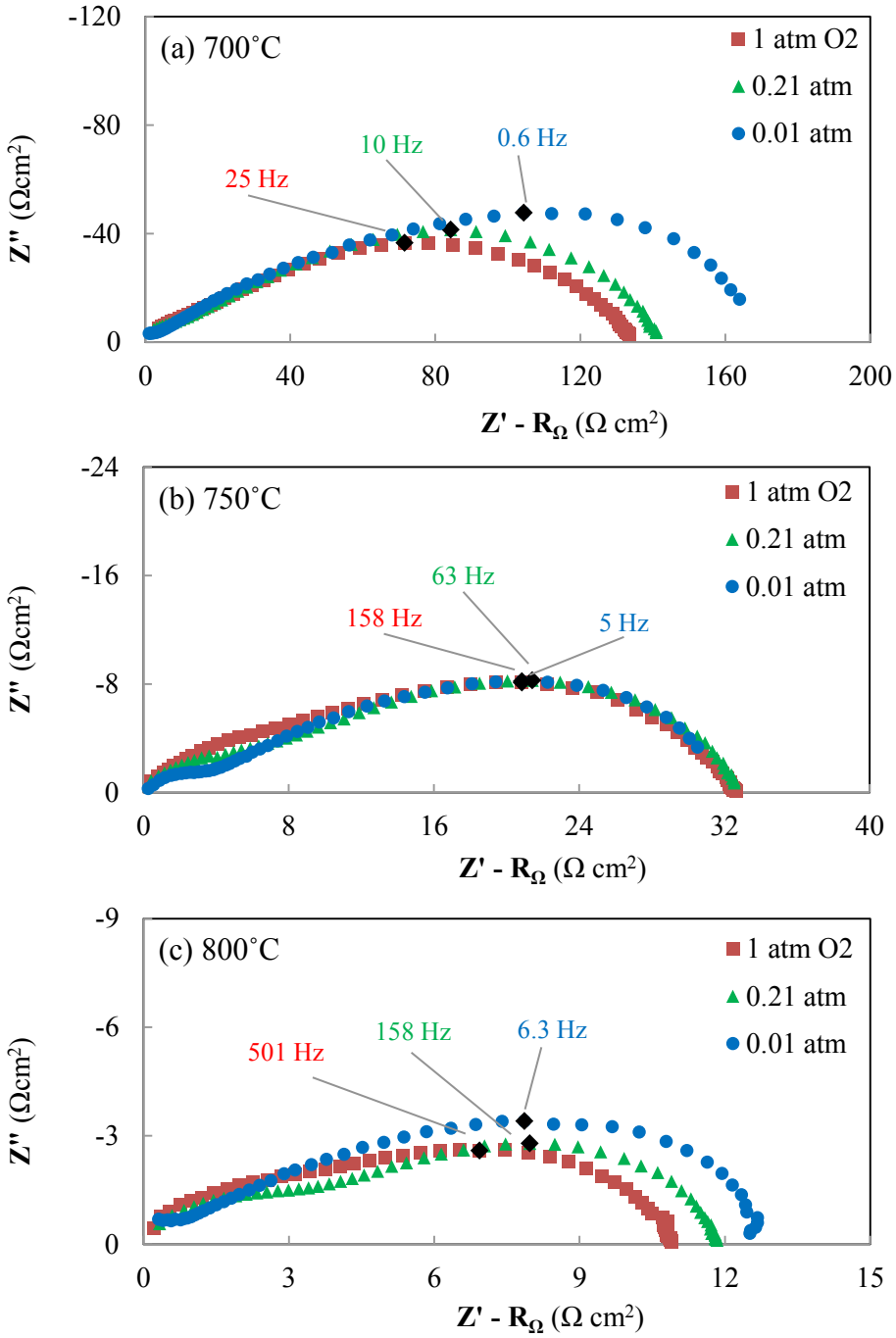

Figure 4.5: The EIS spectra at 0.01, 0.21, and 0.01 atm O_2 are shown at (a) 700, (b) 750, and (c) 800°C.

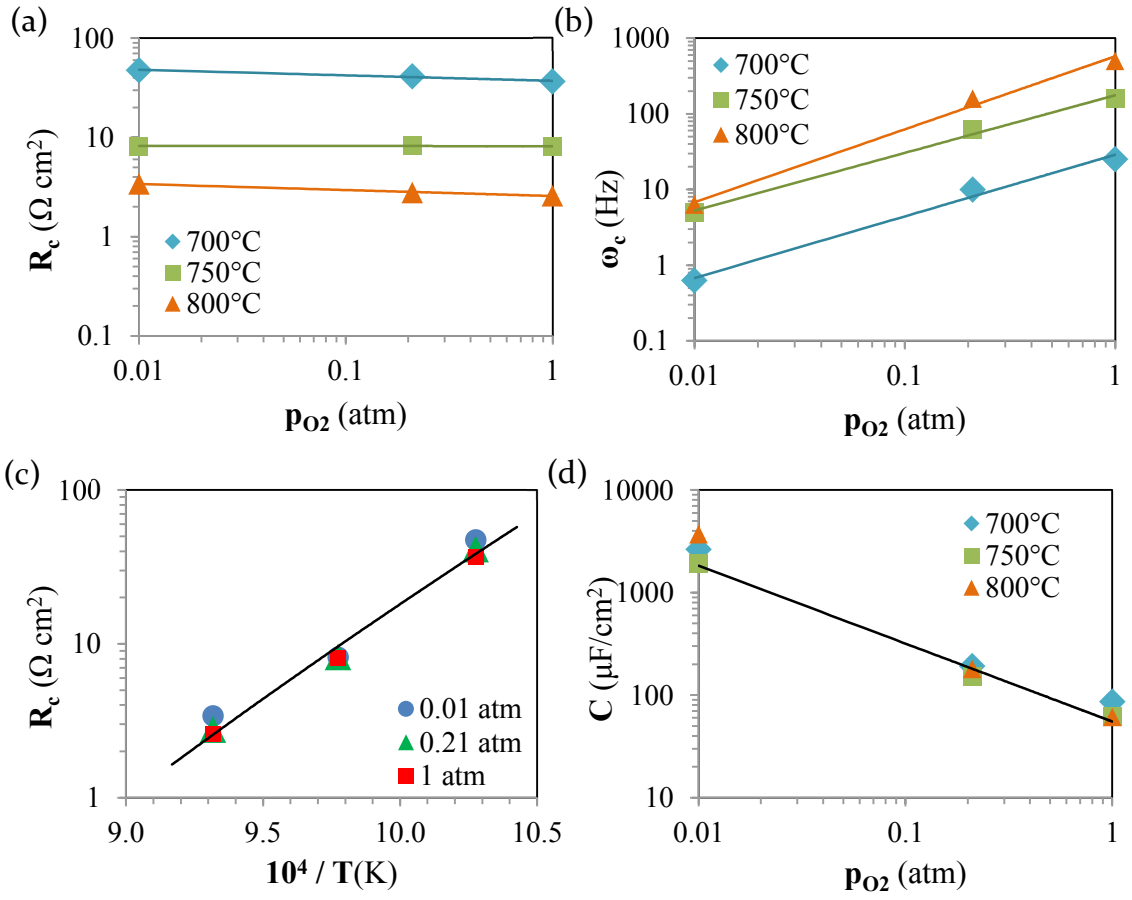

Figure 4.6: Measured values of (a) R_c show a weak decrease with increasing p_{O2} and (c) strong thermal activation (~ -220 kJ/mol). (b) The peak frequency ω_c shows a strong increase with increasing p_{O2}, while (d) C_{chem} shows a strong inverse dependence on p_{O2}.

Comparing the shape of the spectra in Figure 4.5 to the Gerischer response predicted by the 1D model in the previous chapter, the arcs appear vertically depressed and the shape at low frequencies deviates from a semicircle. Figure 4.8 quantifies this discrepancy by plotting the deviation of the observed R_c-scaled *arc width*, $U_{11}(\sigma = 0)$, to that predicted by a 1D model across experimental conditions, illustrated in the inset. The failure of the 1D model to correctly predict the shape of the observed spectra ranges from 20-49%. A portion of this error is caused by the high-frequency feature not accounted for in the model. Even in the spectra where this feature was negligible (1% & 21% O_2 at 700°C), 1D errors of 20% are observed.

As shown by the 2D cylindrical model in Chapter 3, and by Lu *et al.* for LSC-82, these observations are consistent with cases where significant surface diffusion and kinetics relative to bulk diffusion ($\nu, \kappa > 0.1$) result in a large degree of two-dimensional transport [34]. For example, Figure 3.11c shows that for $\nu = 2$ and $\kappa = 10$, the 1D model underestimates $U_{11}(\sigma = 0)$ by 26%, compared to the 2D model.

Transient Behavior

A major factor complicating the analysis of rate-limiting phenomena from dimensional EIS data described in this chapter is the transient nature of the electrochemical cells. Long-term degradation, as well as slow equilibration processes upon changing temperature and p_{O2} not explicitly addressed in presented porous electrode models, are not easily separable from the processes of interest.

Figure 4.9 tracks the characteristic resistance and frequency of a particularly transient LCF|YSZ cell measured over 800 hours of exposure to different oxygen gas compositions at 700°C. At $t < 0\ hrs$, the cell was held at 650°C in 100% O_2 for 24 hours. While changing p_{O2} has an immediate effect on R_c and ω_c, continued exposure results in relaxation processes on the order of days, decreasing in performance upon switching to higher p_{O2} and increasing in performance upon switching to lower p_{O2}. On the order of hundreds of hours and across different p_{O2} steps, all three p_{O2} appear to approach single steady-state values, suggesting a long-term equilibration process, such as surface cation rearrangement, affecting electrode performance.

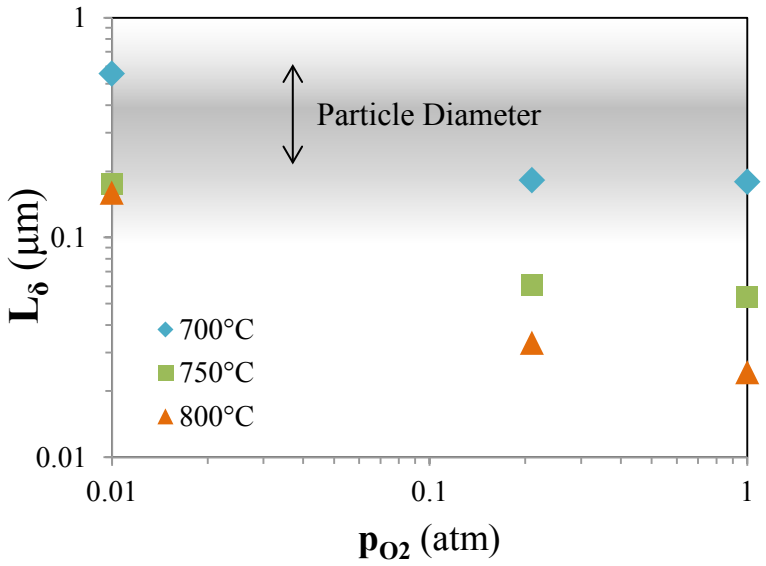

Figure 4.7: The distance that the active region of the electrode from the triple phase boundary, L_δ, estimated from changes in bulk nonstoichiometry, is compared to the average electrode particle diameter.

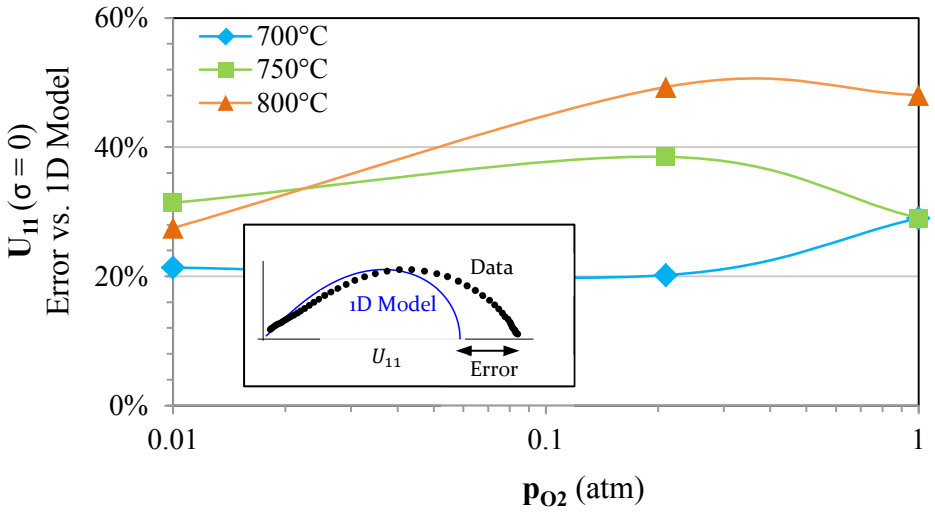

Figure 4.8: The degree of "flattening" of the observed spectra relative to that predicted by a 1D model, defined in the inset, is reported for all conditions. No attempt is made to remove the high-frequency features shown in Figure 4.5 from the arc width.

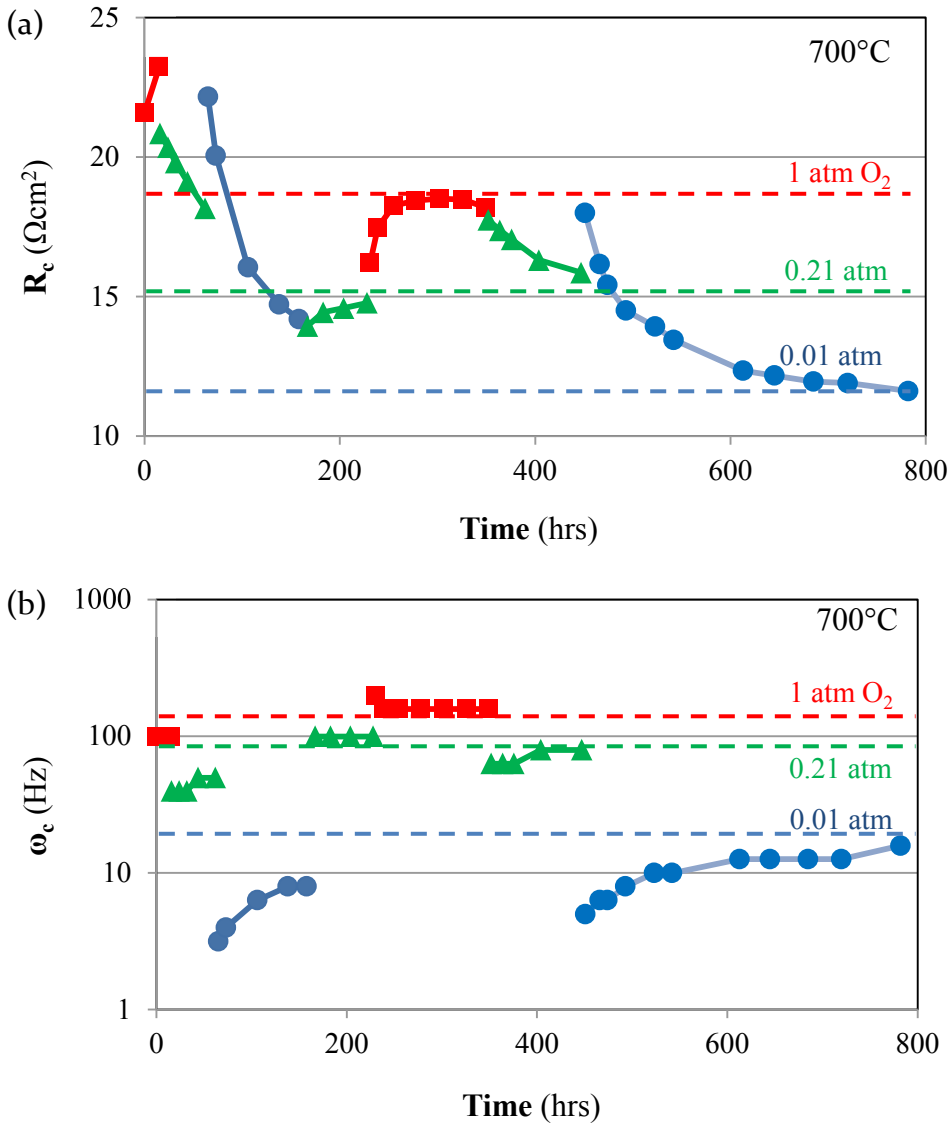

Figure 4.9: The characteristic resistance, R_c, and frequency, ω_c, of a particularly transient LCF|YSZ cell is monitored over 800 hours in 700°C upon cycling p_{O2}.

In order to avoid effects of long-term degradation, most kinetic studies vary temperature and p_{O2} quicker than the relaxation time constants shown in Figure 4.9. Comparing values of R_c and ω_c at different experimental conditions along different points of this slow equilibration process is therefore greatly complicated.

Lu *et al.* has shown for LSC electrodes that, over periods of hundreds of hours in air, while the characteristic frequency and resistance undergo significant changes,

their *interdependence* remains fixed at a constant temperature [79]. Figure 4.10 re-expresses the data in Figure 4.9 as the time constant $t_c = 1/\omega_c$ *versus* R_c (after scaling to the characteristic resistance for bulk diffusion $R_D = \frac{RT}{4F^2}\frac{1}{c_0 x_v^0 D_v a} \propto p_{O2}^{1/2}$, to allow for comparison with Ref. [79]). This shows that, regardless of the transient behavior in Figure 4.9, all points exhibit the same $t_c \propto (R_c/R_D)^2$ dependence in Figure 4.10. By comparing this relationship to the trends predicted by a 2D model, Lu explained this relationship as a variation in the surface rate coefficient $k(T)$ (e.g. $\mathcal{R}_{0,da} = k_{da}(T)\, p_{O2} x_v^{0\,2}$), possibly caused by a change in the surface structure or composition [34], [79]. Additionally, comparing the parametric dependence with p_{O2} shown in Figure 4.10 to the ν dependence in Ref. [34] implies ν increases with increasing p_{O2}, supporting an interstitial surface diffusion mechanism.

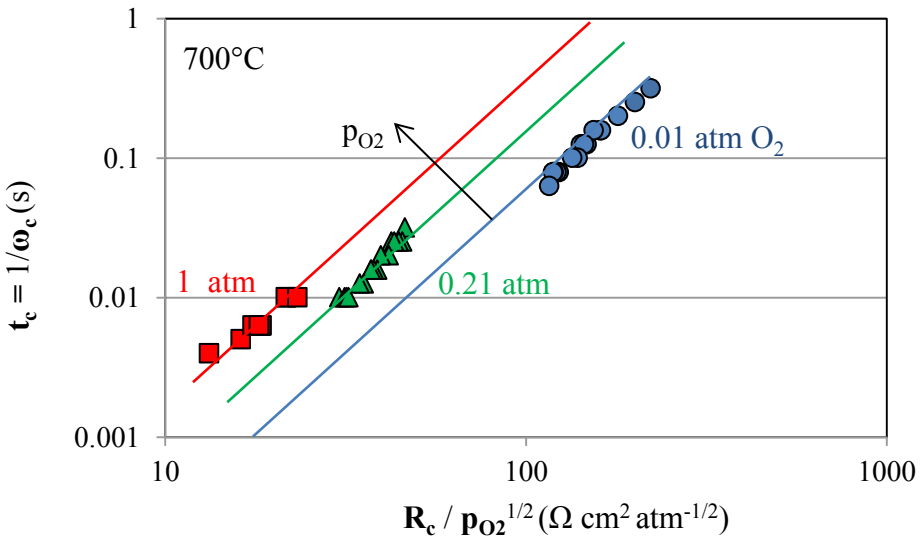

Figure 4.10: Measuring the impedance over long periods of time and varying p_{O2} reveals a strong connection between t_c and R_c.

4.3.2 Nonlinear Impedance Spectroscopy Results

The nonlinear voltage response was scaled to the measured linear response using R_c and ω_c, as described in Ref. [39]. The resulting measured second and third

harmonic voltage response coefficients, U_{22} and U_{33}, are therefore directly comparable to those modeled in Chapter 3. Figure 4.11 shows the measured spectra of U_{22} and U_{33} for the same cell shown in Figure 4.5. Phasor lines extending from the origin intersect the linear peak frequency, ω_c. The spectra show a consistent clockwise rotation of the U_{22} phasor and counter-clockwise rotation of the U_{33} phasor with increasing p_{O_2}. Both harmonics show the low frequency intercepts moving in the negative real direction with increasing p_{O_2}. These observed trends are qualitatively identical to those measured for LSC-82 at 650-750°C and 0.01-1 atm 0_2 [38].

In order to interpret these data, the observed spectra are compared to the various 1D modeling scenarios discussed in the previous chapter. The magnitude and timescale of U_{22} and U_{33}, along with their dependence on increasing p_{O2}, serve as indicators of a model's degree of success. For all cases, the thermodynamics of the electrode bulk, represented by A_0, are fixed to the measured values of bulk LCF-91 presented in Chapter 2.

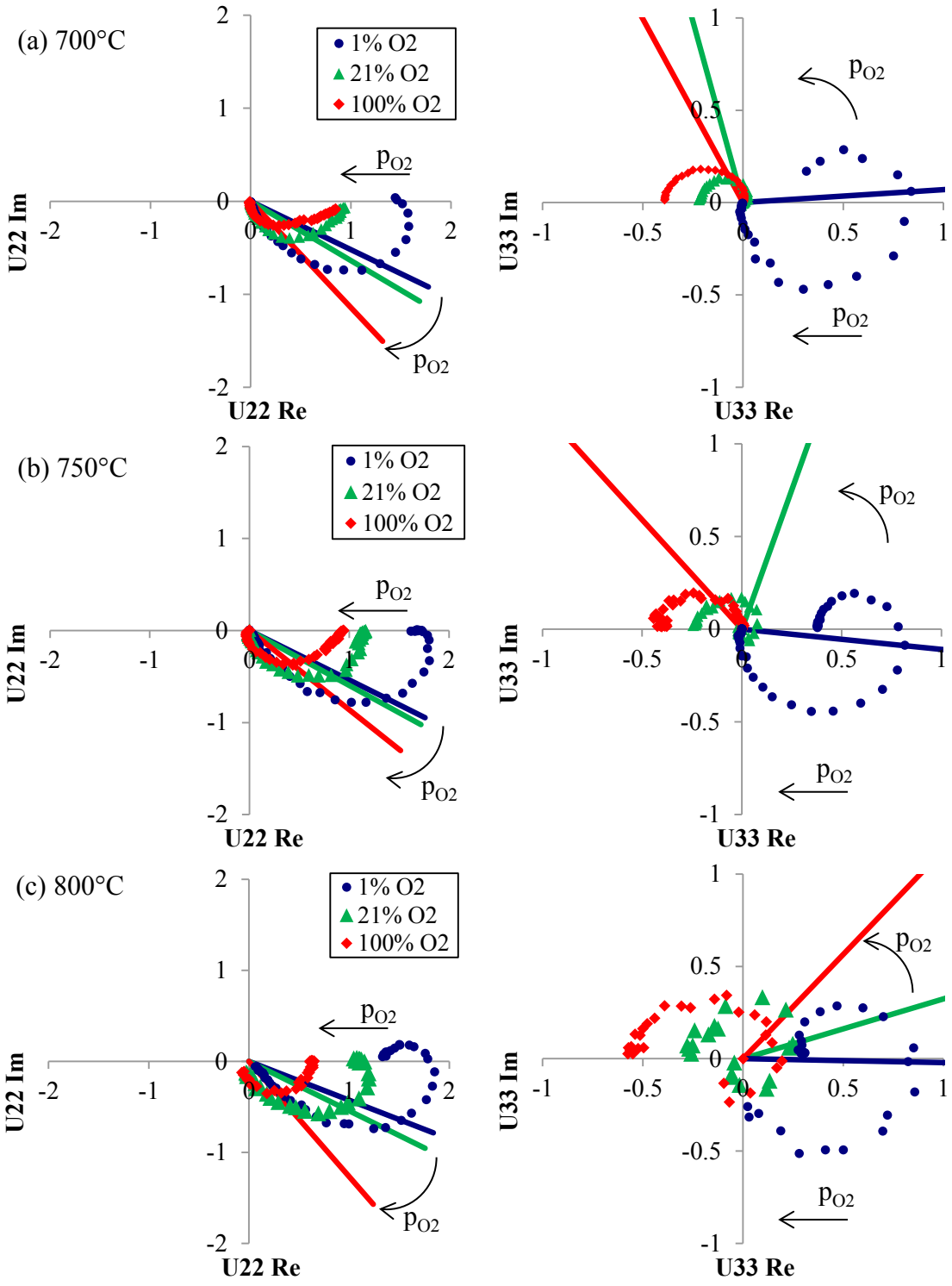

Figure 4.11: The measured nonlinear impedance response at p_{O_2} of 1 (red), 0.21 (green), and 0.01 atm (blue) for (a) 700°, (b) 750°, and (c) 800°C, with arrows indicating trends of phasor line rotation and magnitude shifts with increasing p_{O_2}.

Comparison to 1D Macrohomogeneous Model: Bulk Diffusion Only

The simplest model described in Chapter 3 ignores surface diffusion ($\nu = 0$) and fixes the surface thermodynamics, represented by $A_{0,s}$, to that of the electrode bulk (i.e. $A_{0,s} = A_0$). For this scenario, no fitting parameters exist. Figure 4.12 reveals that this "base case" is unable to capture the data's strong p_{O_2} dependence for either a chemisorption or dissociative adsorption rate law. Additionally, dissociative adsorption predicts harmonic responses significantly larger than those observed, particularly for U_{33}, while chemisorption predicts responses closer in magnitude. Both rate laws predict smaller magnitudes of U_{22} and U_{33} upon increasing A_0 (decreasing p_{O2}), contradicting the measured trend; because of this, even allowing the surface to be more nonstoichiometric than the bulk ($A_{0,s} > A_0$) for $\nu = 0$ will not capture the observed trends. The comparison in Figure 4.12 shows that, for the rate laws discussed, a model considering only bulk transport and bulk thermodynamics is inconsistent with measured spectra for oxygen reduction on LCF.

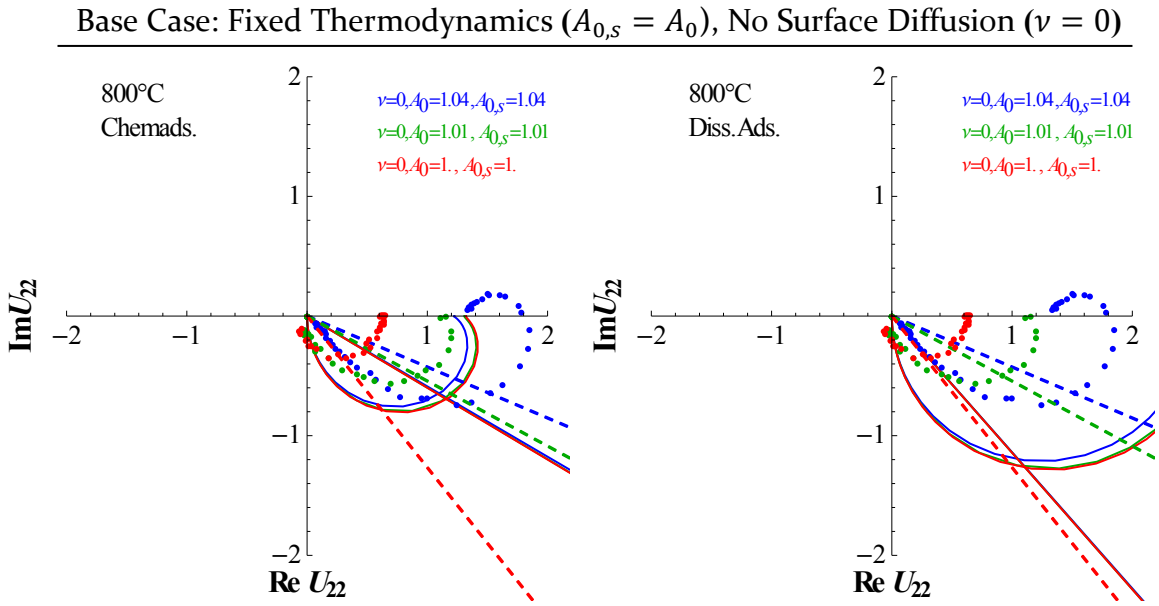

Figure 4.12: The measured U_{22} spectra (points, dashed lines) in 1% (blue), 21% (green), and 100% (red) O_2 environments are compared to modeled results (solid lines) assuming $\nu = 0$, $A_{0,s} = A_0$, and either chemisorption (left) or dissociative adsorption (right) rate laws.

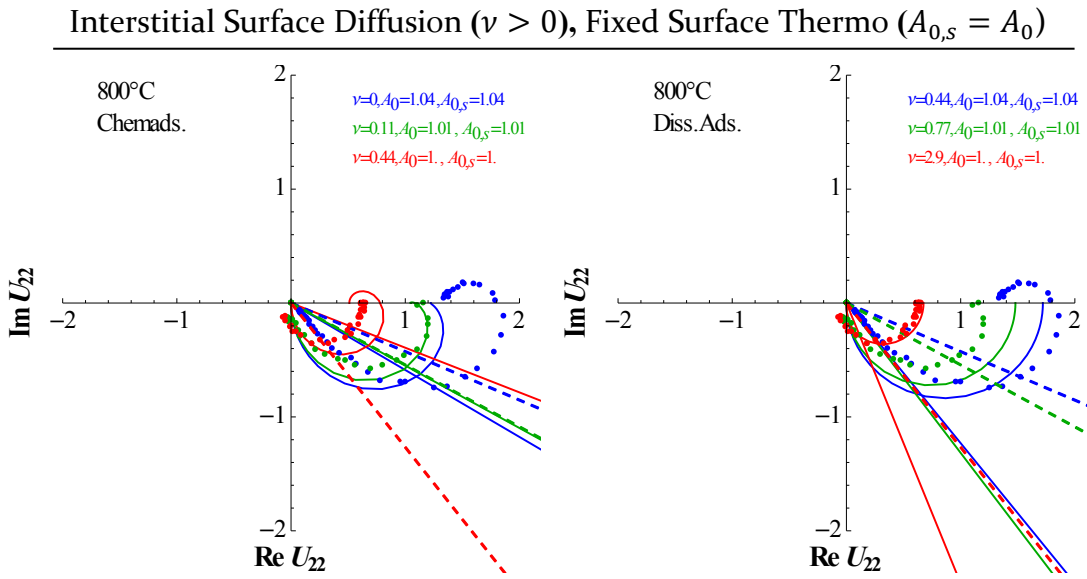

Figure 4.13: U_{22} for the 1D model (solid lines) is fit to the measured spectra (points, dashed lines) in 1% (blue), 21% (green), and 100% (red) O_2, by varying ν but fixing $A_{0,s} = A_0$ for both chemisorption (left) and dissociative adsorption (right) rate laws.

Enhanced Surface Thermodynamics and Surface Diffusion

Previous modeling efforts for LSC-64 and LSC-82 have suggested, particularly in the case of the latter, that the thermodynamics of the surface may differ relative to the bulk [38]. For these studies, in order to obtain quantitative agreement with the observed trends, $A_{0,s}$ was allowed to deviate from A_0, taking on values corresponding to a significantly more nonstoichiometric material. Depth-profile secondary ion mass spectrometry (SIMS) and Auger electron spectroscopy (AES) [38], as well as *in situ* X-ray photoelectron spectroscopy (XPS) provide evidence for A-site cation-enrichment at the gas-exposed surface [80].

Assuming interstitial oxygen surface diffusion, a simultaneous least-squares fit of both U_{22} and U_{33} was performed for all measured p_{O2} and temperature by varying ν and $A_{0,s}$. Figure 4.14 and Figure 4.15 show the results of these fits, assuming a chemisorption and dissociative adsorption rate law, respectively. Chemisorption was unable to capture observed phasor rotation for U_{22}, incorrectly predicting a counterclockwise rotation with increasing p_{O2}. Dissociative adsorption correctly modeled all observed trends, and yielded slightly better quantitative agreement.

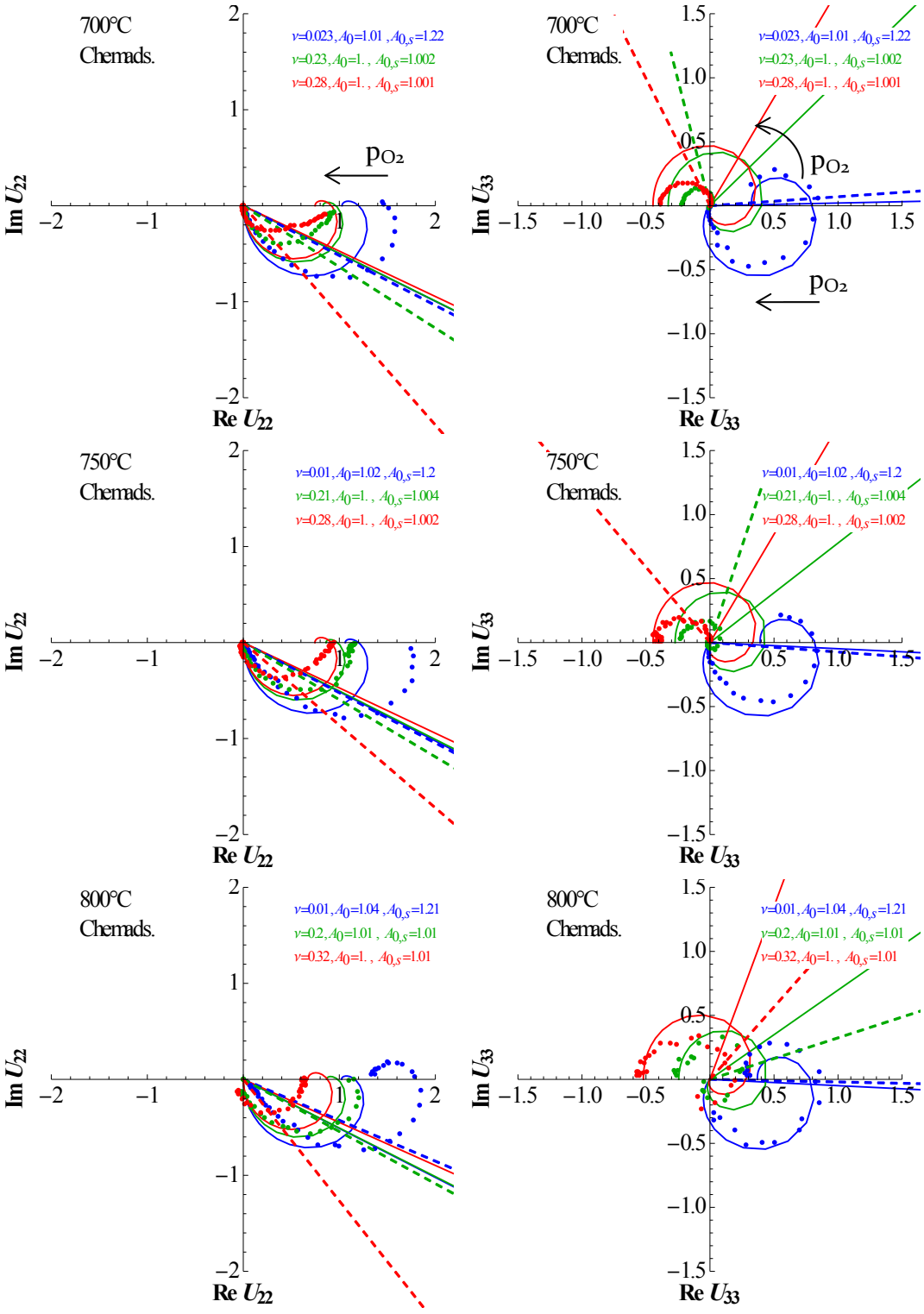

Figure 4.14: The model assuming surface interstitial diffusion and a chemisorption rate law (solid lines) is fit to the measured spectra (dashed lines) at 1% (blue), 21% (green) and 100% O_2 by varying ν and $A_{0,s}$.

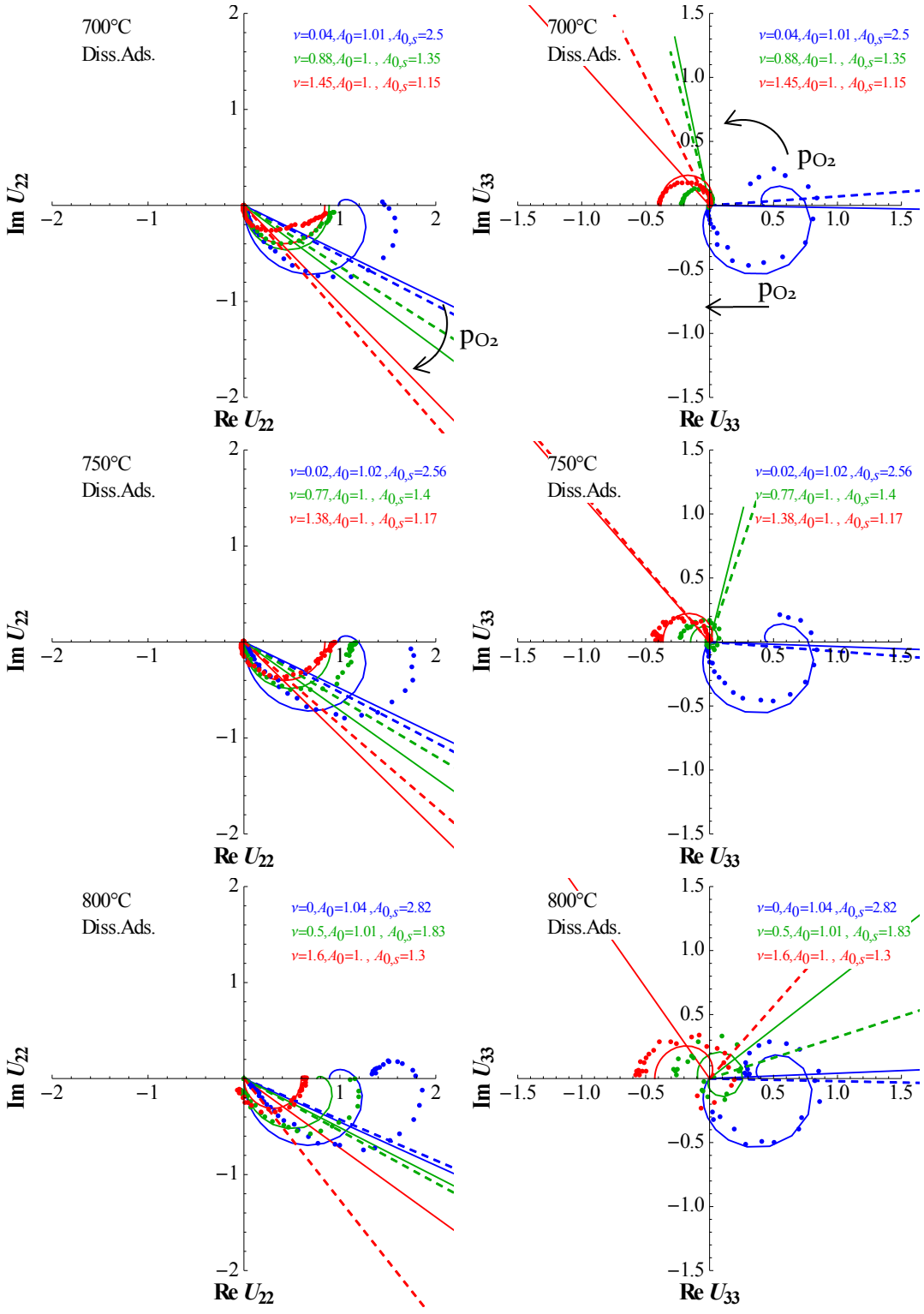

Figure 4.15: The model assuming surface interstitial diffusion and a dissociative adsorption rate law (solid lines) is fit to the measured spectra (dashed lines) at 1% (blue), 21% (green) and 100% O_2 by varying ν and $A_{0,s}$.

While ν and $A_{0,s}$ were freely fit in this study, their dependence on p_{O2} and temperature must be consistent with their physical interpretation. In the case of interstitial oxygen surface diffusion, $\nu = \frac{\Gamma_0 K_{\mathrm{eqm}} D_I}{R c_O D_v x_v^0 x_{v,s}^0}$, implying $\nu \propto p_{O2}$ if both x_v^0 and $x_{v,s}^0 \propto p_{O2}^{-1/2}$ in the limit of small vacancy concentration. Furthermore, all fit values of ν are less than 2. For the 2D cylinder model solved in the previous chapter, even at values of $\kappa = 10$ (fast kinetics relative to bulk diffusion), a negligible effect on the magnitude of U_{22} was observed, while U_{33} was ~55% *larger* than the 1D, suggesting a 2D model is not likely to improve the fits shown in Figure 4.15.

Thermodynamic surface enhancement is assumed to result from an increase in A-site dopant at the surface; $A_{0,s}$ must therefore be consistent with the p_{O2} and temperature dependence of LCF at an increased Ca-doping. Figure 4.16 shows the values of ν and $A_{0,s}$ corresponding to the best fit shown in Figure 4.15 for a dissociative adsorption rate law.

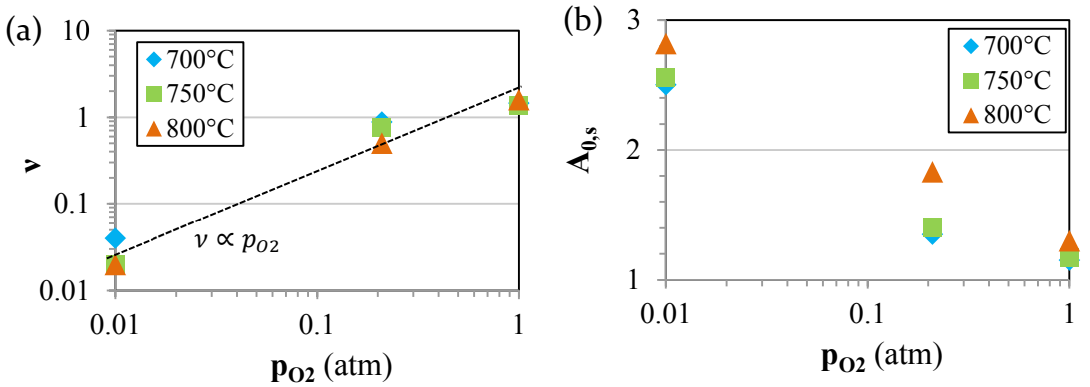

Figure 4.16: The best-fit values of (a) ν and (b) $A_{0,s}$ corresponding to Figure 4.15 are reported as a function of p_{O2} at 700, 750, and 800°C, with the expected p_{O2} dependence of ν shown for comparison.

In the case of ν, fit values are consistent with the predicted $\nu \propto p_{O2}$ dependence. However, the fit values of $A_{0,s}$, while qualitatively consistent in p_{O2} and temperature trends, results in values likely too high to be the result of calcium

surface segregation. While thermodynamic studies comparing the defect chemistry of LCF as a function of Ca dopant level currently don't exist, an approximation can be made by applying the weak Sr-dependence measured for ΔH_{ox}^{0} and ΔS_{ox}^{0} (defined in Chapter 2) for LSF to the model for LCF-91 [14]. Based on this estimation, even for the most reducing conditions of 1% O_2 and 800°C studied, $A_{0,s} > 2$ is not expected for any A-site composition. Instead of assuming an entirely entropic change in the free energy of surface exchange (e.g. cation rearrangement), this change can be expressed as a shift in the enthalpy of oxidation from -152 kJ/mol (bulk, Chapter 2) to -112 kJ/mol (surface). This energetic surface enhancement could be tied to space charge effects at the semiconductor-gas interface, resulting in a "bending" of the valence band away from the Fermi energy of the p-type conductor, resulting in a more reduced surface, while still retaining the material's nominal A-site composition [81].

4.4 SUMMARY

Linear and nonlinear impedance data were collected between 700-800°C and at 0.01, 0.21, and 1 atm O_2 on symmetric LCF-91|YSZ cells and interpreted using both the 1D and 2D porous electrode models developed for p-type mixed conductors in Chapter 3. Estimates of the capacitive contribution of the bulk electrode, as well as a depressed-Gerischer linear response, imply that the active region of the electrode is limited close to triple phase boundary, increasing the likelihood of multi-dimensional transport effects. Dimensional analysis of the characteristic impedance features suggests moderate surface diffusion with increasing p_{O2}, as well as an equilibrium exchange rate somewhat between that predicted by dissociative adsorption and chemisorption rate laws—though the validity of the latter analysis was shown to be very sensitive to the transient nature of the EIS response.

The observed nonlinear impedance spectra had a much stronger p_{O2}dependence than could be explained by a model considering just bulk diffusion and uniform bulk thermodynamics. Even after allowing for surface diffusion, none of the models could explain the observed trends without assuming the electrode surface to be at a more reduced state than predicted by bulk thermodynamics. Only in the case of a dissociate adsorption rate law, interstitial oxygen surface diffusion, and drastically enhanced surface thermodynamics was qualitative nonlinear agreement reached.

5. Oxygen Reduction on Porous LSCF-6428 Electrodes

5.1 INTRODUCTION

$La_{1-x}Sr_xCo_{1-y}Fe_yO_{3-\delta}$ (LSCF) has gained interest over the last 30 years as an alternative oxygen electrode material for intermediate temperature SOFCs and SOECs. Particularly, the composition $La_{0.6}Sr_{0.4}Co_{0.2}Fe_{0.8}O_{3-\delta}$ (LSCF-6428) exhibits a good balance of kinetic activity, ionic and electronic transport properties, and chemical stability [16], [82], [83]. Because of LSCF's reactivity with the most common electrolyte material, yttria-stabilized zirconia, gadolinium-doped ceria (GDC) electrolytic interlayers are required [84]. Alternatively, for intermediate temperatures (500-800°C), GDC alone behaves as a suitable electrolyte material [85], [86], avoiding the issue of electrode-electrolyte reactivity.

Electrochemical measurements on LSCF-6428, including conductivity relaxation [87], coulometry [88], and impedance techniques [89], all underline the importance of oxygen vacancy reactions and diffusion on overall performance, but a consensus on the exact nature of the rate-determining phenomena has still not been reached. Therefore, this chapter seeks to extend the analysis of oxygen reduction on p-type mixed conducting electrodes developed in Chapters 3 and 4 to LSCF-6428 electrodes.

5.2 EXPERIMENTAL

5.2.1 Symmetric Cell Fabrication

Approximately 2.2 g of $Ce_{0.9}Gd_{0.1}O_2$ (GDC, Praxair, 7.08 m^2/g) was uniaxially pressed in a cylindrical die at 6,000 psi for 3 minutes, then fired at 1500°C for 4 hours, ramping at 2°C/min to produce a dense electrolyte pellet.

$La_{0.6}Sr_{0.4}Co_{0.2}Fe_{0.8}O_{3-\delta}$ powder (Praxair, 6 m^2/g) was micronized for 30 minutes to break up agglomerates before mixing with an organic solution (91.5 wt% α-terpineol, 0.5% oleic acid, 8% ethyl cellulose), producing an ink with 50% solids loading. A three-roll mill with 127 μm spacing was used to ensure an even distribution of solids in the ink. The ink was screen-printed onto both faces of the GDC electrolyte and a reference electrode was hand-painted along the perimeter of the pellet. Figure 4.1 shows the LSCF|GDC cell after sintering at 1050°C in air for 2 hours, ramping at 2°C/min.

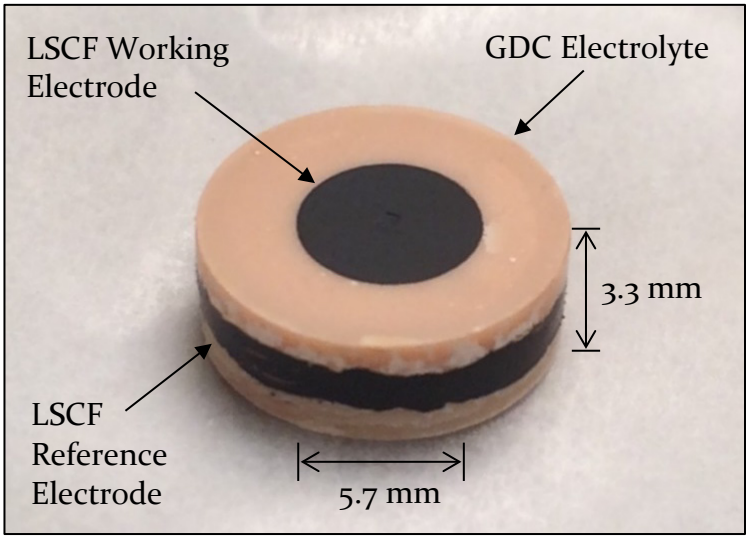

Figure 5.1: A picture of a symmetric cell used in electrochemical testing shows LSCF working (identical counter not shown) and reference electrodes on a GDC pellet.

5.2.2 *Cell Characterization*

The cross section of the LSCF-GDC interface was observed via SEM after fracturing the cell normal to the interface. Figure 4.2 shows a well-adhered electrode of total thickness between 4-6 μm. Good contact between particles with diameters ranging from 0.1 to 1 μm was observed for these sintering conditions.

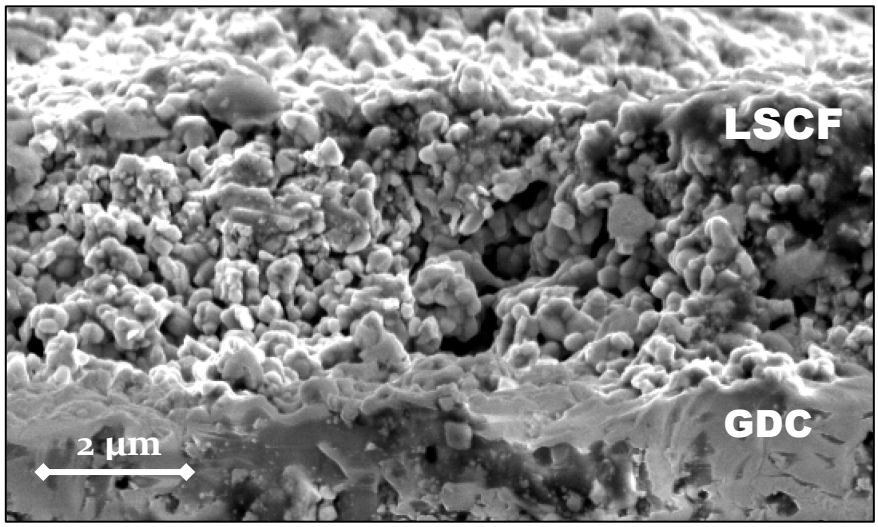

Figure 5.2: SEM of the electrode-electrolyte interface shows a cell thickness between 4-6 μm, good electrode contact to the GDC, and particle diameters ranging from 0.1-1 μm.

5.2.3 *Impedance Measurements*

The testing apparatus for electrochemical measurements was identical to that described in Chapter 4. Nonlinear electrochemical impedance spectroscopy (NLEIS) was performed in 1%, 10%, and 100% oxygen (balance nitrogen) environments at 550, 600, and 650°C. All presented spectra correspond to single-chamber half-cell measurements. The reported EIS spectra were extracted from the linear portion of the NLEIS data and not performed as separate measurements. Galvanostatic zero-bias AC perturbations producing half-cell voltage response amplitudes between 10 mV (most linear) and 160 mV (most nonlinear) and

perturbation frequencies ranging from 100 MHz to 5 mHz were performed once the system was allowed to equilibrate with the new gas and temperature environment for at least 48 hours. All data were collected in the order of 100%-10%-1%-100% 0_2 before increasing the operating temperature. A full amplitude (20) and frequency (10/decade) sweep at a single temperature and p_{O_2} lasted between 6 and 12 hours.

5.3 ELECTROCHEMICAL ANALYSIS: RESULTS & DISCUSSION

5.3.1 Linear Impedance Spectroscopy Results

Figure 5.3 shows the measured EIS spectra of the LSCF|GDC half-cell exposed to 1%, 10%, and 100% O_2 environments at 550, 600, and 650°C. All spectra show two clear features: a small p_{O2}-independent high-frequency feature, likely tied to the LSCF-GDC interface, and a large p_{O2}-dependent chemical feature. This chemical feature closely resembles the Gerischer response predicted in Chapter 3, implying a co-limitation of kinetic and transport phenomena for the oxygen reduction process on LSCF.

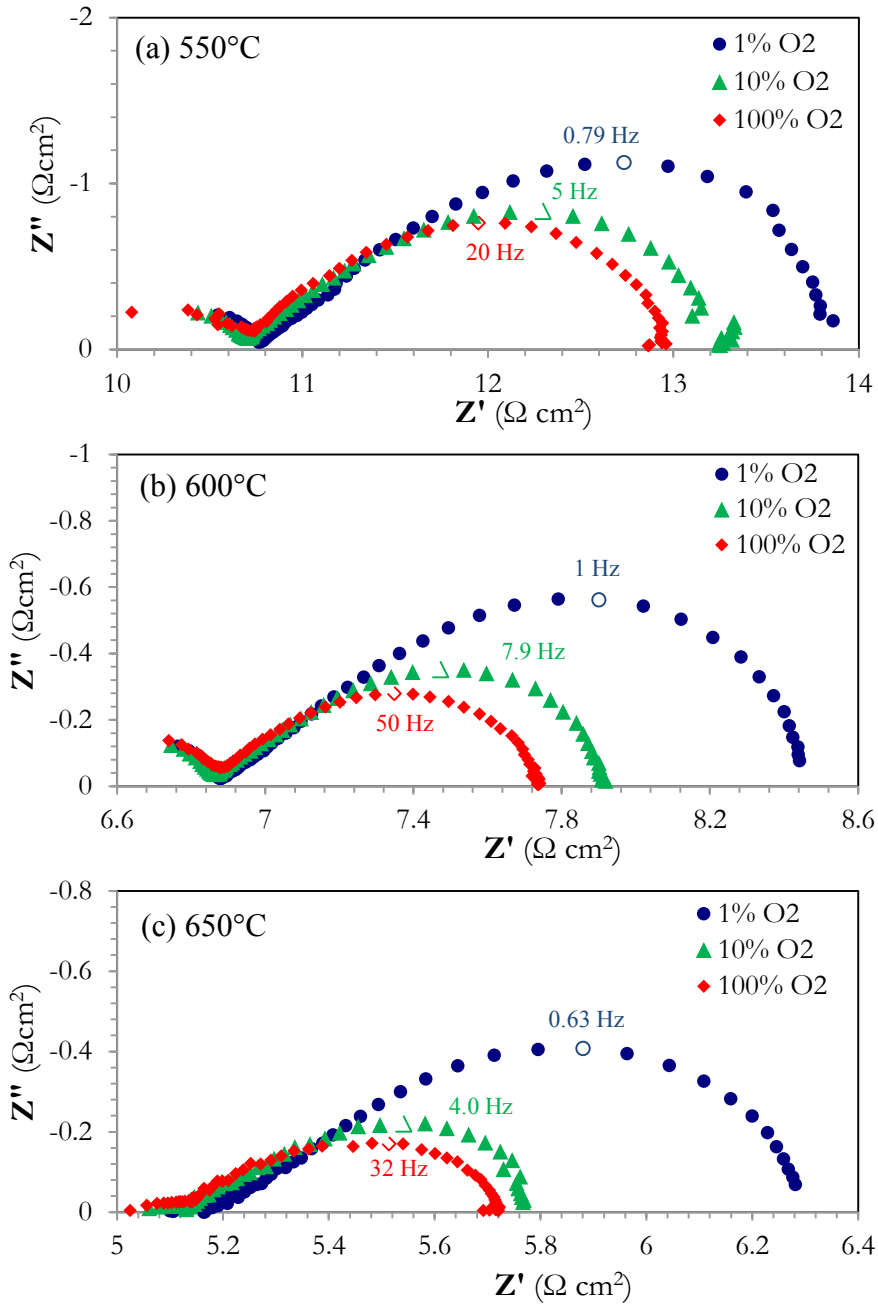

Figure 5.3: The EIS spectra at 0.01, 0. 1, and 0.01 atm O_2 are shown for (a) 550, (b) 600, and (c) 650°C.

Figure 5.4 quantifies the electrode performance using the characteristic resistance R_c ("arc height") and peak frequency ω_c defined in Chapter 3. The observed values are consistent with those measured in the literature [90]. R_c has a

$p_{O2}{}^{n}$ dependence, where $n \approx$ -0.08–-0.19, and thermal activations between -65 and -94 kJ/mol. Figure 5.5a shows a stronger dependence of ω_c on p_{O2}, with values of n = 0.77, 0.83, and 0.88 for 550, 600, and 650°C, respectiviely. Assuming $\omega_c \propto \frac{\mathcal{R}_{0,j}}{x_v^0 A_0}$ for a 1D porous electrode model and the thermodynamic dependence of x_v^0 and A_0 measured by Kuhn *et al.* for LSCF6428, allows the p_{O2} dependence of ω_c to be related to that of the equilibrium exchange rate $\mathcal{R}_{0,j}$ [16]. Figure 5.5b shows that the observed p_{O2} dependence of ω_c is between that predicted by chemisorption ($\mathcal{R}_{0,ca} \propto p_{O2} x_v^0$) and dissociation adsorption ($\mathcal{R}_{0,da} \propto p_{O2} x_v^{0\,2}$) rate laws, though the 550 and 600°C data appear closer to the former. The $p_{O2}{}^{n}$ dependences of R_c and ω_c for the measured LSCF-6482 electrode are consistent with independently measured values of n = -0.17 and -0.67, respectively for $La_{0.6}Sr_{0.4}Co_{0.2}Fe_{0.8}O_{3-\delta}$ [89], suggesting similar rate-limiting phenomena between differing compositions of LSCF.

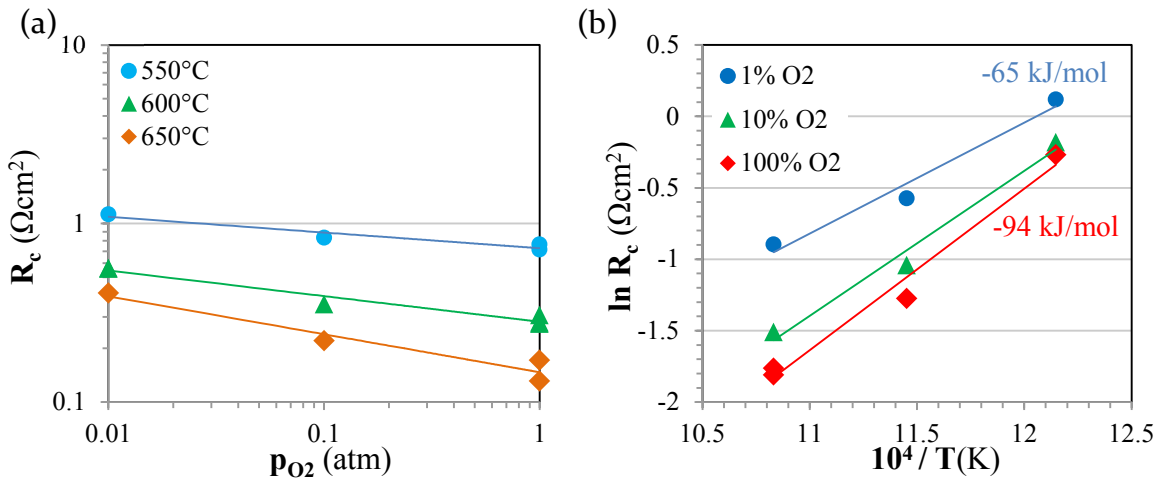

Figure 5.4: Measured values of the characteristic resistance R_c show (a) a weak decrease with increasing p_{O2} and (b) thermal activation of ~ -65–-94 kJ/mol.

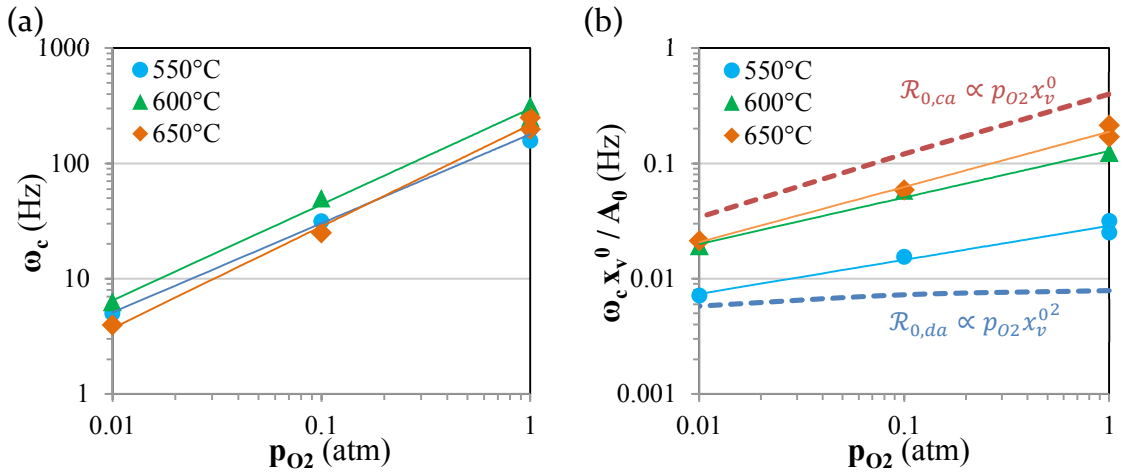

Figure 5.5: (a) The peak frequency ω_c shows a strong p_{O2}^n dependence where $n \approx 0.77 - 0.88$, (b) which is compared to the predicted dependence of equilibrium exchange rates for chemisorption (dashed red line) and dissociative adsorption (dashed blue line) rate laws.

In a manner similar to Chapter 4, the measured area-specific capacitances of the low-frequency features in Figure 5.3 are interpreted as changes in equilibrium bulk nonstoichiometry of the electrodes. Figure 5.6 shows increased capacitances at conditions corresponding to increased vacancy concentration (i.e. low p_{O2} and high temperature). Assuming the equilibrium values given by Kuhn *et al.* and a porosity of $\epsilon \approx 0.5$, Figure 5.6b relates the measured capacitances to an estimated active length of the electrode extending from the electrode-electrolyte interface [78], [91]. L_δ is estimated to be on the order of or larger than the average electrode particle diameter, suggesting that, while two-dimensional effects are expected, a one-dimensional model is likely adequate. This conclusion is further supported by the degree of "flattening" observed in the linear spectra compared to a 1D model: at 650°C and 100% O_2, an underestimation of 23% is observed, while the average error for all other conditions is 5.9%.

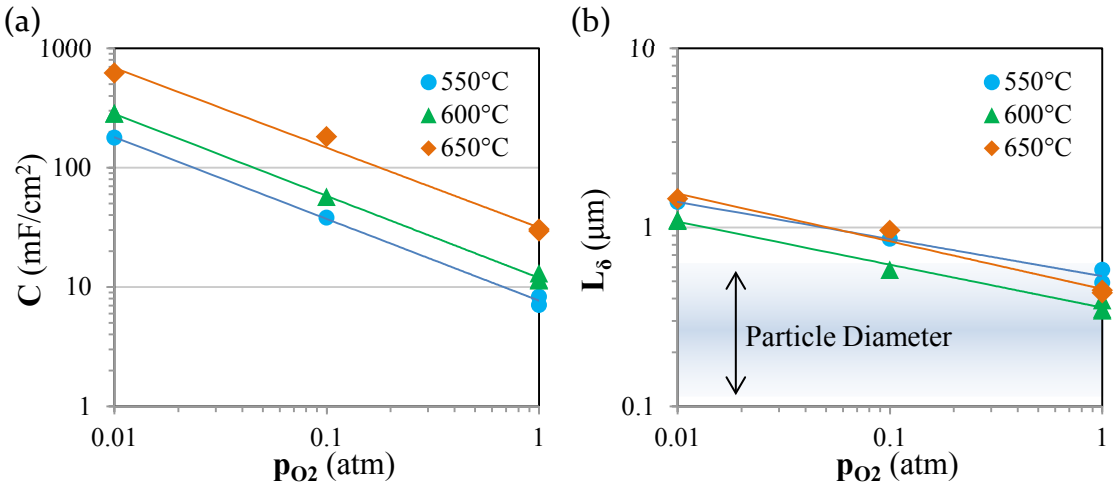

Figure 5.6: By relating (a) the measured chemical capacitance of the elec trode to changes in bulk nonstoichiometry, (b) the length of the active region of the electrode from the triple phase boundary (L_δ) is estimated and compared to observed electrode particle diameters.

5.3.2 *Nonlinear Impedance Spectroscopy Results*

Figure 5.7 shows the nonlinear spectra of LSCF|GDC half cells measured at different temperatures and p_{O2}, the linear portion of which corresponds to the data shown in Figure 5.3. U_{22} and U_{33} represent second and third-order dimensionless Fourier voltage coefficients defined in Ref. [39] and scaled to the linear characteristic resistances and frequencies, R_c and ω_c. Phasor lines intersecting ω_c are drawn to indicate the characteristic time constant of the linear response.

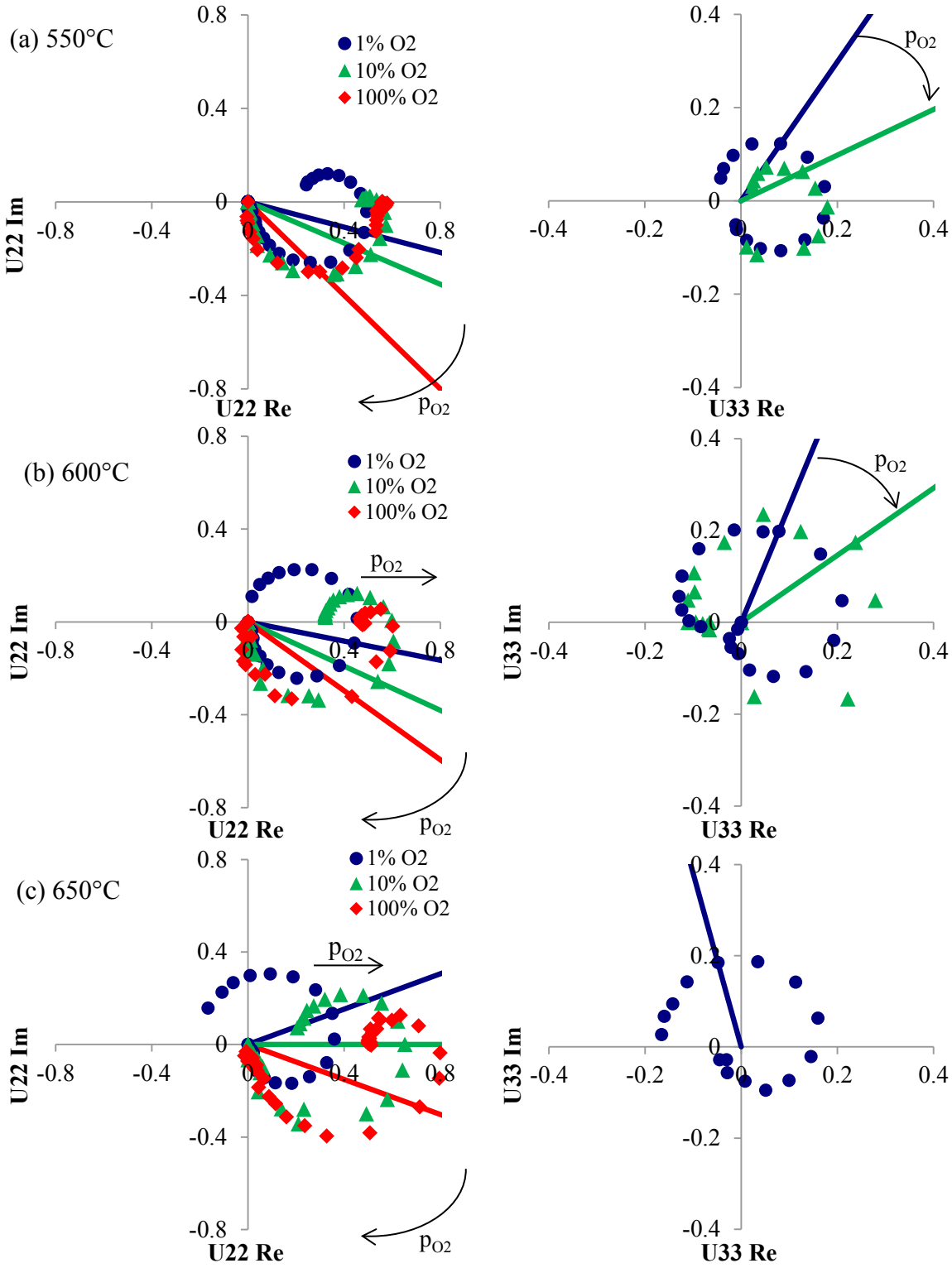

Figure 5.7: The measured second (left) and third-order (right) nonlinear response at p_{O_2} of 0.01 (blue), 0.1 (green), and 1 atm O_2 (red) is shown at (a) 500, (b) 550, and (c) 650°C.

The important trends of rotating phasor lines (representing changes in nonlinear time constant) and shifting excursions (representing the magnitude of the harmonic response relative to the linear signal) are indicated for increasing p_{O2}. The missing U_{33} spectra at high p_{O2} and temperature correspond to data where the third-order voltage harmonic fell below the measured noise floor.

Figure 5.7 shows that at $< 650°$, the magnitude of U_{22} and $U_{33}$are nearly p_{O2} independent. For all temperatures, U_{22} and U_{33} show a strong clockwise phasor rotation with increasing p_{O2}. Qualitatively, these trends differ from those observed for LCF-91 in Chapter 4.

5.3.3 *Comparison to Porous Electrode Models*

The spectra in Figure 5.7 are interpreted by comparing to the various porous electrode modeling scenarios discussed in Chapter 3. Unless otherwise stated, values of A_0, representing the thermodynamic state of the electrode bulk, are fixed to values measured by Kuhn *et al.* and surface oxygen storage is neglected (i.e. $\varphi = 0$) [16].

The simplest one-dimensional model considered bulk diffusion to be the only transport pathway ($\nu = 0$) and the thermodynamics of the surface to be identical to the bulk ($A_{0,s} = A_0$). Figure 5.8 compares U_{22} predicted for these assumptions for both a chemisorption and dissociative adsorption rate law to the measured spectra at 650°C. Both rate laws overestimate the magnitude of U_{22} while failing to capture the observed strong p_{O2} dependence of the nonlinear time constant. This implies that for the considered rate laws, phenomena beyond uniform thermodynamics and bulk-only transport must be considered.

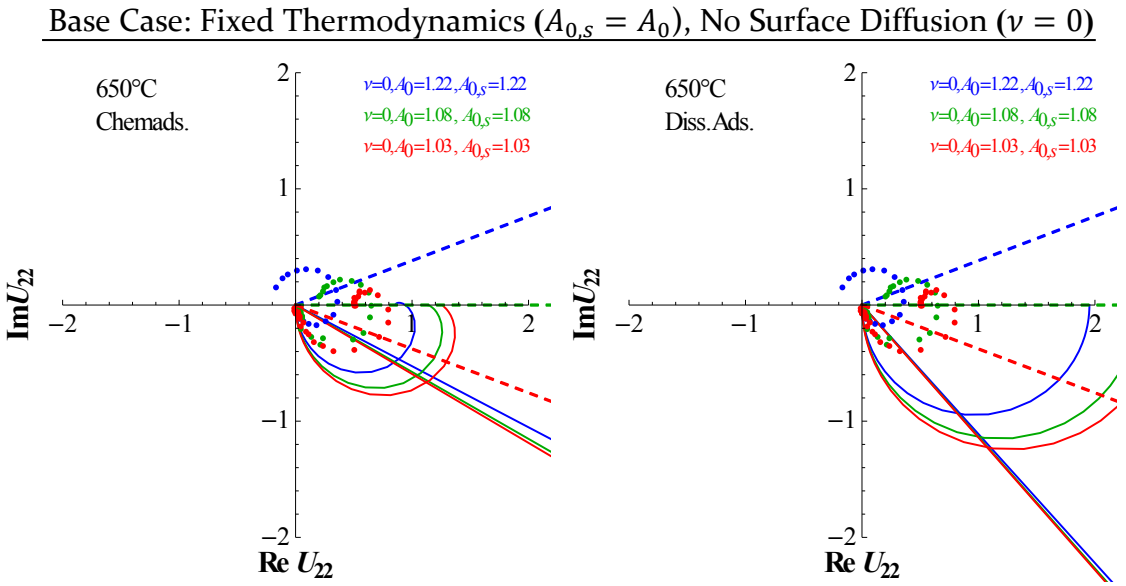

Figure 5.8: The simplest modelling scenario (solid lines) neglecting surface diffusion ($\nu = 0$), fixing the surface thermodynamics to measured bulk values ($A_{0,s} = A_0$) and assuming either a chemisorption (left) or dissociative adsorption (right) rate law is compared to measured U_{22} (dashed lines) at 650°C for 1% (blue), 10% (green), and 100% O_2(red).

The surface diffusion mechanisms assuming either mobile oxygen interstitials or surface vacancies described in Chapter 3 were both considered, yet only the former yielded superior fits. Fixing $\nu = 0$ but allowing $A_{0,s} > 0$ could not simultaneously capture the strong phasor rotation with p_{O2} while still correctly estimating the magnitude.

Therefore, both ν and A_0, s were relaxed as fitting parameters. Figure 5.9 and Figure 5.10 show the results of these fits assuming either a chemisorption or dissociative adsorption rate law, respectively. As shown in Figure 3.9, for specific values of ν and $A_{0,s}$, both rate laws predict a nullification of U_{33}, possibly accounting for the failure to measure a third voltage harmonic at the highest p_{O2}. While both models yield good quantitative agreement with the data if U_{22} is considered independent of U_{33} (not shown), both rate laws have difficulty

predicting the correct ratio of magnitudes between U_{22} and U_{33}, though dissociative adsorption fares better in this regard.

For these fits to be valid, the resulting values of ν and $A_{0,s}$ must be consistent with their physical definitions in Chapter 3: increasing values of $A_{0,s}$ must correspond to more reducing conditions (increasing T, decreasing p_{O2}), and ν, for interstitial oxygen diffusion, must increase with increasing p_{O2}. Figure 5.9 (chemisorption) shows that the values of $A_{0,s}$ are not thermodynamically consistent across all temperatures and p_{O2}, while ν shows no clear trend with p_{O2}. Figure 5.10 (dissociative adsorption), shows qualitatively consistent values of $A_{0,s}$, yet ν appears to *decrease* with increasing p_{O2}. Therefore, the observed nonlinear spectra are inconsistent with the above set of assumptions of enhanced surface nonstoichiometry and surface oxygen diffusion for both rate laws considered.

Alternative Modeling Scenarios

In order to test the sensitivity of the previously discussed models to small changes in bulk nonstoichiometry, A_0 was allowed to deviate from its thermodynamically predicted values. While this scenario yielded good quantitative fits for a dissociative adsorption rate law, the resulting values of A_0 (e.g. 1.53 at 1% O_2 and 650°C compared to 1.22) were outside what could be attributed to errors in thermodynamic measurements of bulk nonstoichiometry.

However, this result suggested that beyond affecting surface kinetics and surface diffusion, enhanced thermodynamics may also result in an increased vacancy capacity in the near-surface bulk (currently assumed to have zero volume). To test this hypothesis, the near-surface bulk was assigned a finite annular volume fraction of the bulk electrode, λ, and included in the materials balance in Chapter 3. By once again fixing A_0 to measured values and varying $A_{0,s}$, ν, and now λ, this model was fit to the observed data. However, the resulting fits failed to improve significantly on those presented in Figure 5.10, and was therefore not considered a valid explanation.

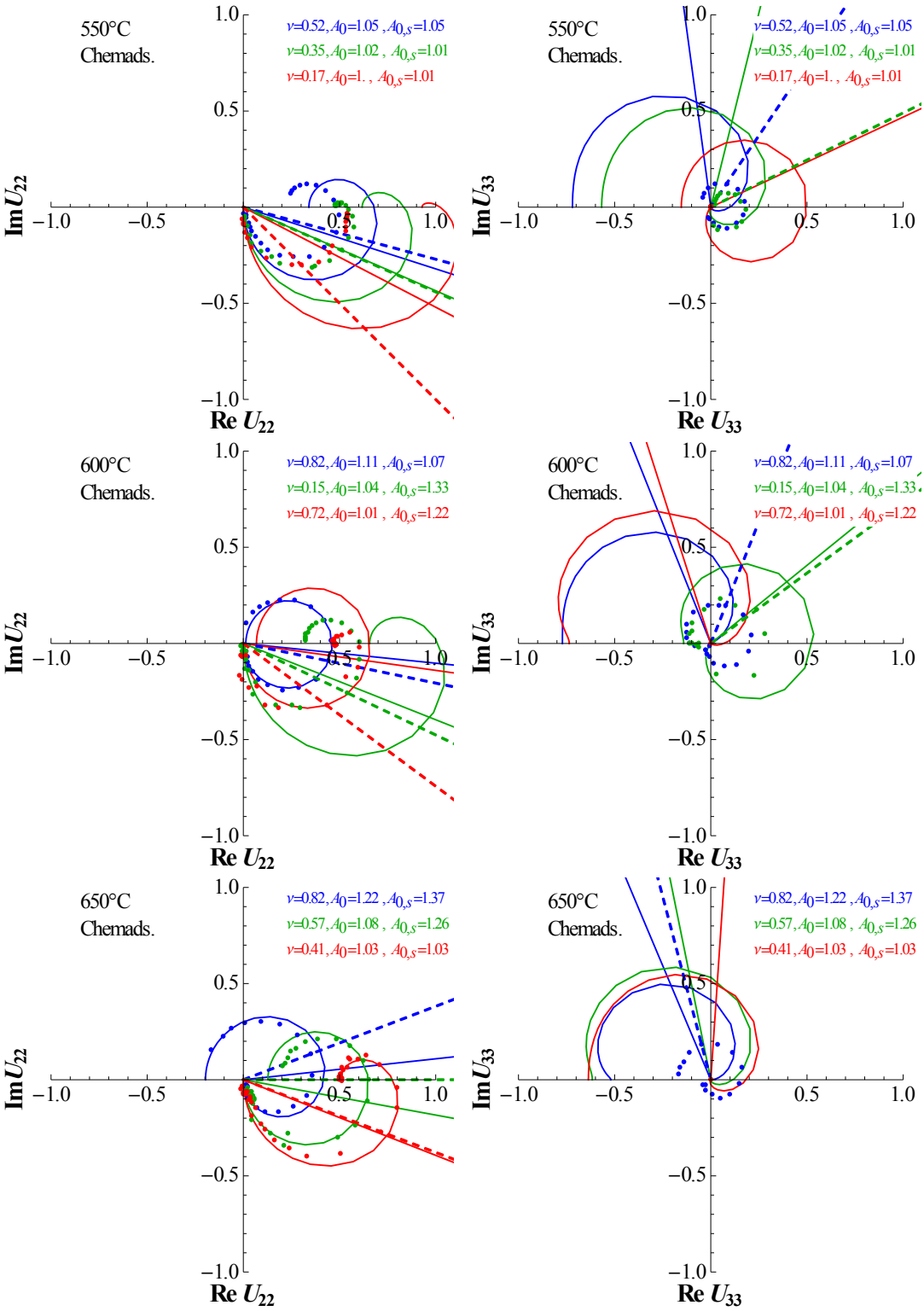

Figure 5.9: U_{22}(left) and U_{33}(right) assuming $\nu > 0$, $A_{0,s} > A_0$, and a chemisorption rate law (model, solid lines) is fit to data (dashed lines) for p_{O2} of 0.01 (blue), 0.10 (green), and 1 atm (red) and 550 (top), 600 (middle), and 650°C (bottom).

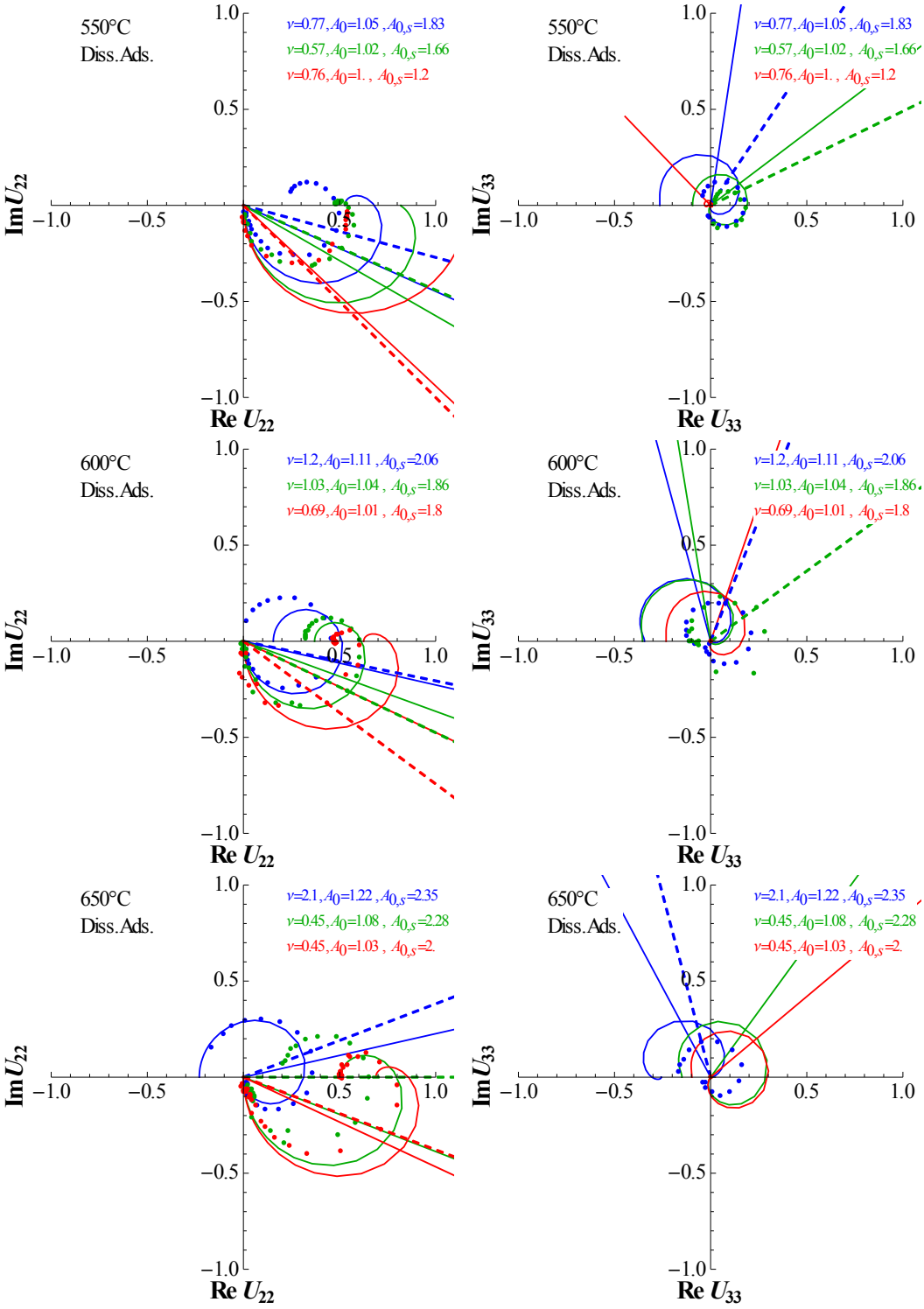

Figure 5.10: U_{22}(left) and U_{33}(right) assuming $\nu > 0$, $A_{0,s} > A_0$, and a dissociative adsorption rate law (model, solid lines) is fit to data (dashed lines) for p_{O2} of 0.01 (blue), 0.10 (green), and 1 atm (red) and 550 (top), 600 (middle), and 650°C (bottom).

5.4 SUMMARY

Linear and nonlinear impedance data were collected between 550-650°C and at 0.01, 0.1, and 1 atm O_2 on a symmetric LSCF-6428|GDC cell and interpreted using both the 1D and 2D porous electrode models developed for p-type mixed conductors in Chapter 3. EIS data suggest that oxygen reduction is co-limited by kinetic and transport phenomena. Furthermore, the shape of the linear spectra and estimates of the active region of the electrode imply that a one-dimensional electrode model is likely adequate. The temperature and p_{O2} dependence of characteristic resistance and frequency are consistent with values in the literature and appear between those predicted by chemisorption and dissociative adsorption rate laws.

The observed nonlinear impedance spectra were found to have a much stronger p_{O2}dependence than explainable by the simplest model considering just bulk diffusion, uniform bulk thermodynamics, and these two rate laws. Even in models allowing for surface diffusion and enhanced surface thermodynamics, neither rate law was found to be consistent with the observed trends, suggesting either additional physics or modified assumptions need to be considered. However, because of the weak p_{O2} dependence of LSCF's bulk reducibility relative to that measured by NLEIS, any rate law is unlikely to be consistent *without* additionally considering strongly p_{O2} -dependent phenomena, such as increased surface reducibility or surface diffusion.

6. Porous LCF-91 Electrodes in H_2-H_2O Environments

6.1 INTRODUCTION

One of the main motivations for studying the thermodynamics of LCF under reducing conditions in Chapter 2 was the electrode's potential application as an SOFC or SOEC fuel electrode. As discussed in Chapter 1, an advantage of n-type mixed-conducting perovskites over the state-of-the-art H_2 electrode, Ni-YSZ, is their stability in carbon-containing environments. Before extending analysis to co-electrolysis of H_2-H_2O-CO-CO_2 systems, understanding of the electrode behavior in H_2-H_2O environments is essential.

LCF-91 was selected as a model electrode for studying the rate-determining phenomena relevant to water reduction on n-type perovskite mixed conductors. The work in this chapter aims to highlight difficulties for electrochemical analysis of this class of materials unique to reducing conditions which must be addressed before undertaking the kind of analysis presented in Chapter 4. Particular emphasis is given to the role of the current collector in impedance measurements—a factor typically neglected for similar materials in oxygen environments—as well as the transient behavior of interfacial processes greatly affecting cell performance.

6.2 THEORY

The following sections consider the roles of the thermodynamic, kinetic, and transport phenomena of an n-type mixed-conducting electrode in a H_2-H_2O environment near its p-n transition. These results build on the 1D macrohomogeneous model presented in Chapter 3 for oxygen reduction of p-type mixed conductors.

6.2.1 Thermodynamics

The thermodynamic behavior of LCF-91 under the reducing conditions of interest to this chapter is assumed to obey the point-defect model presented in Chapter 2. The overall half-cell reaction is given below in Kröger-Vink notation.

$$H_2O\ (g) + V_O^{\cdot\cdot} + 2e' \rightleftharpoons H_2(g) + O_O^x \tag{6.1}$$

Due to Fe^{2+} being the dominant electronic charge carrier under reducing conditions, the reaction is expressed in terms of electrons instead of holes. In the case of negligible hole concentration, electroneutrality implies $x_e = [Fe'_{Fe}] \approx (6x_v - x)$, where x_e is the mole fraction of electrons per unit cell, x_v the mole fraction of vacancies per oxygen sites, and x is the intrinsic A-site dopant mole fraction.

The Nernst potential of this half-cell relative to an oxygen reference electrode is given below,

$$V = E^0_{cell}(T) + \frac{RT}{2F}\ln\left(\frac{p_{H2O}}{p_{H2}\,p^{1/2}_{O2,ref}}\right) = \frac{RT}{4F}\ln\left(\frac{p_{O2,eff}}{p_{O2,ref}}\right), \tag{6.2}$$

where E^0_{cell} is the standard half-cell potential for Eq.6.1. The right-hand side of Eq. 6.2 also defines $p_{O2,eff}$, the effective p_{O_2} that would be in equilibrium with the given blend of H_2 and H_2O. This allows the thermodynamic factors A and A_0 and equilibrium vacancy mole fraction, x_v^0, to be defined in a manner analogous to that of Chapter 3.

$$A(x_v) \equiv -\frac{1}{2}\frac{\partial \ln\left(p_{\mathrm{O2,eff}}^{\mathrm{solid}}\right)}{\partial \ln(x_v)} = 1 + \frac{12x_v}{6x_v - x} \quad 6.3$$

$$A_0(x_v^0) = 1 + \frac{12x_v^0}{6x_v^0 - x} \quad 6.4$$

The thermodynamic state of a material in H_2-H_2O environments is fully specified by the ratio of p_{H2}:p_{H2O} and temperature. For example, both a 0.1-0.1 atm blend of H_2-H_2O and a 0.2-0.2 atm blend will be at identical $p_{O2,eff}$ (and therefore, A_0) though their associated kinetics might vary. This provides an additional experimental degree of freedom, making measurement of the full range of values for all experimental conditions (temperature, p_{H2}, and p_{H2}/p_{H2O}) time-intensive. In order to limit the range of experimental conditions, Figure 6.1 maps the thermodynamic state (T, $p_{O2,eff}$) of different gas blends of H_2:H_2O and compares it to equilibrium values of LCF-91 oxygen nonstoichiometry, δ. A value of δ = 0.05 corresponds to the observed nonstoichiometry "plateau" discussed in Chapter 2 and is interpreted as the point of minimum electronic carrier concentration. A value of δ = 0.06 corresponds to the most reducing conditions studied in Chapter 2 for this material, where no secondary phase formation has been observed. Therefore, δ = 0.06 and δ = 0.05 serve as upper and lower bounds for studying LCF-91 in reducing conditions. Figure 6.1 shows that at 700-800°C, a gas blend of $0.1 < p_{H2}/p_{H2O} < 10$ falls between these bounds for oxygen nonstoichiometry.

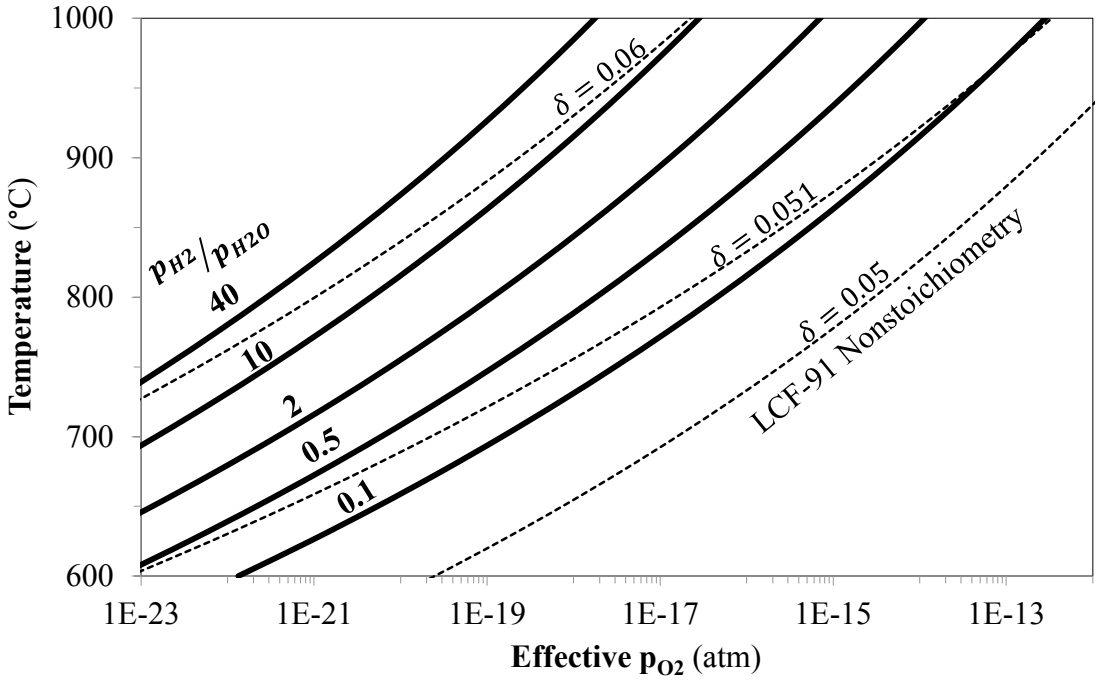

Figure 6.1: The thermodynamic state (T, $p_{O2,eff}$) of various H_2-H_2O blends (solid lines) is compared to that of LCF-91 at values of constant nonstoichiometry (dashed lines).

6.2.2 H_2-H_2O Kinetics

While the overall half-cell reaction for water reduction (or hydrogen oxidation) on a mixed-conducting electrode, given by Eq. 6.1, is well-known, there is no accepted mechanism or rate-determining step. The same approach developed to study oxygen reduction on LCF can be adapted to study water reduction—first proposing a mechanism and rate-limiting elementary step, before deriving a nonlinear, thermodynamically-consistent, mass-action rate law—however, several modifying assumptions are required.

As in the previous chapter, moderately dilute solution theory is invoked. The addition of a second gas-phase species greatly increases the number of likely surface species. Even on the well-studied Ni-YSZ electrode, the choice of active

surface species is not agreed upon [42]. While surface vacancies (s) and oxygen ($s\text{-}O^{2-}$) will remain prevalent, at the higher vacancy concentrations at the low p_{O_2} of interest, using a solvent approximation for $s\text{-}O^{2-}$ to neglect its concentration dependence may no longer be valid. Additionally, as is common in the Ni-YSZ literature, competitive adsorption may be required in the case of high surface coverage [92].

Regardless of the rate-determining step or mechanism, the rate law can be expressed as an effective oxygen rate, resulting in the same form used to study oxygen.

$$r_{O_2,j} = \mathcal{R}^0_{\mathrm{O2,j}}\, \mathrm{R}_{O_2,j}(\chi; A_0, \kappa_{H2}) \tag{6.5}$$

In addition to being parametric in the thermodynamic state of the electrode (A_0), dictated by the ratio p_{H2}/p_{H20}, the dimensionless rate, $\mathrm{R}_{O_2}(\chi)$ is parametric in κ_{H2}, representative of the absolute pressure of H_2. The linear rate law will therefore have the form $r_{O_2,j} = 2A_0\mathcal{R}^0_{\mathrm{O2,j}}\,\chi$.

6.2.3 Transport Properties near the p-n Transition

A common assumption when studying mixed ionic and electronic conductors is that the material's electronic conductivity greatly overshadows its ionic conductivity. One can then neglect gradients in the electrochemical potential of electrons, μ_e, such as in Chapter 3. While this assumption of an electronic transference number, t_e, approaching unity is typically valid for semiconducting materials far from their p-n transition—such as the case of LCF and LSCF in oxidizing conditions—its validity is less certain near the point of minimum electronic carrier concentration.

In order to assess the importance of electronic transport effects, a linear 1D macrohomogeneous model involving bulk vacancy diffusion and a first-order reaction rate was developed in a manner similar to Chapter 3, with the addition of a non-uniform μ_e distribution. The superficial vacancy flux, N_v, now explicitly includes a dependence on the electrical state variable, μ_e,

$$N_v = -c_0 D_v A(x_v) \nabla x_v + \frac{2 c_0 D_v x_v}{\mathrm{RT}} \nabla \mu_e \,, \tag{6.6}$$

where the remaining variables are defined in Chapter 3. Additionally, the total superficial current further relates x_v and μ_e.

$$i = \frac{\sigma_t}{F} \nabla \mu_e - 2 F D_v c_0 A(x_v) \nabla x_v \tag{6.7}$$

In the case of one-dimensional transport normal to the electrode-electrolyte interface, and assuming the definitions in Table 6.1, the linearized dimensionless vacancy material balance and $\nabla \cdot i = 0$ result in the coupled PDE and ODE below.

$$0 = -\frac{\partial \chi}{\partial \tau} + A_0 \frac{\partial^2 \chi}{\partial \xi^2} - 2 \frac{\partial^2 \zeta}{\partial \xi^2} - \kappa A_0 \chi \tag{6.8}$$

$$0 = \frac{\partial^2 \zeta}{\partial \xi^2} - \frac{t_v}{2} A_0 \frac{\partial^2 \chi}{\partial \xi^2} \tag{6.9}$$

The three model parameters are A_0, defining the thermodynamic state, $t_v = 1 - t_e$, the vacancy transference number, and κ, the reaction rate relative to vacancy transport. Assuming a current-controlled half-cell impedance experiment (as in Chapter 3), purely electronic current at the current collector ($\xi = 1$), purely ionic current at the electrolyte ($\xi = 0$), and setting the electrical state of the reference electrode, $\zeta^{RE} = 0$, the four boundary conditions and voltage expression are given below.

$$-\frac{t_v}{2} A_0 \frac{\partial \chi}{\partial \xi}|_{\xi=0} + t_v \frac{\partial \zeta}{\partial \xi}|_{\xi=0} - \alpha \cos(\sigma\tau) = 0 \tag{6.10}$$

$$(1 - t_v) \frac{\partial \zeta}{\partial \xi}|_{\xi=1} - \alpha \cos(\sigma\tau) = 0 \tag{6.11}$$

$$A_0 \frac{\partial \chi}{\partial \xi}|_{\xi=1} + 2 \frac{\partial \zeta}{\partial \xi}|_{\xi=1} = 0 \tag{6.12}$$

$$\zeta_e|_{\xi=0} + \frac{1}{2} \ln\left[(1+\chi)(1+\frac{A_0 - 1}{2}\chi)^2\right]|_{\xi=0} = 0 \tag{6.13}$$

$$U = \zeta_e|_{\xi=1} \tag{6.14}$$

Quantity	Dimensional Form	Dimensionless Form	Dimensional Group
Axial Position	y	$\xi = \frac{y}{y^*}$	$y^* = \mathrm{L}$ (electrode thickness)
Time	t	$\tau = \frac{t}{t^*}$	$t^* = \frac{L^2}{D_v}$
Bulk Vacancy Mole Fraction	x_v	$\chi = \frac{x_v - x_v^0}{x_v^0}$	x_v^0
Electrical State	ζ	$\zeta = \frac{\mu_e}{\mathrm{RT}}$	R T
Voltage	V	$U = \frac{V}{V^*}$	$V^* = \frac{RT}{2F}$
Current Amplitude	$\tilde{\imath}$	$\alpha = \frac{\tilde{\imath}}{i^*}$	$i^* = \frac{\sigma_T RT}{F\ L}$
Frequency	$\widetilde{\omega}$	$\sigma = \widetilde{\omega}\ t^*$	$t^* = \frac{L^2}{D_v}$
Eqm Vacancy Transference #	t_v	$\frac{\sigma_v}{\sigma_T}$	$\sigma_v = \frac{4F^2 D_v c_0 x_v^0}{\mathrm{RT}}$ $\sigma_T = \frac{4F^2 D_v c_0 x_v^0 + F^2 D_e \frac{c_0}{3} x_e^0}{\mathrm{RT}}$
Vac. Diff.-scaled Reaction Rate	$\mathcal{R}_{O_2}^0$	$\kappa = \frac{4aL^2 \mathcal{R}_{O_2}^0}{c_0 x_v^0 D_v}$	$\frac{c_0 x_v^0 D_v}{4aL^2}$

Table 6.1:Definitions of the dimensionless variables and parameters used in the 1D macrohomogeneous model.

Figure 6.2 shows the resulting linear scaled voltage response, U_{11}, upon solving Eqns. 6.10-6.14 for different values of t_v and κ. As $t_v \to 0$, the model approaches that of Chapter 3 where $\nabla\mu_e \approx 0$. In this limit and without any surface reaction (i.e. $\kappa = 0$), a purely real, ohmic response—dictated entirely by the total electronic conductivity (which the response is scaled to, hence $U_{11}(\sigma \to \infty) = 1$)—is predicted. Increasing t_v, even in the absence of any surface reaction, produces an impedance feature with increasing magnitude. At high frequencies, the model describes Hebb-Wagner polarization, where concentration gradients are negligible and the current consists predominantly of migrational fluxes driven by gradients in the electrostatic potential [93], [94]. Upon decreasing frequency, the species distribution in the electrode approaches its steady state concentration profile,

where the migration and diffusion terms of the vacancy flux in Eq. 6.6 negate each other.

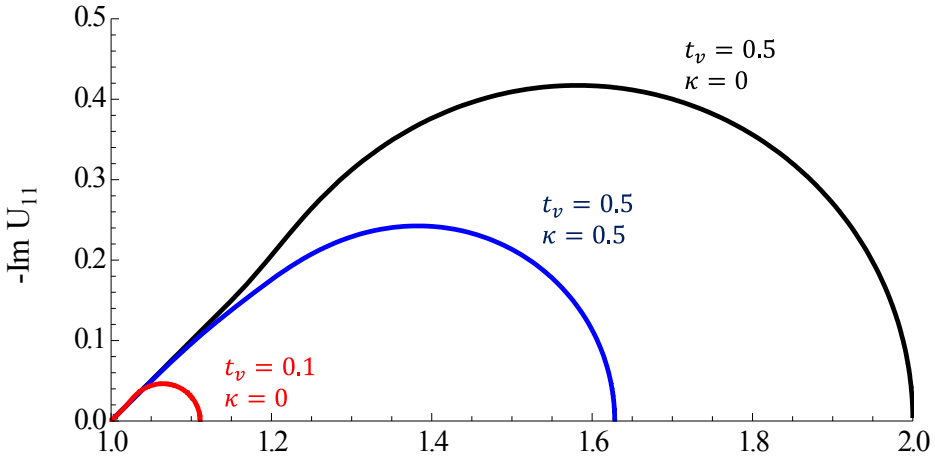

Figure 6.2: The predicted scaled linear voltage response, U_{11}, is given for $A_0 = 1.01$ and varying values of t_v (vacancy transference number) and κ (scaled surface reaction rate).

Introducing a finite surface reaction rate ($\kappa > 0$) causes the impedance feature to approach the Gerischer shape modeled in the previous chapters. The curve in Figure 6.2 corresponding to $t_v = 0.5$ and $\kappa = 0.5$ shows that in the case of significant electronic transport effects, the *shape* of the impedance response is indistinguishable from that predicted by a model assuming $t_v = 0$; only the magnitude of the response is greatly affected.

Ideally, transport properties such as t_v can be independently measured as a function of p_{O2} and temperature to assess the importance of electron transport limitations. Unfortunately, transport data for LCF near its p-n transition does not exist. As a first approximation though, mobilities for LSF-91 can be coupled with the defect model in Chapter 2, to estimate the partial conductivities for LCF-91. Assuming p_{O2}-independent mobilities, u_e, and u_h, of 0.08 and 0.1 $\frac{cm^2}{V\,s}$, and

$D_v = 10^{-5.9}\frac{cm^2}{s}$ at 750°C, where $\sigma_i = \frac{|z_i|F}{V_m}x_i u_i = \frac{z_i^2 F^2 D_i}{V_m}x_i$ for species i, charge number z_i, and molar cell volume V_m, yields the results shown in Figure 6.3a [12], [29], [30]. As required by the thermodynamic model, the point of minimum total conductivity occurs at the center of the p-n transition, approximately 10^{-16}atm O_2 at 750°C. Even at this point, Figure 6.3b shows that the electronic transference number is estimated to reach a minimum of only 0.96.

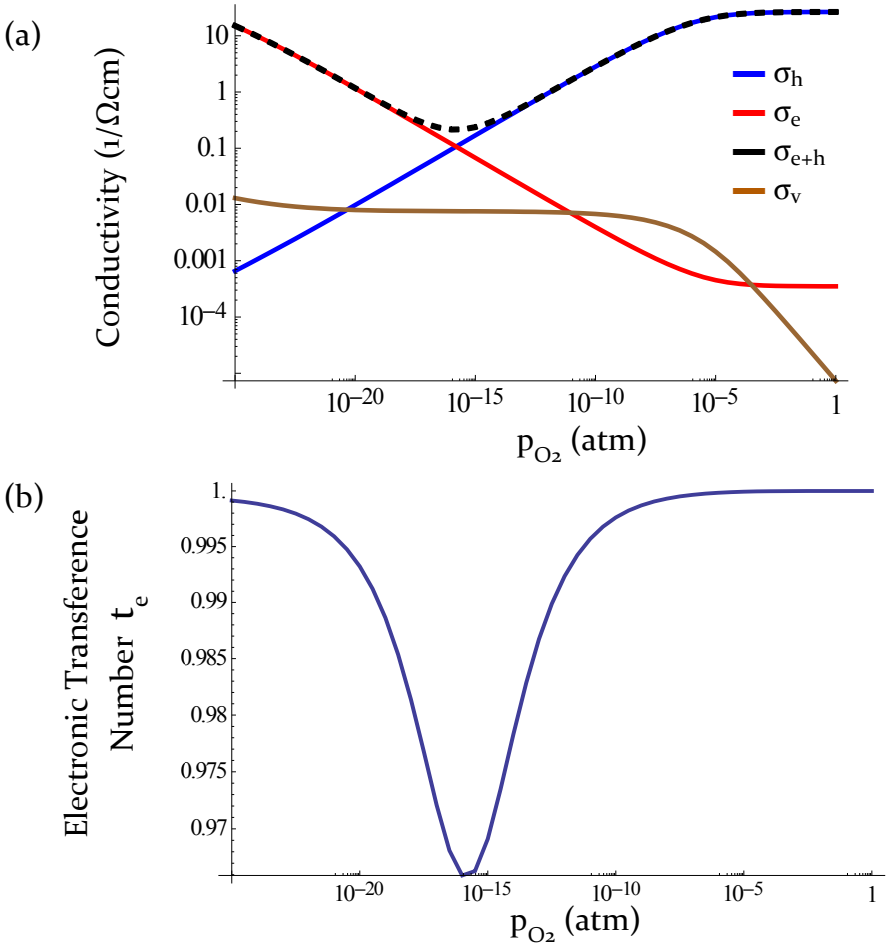

Figure 6.3: Predicted transport properties of LCF-91 based on measured values for LSF-91 [12], [29].

6.3 EXPERIMENTAL

6.3.1 Cell Fabrication & Characterization

In order to test the stability and reactivity of the LCF-YSZ interface under reducing conditions, powders of 50-50 wt% LCF-91 and 8%-YSZ were mixed and pressed at 10,000 psi into pellets. These unsintered pellets were exposed to a 10:1 H_2:H_2O mixture at 850°C for 87 hours before cooling in the reducing environment. Powder x-ray diffraction was performed using a Bruker AXS D8 Discoverer spectrometer with CuK_α radiation at an average wavelength of 1.54 Å.

Symmetric LCF-91|8%-YSZ button cells for 3-electrode electrochemical testing were prepared in a manner identical to that of Chapter 4. Additionally, a dense pellet of LCF-91 (without YSZ) was pressed at 10,000 psi and fired at 1050°C, resulting in a thickness of 3 mm and diameter of 10 mm.

6.3.2 Electrochemical Measurements

The experimental method for linear and nonlinear electrochemical impedance spectroscopy is the same as that for oxygen analysis discussed in Chapter 3. EIS measurements were performed either in a two-electrode "full-cell" arrangement or a three-electrode "half-cell" arrangement with an LCF reference electrode painted around the perimeter of the electrolyte; all NLEIS measurements were performed in a half-cell configuration.

Two kinds of gold current collectors were used. Unless specified otherwise, a gold mesh with a 0.3 mm pitch and 0.1 mm diameter wires was held to the working and counter electrodes using an alumina clamp. Additionally, some cells had a thin layer of gold paste (70 wt%, Fuel Cell Materials, AU-1) painted over the working and counter electrodes before slowly (1°C/min) ramping to the operating temperature in the testing apparatus.

Figure 6.4 shows the configuration for electrochemical measurements. H_2-N_2 gas blends (5%, 10%, 100% H_2) were mixed with a humidified nitrogen stream using a

humidifier consisting of a column of distilled water held at 21°C by an isolated circulating water bath. The final gas blend was fed to the sealed electrochemical testing system before entering a Pt|YSZ oxygen sensor at 750°C. This downstream analysis resulted in Nernst potentials within 1% of the expected values, confirming the nominal gas composition. All data in this study were collected at 750°C with total gas flow rates varying between 20 and 100 sccm.

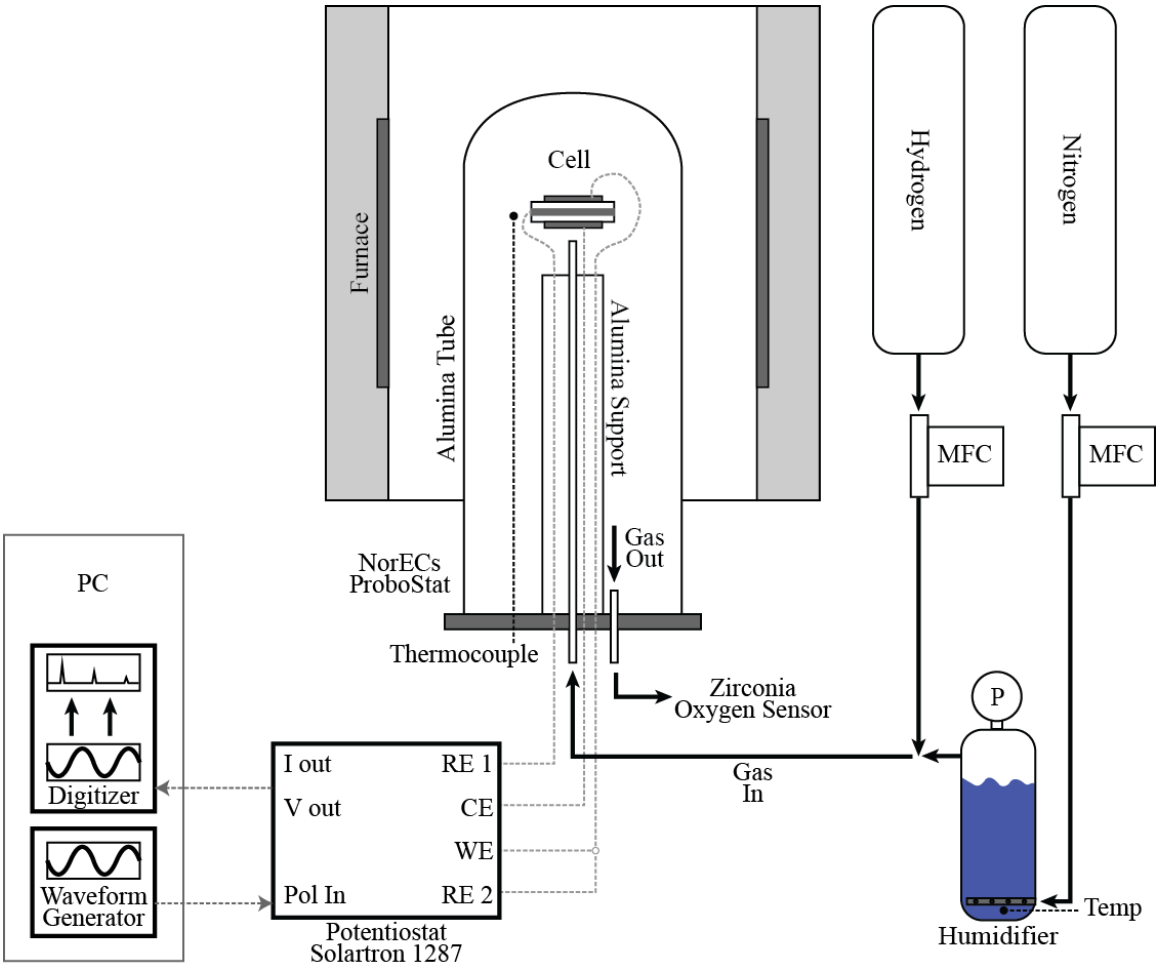

Figure 6.4: The NLEIS setup used for H_2-H_2O analysis is identical to that used for O_2 studies, with the addition of a temperature-controlled humidifier and gas blending system.

6.4 RESULTS

6.4.1 Characterization and Stability

Figure 6.5 shows an SEM of the electrode-electrolyte interface of an LCF-YSZ cell used in electrochemical testing after being cut in half normal to the interface. The electrode thickness was 7-8 μm across the superficial 0.17 cm^2 area, with particle diameters ranging from 0.2-1.2 μm.

Figure 6.6 shows the x-ray diffraction spectrum of the 50-50 wt% LCF-YSZ pellet exposed to a 10:1 H_2-H_2O gas blend at 850°C for 87 hours. Matching catalogued spectra for $LaFeO_3$ and YSZ to the measured peaks shows that all features can be accounted for by either the electrode or electrolyte. The only peak not accounted for was attributed to unreacted ZrO_2 from the YSZ powder—confirmed from independent XRD experiments.

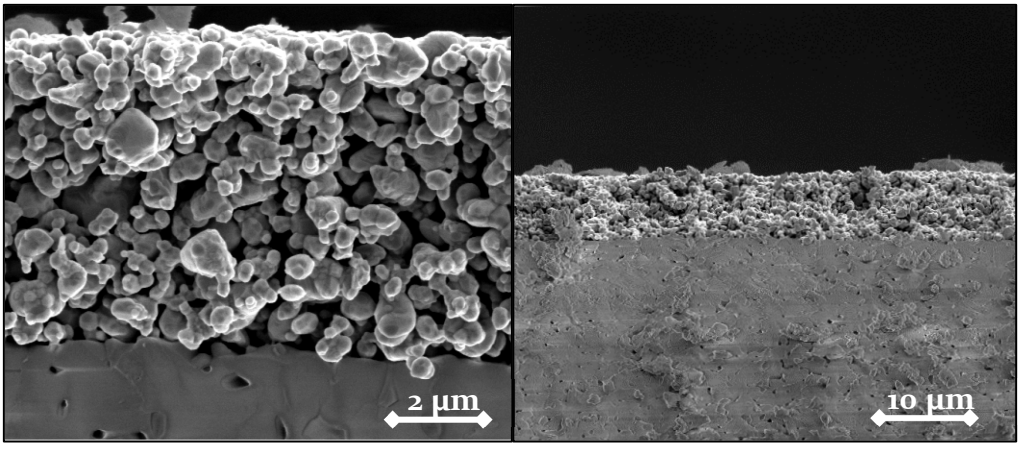

Figure 6.5: Cross-sectional SEM of the LCF-YSZ electrode-electrolyte interface.

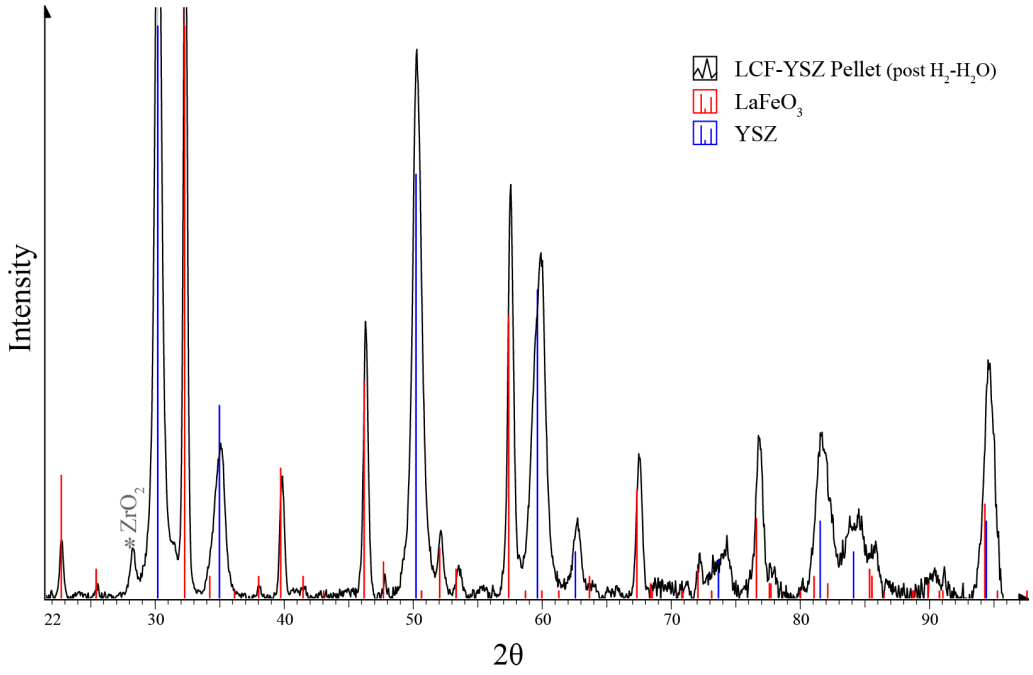

Figure 6.6: XRD of a 50-50 wt% LCF-YSZ pellet exposed to a 10:1 H_2-H_2O blend at 850°C for 87 hours.

6.4.2 Electrochemical Measurements in H_2-H_2O

Linear Impedance Spectroscopy

Figure 6.7 shows the half-cell measurement of the linear impedance data for a LCF-91|YSZ symmetric cell exposed to a 2.8% H_2 and 1.4% H_2O blend at 750°C as a function of time, over the course of eight days, where $t = 0$ corresponds to the time of initial exposure to reducing conditions. The linear impedance results in this section have been extracted from NLEIS data.

At least three unique features are observed in the spectra, with their peak frequencies ($f_p = \omega_c/2\pi$) labeled. The highest frequency process (Z_3) occurs at a timescale similar to the process observed in an oxygen environment, which was assumed to correspond to an electrode-electrolyte interfacial resistance; however, its magnitude is significantly larger and continues to increase with time. The lowest frequency process (Z_1) shows a relatively constant peak frequency,

occurring at timescales similar to those observed for the dominant chemical process in an oxygen environment. The intermediate frequency process (Z_2) shows a strong frequency dependence over time. The varying degree of overlap between the three processes hinders the separation of their contributions to the total impedance ($Z_T = Z_1 + Z_2 + Z_3$).

Figure 6.8 tracks three characteristic parameters for each electrode feature over time: the imaginary "arc height", R_c, the peak frequency, ω_c, and the capacitance, C. The majority of the total half-cell's increase in resistance comes from the highest frequency feature, evidenced by $R_{c,1}$. The characteristic resistances of the two lower frequency features, particularly $R_{c,3}$, are much more stable. The peak frequency of the intermediate frequency process, ω_2, exhibits the sharpest decrease, causing it to further obfuscate the low frequency process with time. Expressing R_c and ω_c as capacitances shows that the lowest frequency process has a value consistent with a chemical process occurring in the bulk electrode, while the intermediate-frequency capacitance of $\sim 10\ \mu F/cm^2$ is on the order observed for double-layer capacitances for the electrode-electrolyte interface [11].

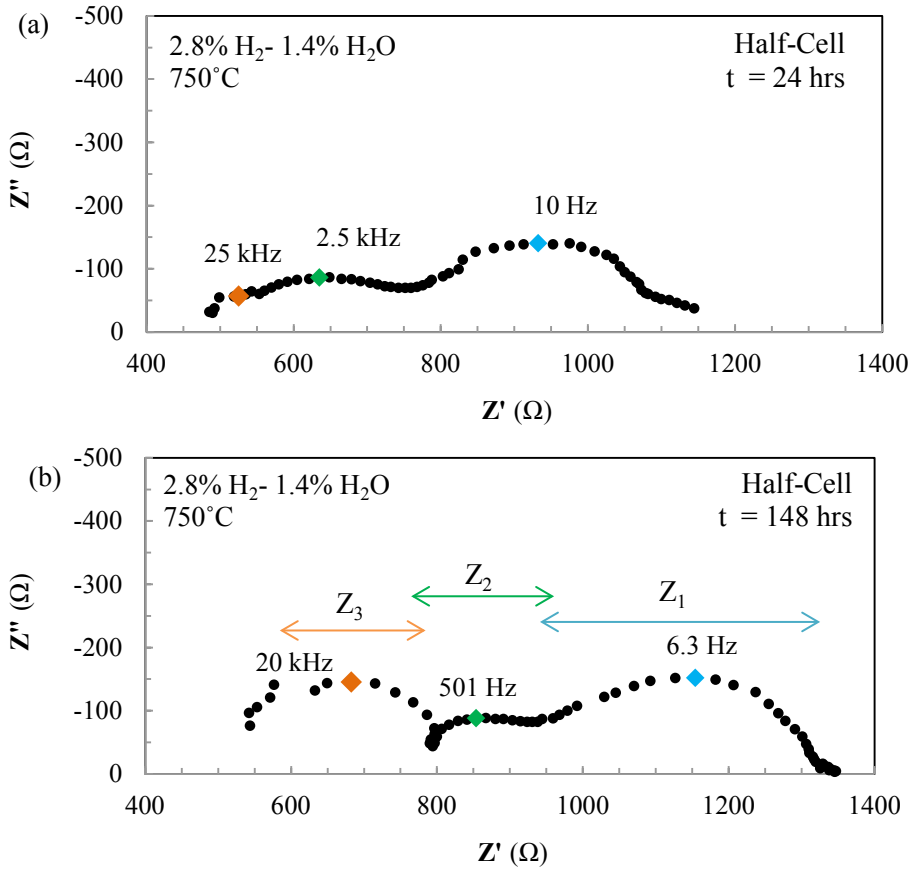

Figure 6.7: The linear impedance data measured in a 2.8% H_2 and 1.4% H_2O blend at 750°C shows a strong time variance in two high-frequency features over 8 days.

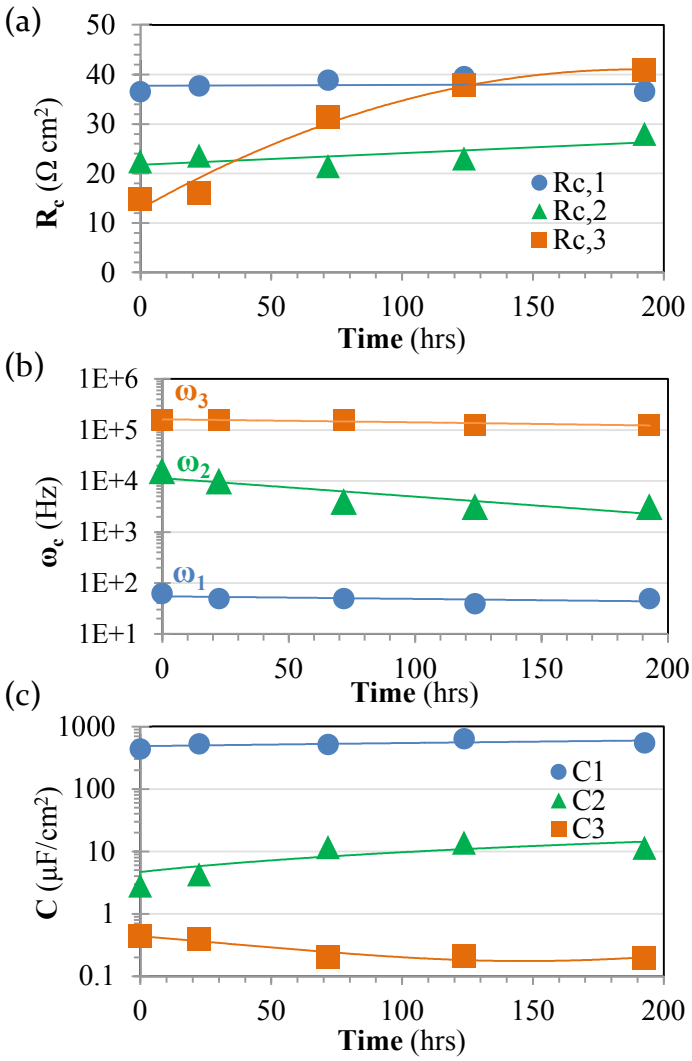

Figure 6.8: The characteristic (a) resistance, (b) frequency, and (c) capacitance for the half-cell shown in Figure 6.7 are tracked over 200 hours of exposure to a 2.8% H_2 and 1.4% H_2O gas blend at 750°C.

Nonlinear Impedance Spectroscopy

NLEIS was performed on the same cell under the conditions described in the previous section as a function of time. Figure 6.9 shows the dimensionless second and third-order nonlinear response of the cell after 193 hours of H_2-H_2O exposure, where U_{22} and U_{33} have been normalized to the total, series-resistance-subtracted linear impedance. In order to compare the timescales of the nonlinear response to those shown Figure 6.7, phasor lines are drawn intersecting ω_1 and the labeled

frequencies near the origin indicate the highest frequency capable of producing a measurable nonlinear response. Comparing these frequencies to those in Figure 6.8b suggests that highest frequency process is purely linear. While the intermediate process is slightly nonlinear, the majority of NLEIS response occurs at frequencies attributable to the low-frequency linear process, Z_1.

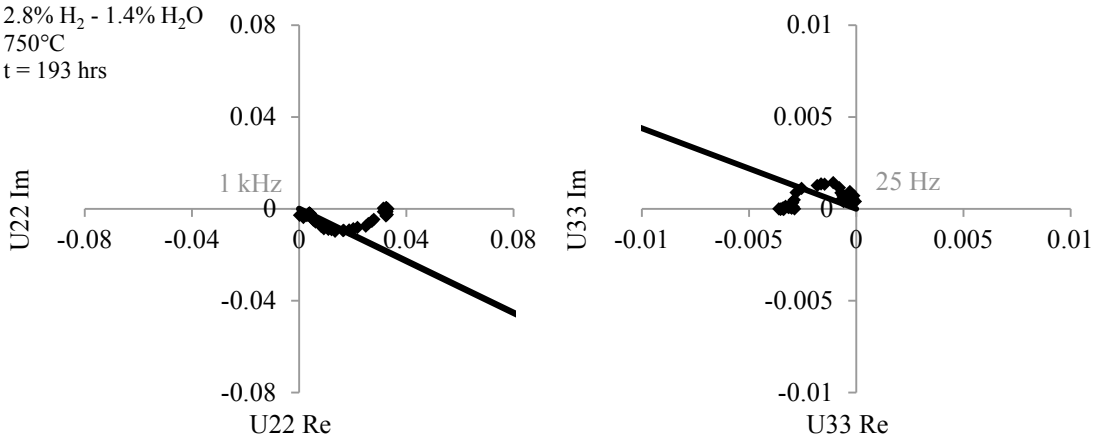

Figure 6.9: The second and third harmonic NLEIS spectra are shown for a 2.8% H_2 - 1.4% H_2O blend at 750°C after 193 hours of exposure. Phasor lines indicate the peak frequency of the low-frequency feature (ω_1), and labeled frequencies near the origin indicate the highest frequency resulting in a measurable nonlinear response.

Returning to Oxidizing Environments

In order to assess the reversibility of the processes affecting performance in reducing conditions, the same button cell discussed in the previous section was measured in a full-cell arrangement in air before and after exposure to different H_2-H_2O blends. Figure 6.10 shows that the total impedance of the cell increases by nearly a factor of three upon switching to a H_2-H_2O mixture corresponding to 8 x 10^{-21} atm O_2 at 750° C. Increases in the ohmic intercept and high frequency processes previously discussed account for the majority of this performance drop. However, upon switching back to air after 250 hours of testing in H_2-H_2O, the total resistance drops to a value *below* the initial measurement in air, while the ohmic

intercept and high-frequency feature's resistance have increased slightly. Upon returning to an even more reducing H_2-H_2O environment (corresponding to 3 x 10^{-22} atm O_2), the resistance of all features continued to increase. Finally, returning to air after 140 hrs of H_2-H_2O testing shows an increased cell resistance compared to the previous measurement in air, mostly from the high-frequency arc.

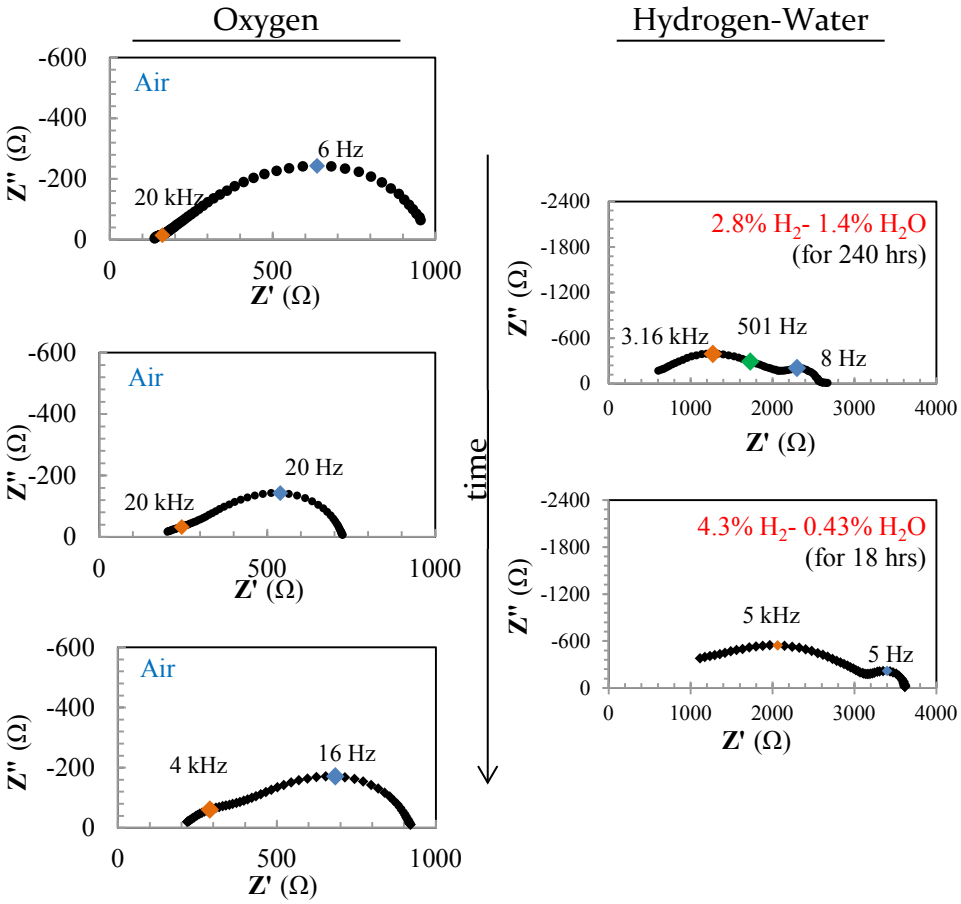

Figure 6.10: The full-cell impedance of the LCF-YSZ cell is measured in air (left) before and after exposure to two reducing gases (right).

Electronic Transport Effects

In order to isolate transport effects from the cell kinetics and interfacial LCF-YSZ processes likely affecting the previous results, a dense, 3 mm-thick pellet of LCF was exposed to both oxidizing and reducing conditions using a gold mesh current

collector. Figure 6.11 shows that in 1% O_2, the measured impedance (besides an inductive tail, likely from the system wiring), is purely real, with a resistance < 1 Ω. Within 10 minutes of switching to a 49% H_2 – 1.2% H_2O gas, the most reducing conditions studied and corresponding to 1.8 x 10^{-23} atm O_2 at 750°C, the impedance drastically changes. The high-frequency intercept increases two orders of magnitude, and an impedance feature appears, with an arc beginning to close at the lowest frequencies tested.

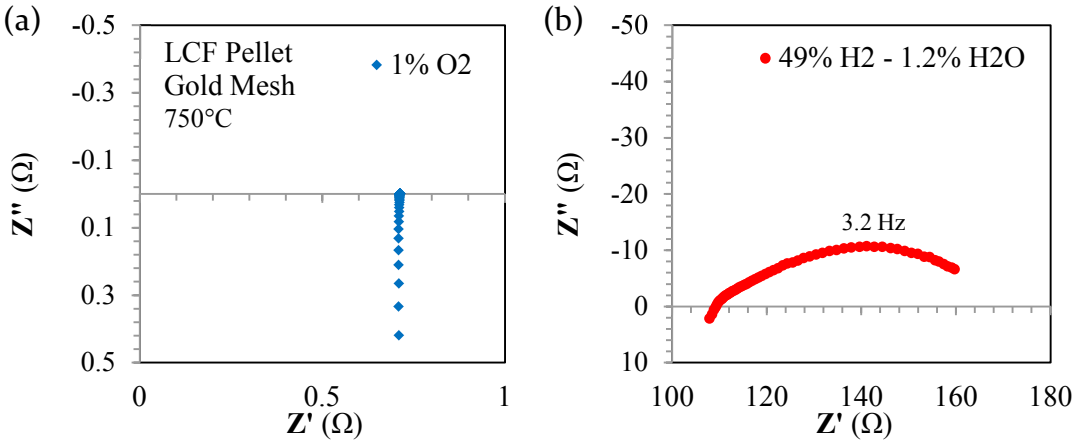

Figure 6.11: EIS measurements of a dense pellet of LCF with gold mesh current collectors exposed to both (a) oxidizing and (b) reducing conditions.

A thin layer of gold paste was applied to both the top and bottom of the same LCF pellet before repeating the above experiment. Figure 6.12 shows that the type of current collector has little effect in oxidizing conditions but greatly affects the performance in reducing conditions. The ohmic intercept is an order of magnitude smaller using gold paste than with the gold mesh. The low-frequency feature is two orders of magnitude smaller using gold paste, with a low-frequency slope of 0.37 and showing no sign of reaching a local minimum.

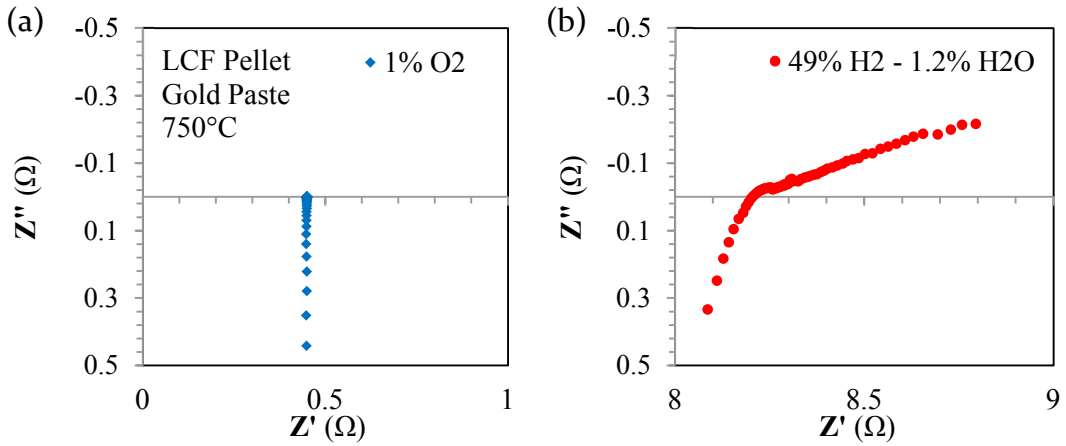

Figure 6.12: EIS measurements of a dense pellet of LCF with gold-painted current collectors exposed to both (a) oxidizing and (b) reducing conditions.

A new LCF-YSZ button cell was made with the addition of gold paste current collectors painted on the working and counter electrodes. Full-cell EIS measurements were taken in 1% O_2 before and after exposure to the same reducing gas blend used in the previous pellet measurements. Figure 6.13 shows that within an hour of exposure to H_2-H_2O, the low-frequency feature's resistance decreased over an order of magnitude, while the high-frequency feature remained relatively constant. Figure 6.14 shows that over 80 hours of H_2-H_2O exposure, R_c of the low-frequency feature remains nearly constant, while R_c of the high-frequency process continually increases. The capacitances of these features fall within the ranges typical of chemical and double-layer capacitances, respectively. Relative to measurements in oxygen prior to H_2-H_2O exposure, returning to 1% O_2 results in a slight decrease in the low-frequency feature and a significant increase in the high-frequency feature.

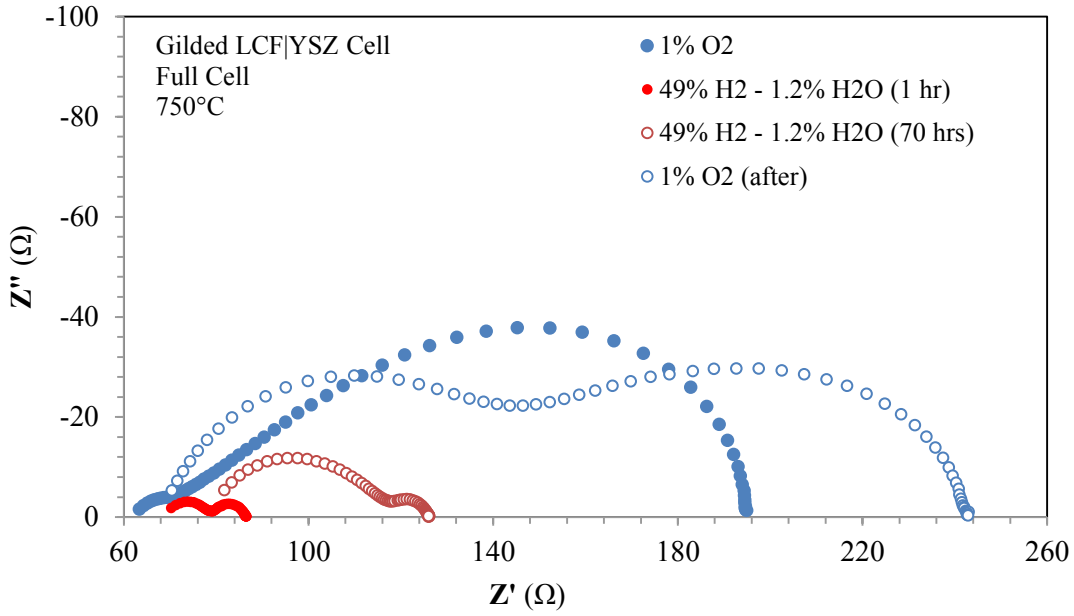

Figure 6.13: Full-cell EIS measurements of an LCF-YSZ button cell with gold-painted current collectors performed before, during, and after switching from air to H_2-H_2O at 750°C.

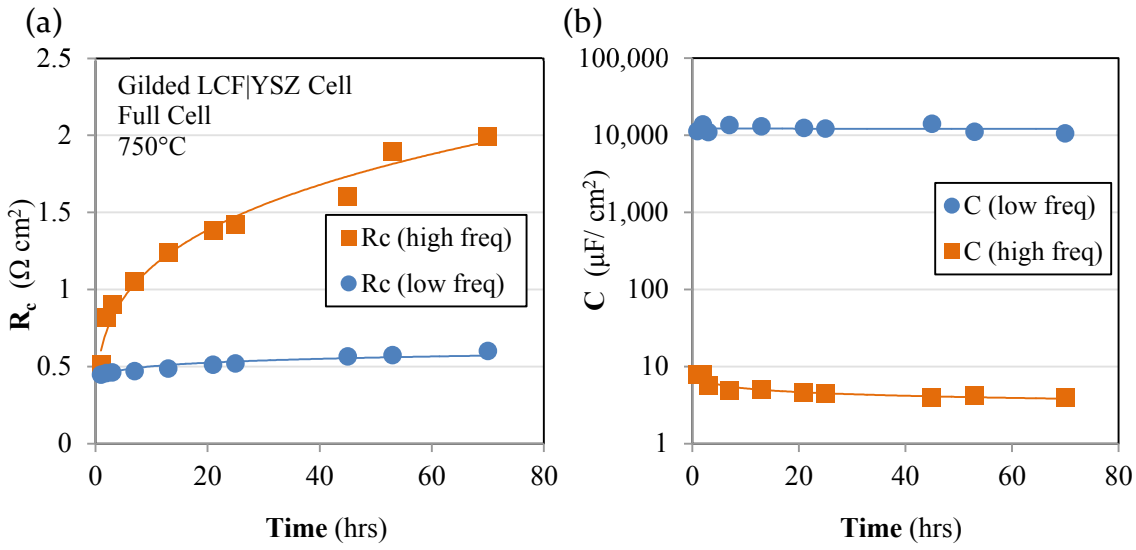

Figure 6.14: The characteristic (a) resistance and (b) capacitance of both the high and low frequency features shown in Figure 6.13 are monitored over 80 hours in a 49% H_2 – 1.2% H_2O environment.

6.5 DISCUSSION

Role of the Current Collector

Comparing the transitions between O_2 and H_2-H_2O environments shown in Figure 6.13 to those in Figure 6.10 highlights the profound effect of using a painted gold current collector versus a gold mesh—a factor often assumed negligible for mixed conductors with high electronic transference numbers. With a gold mesh, the overall cell performance appears to drastically decrease upon switching to reducing environments; with gold paste, the cells show an increase in performance. Measurements performed on multiple LCF-YSZ cells using gold mesh current collectors qualitatively mirrored the presented results for various gas compositions, including the more reducing blend used for studying the gilded cell and pellet.

The negligible catalytic activity of gold suggests this change is tied largely to contact resistances and transport limitations near the gold-electrode interface [95]. The modeling results presented at the beginning of the chapter show that even in the absence of an electrochemical reaction, non-ohmic impedance features can exist, as observed with the LCF pellets with either paste or mesh current collectors. In the case of gold paste, where the applied current is evenly distributed across the gold electrode, the results are directly comparable to those modeled: upon decreasing frequency the cell begins to approach its steady-state oxygen vacancy distribution, yet never comes close to reaching it due to the time constant for vacancy diffusion through a 3 mm thick pellet being orders of magnitude longer than that probed within an EIS experiment. For the case of a gold mesh current collector with only a few widely dispersed contact points, the measured resistance greatly increases from the decreased contact area and increased sheet resistance, and the electrode quickly approaches a pseudo-steady state, explained by a point current source approaching a semi-infinite distribution at short times [30].

The modeling results also show that combining these transport effects with a finite reaction rate produces spectra of indistinguishable shape, yet results in an increased magnitude of both the ohmic intercept and chemical features, easily misattributed as a change in the physical processes typically associated with these features. The experiments performed in oxygen environments show that using a gold mesh has little effect on cell performance when $t_e \approx 0$. Based on estimates using LCF's defect chemistry and LSF's transport properties, LCF-91 is expected to have a maximum of t_e of only 0.04 [29], [75]. However, differing mobilities between LCF and LSF, as well as other works predicting significantly larger electronic mobilities for LSF [27], could result in increased electronic transference numbers for LCF.

Studies comparing current collector materials and configurations of perovskites in oxygen environments show that a gold mesh is a suitable choice [95]. The majority of current collector studies in reducing environments use Ni-YSZ electrodes and focus on the role of the metal's reactivity and diffusion through electrode. Guillodo *et al.* showed that nickel meshes were suitable for electrochemical testing (as well as being comparable to interconnects in SOFC stacks) [96]. The presented work suggests that the lower electronic conductivity of LCF compared to Ni-YSZ greatly amplifies the role of the current collector. Based on this discussion, the following sections assume the current collector's contribution only affects transport within the LCF electrode, and that the gold is not supplying any catalytic activity or reacting significantly with perovskite.

High-Frequency Features

While the low-frequency feature is assumed to represent chemical processes analogous to those studied in the previous chapter, it is unclear the exact nature of the high frequency features dominating the overall response. Typically, high-frequency features with capacitances similar to those observed are attributed to interfacial processes between the electrode and electrolyte [53]. The failure to

detect a significant NLEIS responses at these frequencies excludes any strongly nonlinear phenomena, such as that usually associated with chemical kinetics.

Figure 6.13 shows that in the case of a well-distributed electronic current, the high frequency feature at short exposure times to a reducing gas is of similar frequency and magnitude to that observed in 1% O_2 prior to any H_2-H_2O exposure. Only upon continued H_2-H_2O exposure does this feature continue to grow in magnitude. Comparing Figure 6.10 and Figure 6.13, suggests that—upon returning to oxygen environments, where current collector effects are negligible for both paste and mesh—the severity of growth of this high-frequency feature is correlated to both the exposure time and degree of reducibility of the H_2-H_2O gas. For the 10:1 H_2-H_2O blend, XRD experiments were unable to detect any additional phases, even with a 50-50 wt% LCF-YSZ mixture with a very large interfacial area. However, these measurements are insensitive to the formation of very small volumes of unique phases, as well as cation exchange between phases, such as Ca^{2+} into ZrO_2 or Zr^{4+} into LCF. Anderson *et al.* concluded the latter was present for LCF-YSZ systems in oxygen environments, attributing a slight decrease in performance to changes in hole concentrations due to a shift in A-site valence [25]. Exposure to a reducing gas is likely to change the driving force for cation rearrangement at the electrode-electrolyte interface—a process with a time constant typically on the order of days—possibly explaining the non-immediate, yet continual increase of the feature's resistance in H_2-H_2O [11]. The 42:1 H_2-H_2O blend used for the experiments with gold paste corresponds to a more reducing state than those analyzed via x-ray diffraction, making it impossible to rule out additional phase formation for this case. In addition to affecting the high-frequency impedance feature, both cation rearrangement and tertiary phase formation would result in ion or electron-blocking layers that would increase the ohmic intercept, as observed in all cells.

Low-Frequency Features

In the case of the cells with either gold paste or gold mesh current collectors, the resistance of the low-frequency feature in 1% O_2 decreases slightly after extended periods of electrochemical testing in H_2-H_2O environments. This suggests that oxygen reduction on LCF benefits from prior reduction of the bulk electrode, possibly allowing the surface of the electrode to retain a more reduced than it would without H_2-H_2O exposure. However, the lasting stability of this improvement and its effect on the degradation rate of LCF in O_2 has not been studied.

Figure 6.8 and Figure 6.14 show that throughout H_2-H_2O testing, the characteristic resistance of the chemical process remains stable relative to the high frequency processes, suggesting that the interfacial LCF-YSZ processes discussed in the previous section have minimal effect on the phenomena governing water reduction. Due to the drifting timescales of these high-frequency features, it is difficult to isolate the chemical feature. However, because of the linear nature of the high-frequency phenomena, the nonlinear spectra pertain almost entirely to the chemical feature, making NLEIS a useful tool for isolating the cell's chemical behavior. Unfortunately, without modeling the nonlinear role of current collector-induced transport effects, the NLEIS spectra are subject to many of the same uncertainties as the EIS results when using a gold mesh. As such, the primary utility of NLEIS in this study is to assess the degree of nonlinearity of the high and low-frequency features.

6.6 SUMMARY AND FUTURE WORK

LCF|YSZ cells were studied at 750° C and various reducing blends of H_2 and H_2O using both linear and nonlinear electrochemical impedance spectroscopy. Comparison between cells made using a gold mesh current collector versus gold paste highlighted the dramatic influence current constriction can have at the electrode-current collector interface when the mixed conducting electrode begins to deviate from a predominantly electronic conductor. These transport effects can be easily misattributed to decreased performance of both interfacial and chemical processes, and were largely mitigated using gold paste current collectors, revealing that the total electrode performance greatly improved upon switching to reducing conditions. Upon initial exposure to 49%-1.2% H_2-H_2O, an electrode polarization resistance of 3 Ωcm^2 was observed—on the order of that measured for Ni-YSZ electrodes in similar conditions [97]. However, total performance of the electrode rapidly deteriorated due to increases in the interfacial resistance. While XRD was unable to show a tertiary phase at LCF-YSZ interface upon exposure to a 10:1 H_2-H_2O blend, the possibility of an additional phase for the 42:1 blend cannot be excluded. A likely explanation for the degradation in the former environment could be attributed to cation rearrangement at the interface, adding an ion (or electron) blocking layer, which would also yield the observed continual increase in ohmic resistance of the cell. NLEIS spectra confirmed the linearity of this high-frequency process, further supporting this explanation, as well as highlighting the technique's usefulness for isolating nonlinear chemical features.

Future work will aim to better understand the interfacial degradation between LCF and YSZ by performing XRD experiments in more reducing conditions. Unfortunately, implementation of a protective layer between the electrode and electrolyte is complicated by the most common candidate for oxygen electrodes, doped ceria, behaving as a mixed conductor under reducing conditions [86]. Additionally, discrepancies between full and half-cell measurements (only in

reducing environments) have yet to be analyzed—particularly the possibility of enhanced electronic conductivity of YSZ at the gas-semiconductor interface.

Even in the presence of a transient linear interfacial process obscuring the chemical response, the potential for nonlinear analysis of the rate-determing phenomena governing water reduction on LCF electrodes—and its generalization to a class of n-type mixed-conducting electrodes gaining recent interest—still exists.

7. Summary

7.1 SUMMARY OF RESULTS

The primary goal of the work presented in this dissertation was to improve the understanding of the rate-limiting phenomena affecting the performance of semiconducting MIEC electrodes in both oxidizing and reducing conditions. Two materials, $La_{0.9}Ca_{0.1}FeO_{3-\delta}$ and $La_{0.6}Sr_{0.4}Co_{0.2}Fe_{0.8}O_{3-\delta}$, were selected as candidate electrodes; the former for its stability in both oxidizing and reducing conditions, and the latter for its high performance as an air electrode.

In order to interpret the electrochemical behavior of these electrodes, a thorough understanding of the material's thermodynamics is required—particularly, how its defect chemistry (affecting kinetic and transport phenomena) responds to changes in cell environment. While a large body of thermodynamic data has been collected for LSCF, minimal measurements exist for LCF. To address this, the equilibrium oxygen nonstoichiometry for LCF-91 was measured for oxygen partial pressures, p_{O_2}, between 10^{-3} and 10^{-21} atm and temperatures of 750 to 900°C using a tubular, two-probe Pt|YSZ|LCF coulometric titration cell. The results were interpreted using a point-defect model assuming electronic defects localized around Fe. XRD experiments confirmed that LCF-91 remains a single phase perovskite under the most reducing conditions studied.

Using the defect model developed for LCF-91, a porous electrode modeling framework general to p-type mixed conductors was presented for studying oxygen reduction. Different scenarios for surface diffusion mechanisms, varying surface thermodynamics, and multiple reaction rate laws were considered for both a one-dimensional model, capturing electrode microstructural features as volume-averaged parameters, and a two-dimensional axisymmetric cylindrical model treating the porous electrode as an array of rods. For the latter, a numerical representation of the electrode surface was introduced, simplifying treatment of surface diffusion. For surface diffusion and reaction rates on the order of bulk diffusion, both models predicted similar trends, though minor differences in magnitude and timescale existed.

Linear and nonlinear impedance data were collected between 700-800°C and at 0.01, 0.21, and 1 atm O_2 on symmetric LCF-91|YSZ cells and interpreted using the previously discussed modeling framework. Estimates of the capacitive contribution of the bulk electrode, as well as a depressed-Gerischer linear response imply that the active region of the electrode is limited close to triple phase boundary, increasing the likelihood of multi-dimensional transport effects. Dimensional analysis of the characteristic impedance features suggest moderate surface diffusion with increasing p_{O2}, as well as an equilibrium exchange rate somewhat between that predicted by dissociative adsorption and chemisorption rate laws—though the validity of the latter analysis was shown to be sensitive to the transient nature of the EIS response. The observed nonlinear impedance spectra were found to have a much stronger p_{O2}dependence than what could be explained by a model considering just bulk diffusion and uniform bulk thermodynamics. Even after allowing for surface diffusion, none of the models could explain the observed trends without assuming the electrode surface to be at a more reduced state than predicted by bulk thermodynamics. Only in the case of a dissociate adsorption rate law, interstitial oxygen surface diffusion, and drastically enhanced surface thermodynamics was nonlinear agreement reached.

Similarly for LSCF-6428, EIS and NLEIS data were collected between 550-650°C and at 0.01, 0.1, and 1 atm O_2 and interpreted using the same p-type modeling framework. The shape of the linear spectra and estimates of the active region of the electrode imply that a one-dimensional electrode model is likely adequate. The temperature and p_{O2} dependence of characteristic resistance and frequency are consistent with values in the literature, and appear between those predicted by chemisorption and dissociative adsorption rate laws. The observed nonlinear impedance spectra were found to have a much stronger p_{O2}dependence than explainable by the simplest model considering just bulk diffusion, uniform bulk thermodynamics, and these two rate laws. Even in models allowing for surface diffusion and enhanced surface thermodynamics, neither rate law was found to be consistent with the observed trends, suggesting either additional physics or modified assumptions need to be considered. However, because of the weak p_{O2} dependence of LSCF's bulk reducibility relative to that measured by NLEIS, any rate law is unlikely to be consistent *without* additionally considering strongly p_{O2}-dependent phenomena, such as increased surface reducibility or surface diffusion.

Lastly, LCF-91|YSZ cells were studied at 750° C and various reducing blends of H_2 and H_2O using both linear and nonlinear electrochemical impedance spectroscopy. Comparison between cells made using a gold mesh current collector versus gold paste highlighted the dramatic influence current constriction can have at the electrode-current collector interface when the mixed conducting electrode begins to deviate from a predominantly electronic conductor. These transport effects can be easily misattributed to decreased performance of both interfacial and chemical processes, and were largely mitigated using gold paste current collectors. Doing so revealed the total electrode performance to improve upon switching to reducing conditions, reaching cell resistances comparable to those measured for state-of-the-art Ni-YSZ electrodes. However, total performance of the electrode rapidly deteriorated due to increases in the interfacial resistance. XRD was unable to show a tertiary phase at the LCF-YSZ interface upon exposure

to a 10:1 H_2-H_2O blend. A possible explanation for this degradation could be attributed to cation rearrangement at the interface, forming an insulating layer, which would also yield the observed continual increase in ohmic resistance of the cell. NLEIS spectra confirmed the linearity of this high-frequency process, further supporting this explanation, as well as highlighting the technique's usefulness for isolating partially-concealed nonlinear chemical features.

7.2 IMPLICATIONS AND FUTURE WORK

Comparing these observations for oxygen reduction on LCF and LSCF reveals similar trends between the two electrodes, despite differing in both resistance and vacancy concentrations by over two orders of magnitude. In order to explain the strong p_{O2} dependence of the nonlinear spectra for both LCF and LSCF, the phenomena at the electrode surface must deviate significantly from those predicted for the bulk electrode. The exact nature of this surface alteration remains largely unknown though, motivating further examination.

Dimensional analysis of the impedance data for both electrodes resulted in equilibrium exchange rates "between" those predicted for chemisorption ($p_{O2}x_v^0$) and dissociative adsorption ($p_{O2}x_v^{0^2}$), while nonlinear analysis for LSCF appeared inconsistent with both (for the aforementioned assumptions). For the two simplified mechanisms presented in Chapter 3, all likely scenarios for rate-limiting elementary steps have been considered (though only dissociative adsorption and chemisorption were discussed in the text), and either yielded an indistinguishable rate law or fared no better in providing consistent nonlinear fits than the two presented. Because the proposed "mechanisms" in Chapter 3 are likely simplifications of the actual kinetics—and confirmation of a rate law does not imply a confirmation of mechanism (only consistency) —reformulation of the presented model with an empirical $p_{O2}x_v^{0^n}$ nonlinear rate law may provide further insight.

The presented results for LCF electrodes in hydrogen-water environments motivate future work examining the degradation at the LCF-YSZ interface. Because the chemical feature in these conditions was relatively stable, LCF still remains a candidate for studying H_2-H_2O kinetics upon addressing this high-frequency feature and careful consideration of transport effects near the p-n transition. Furthermore, the performance increase in oxygen after reducing the electrode in H_2-H_2O is poorly understood—both in the stability of this behavior and its underlying cause.

References

[1] B. C. H. Steele, "Oxygen transport and exchange in oxide ceramics," *J. Power Sources*, vol. 49, no. 1–3, pp. 1–14, Apr. 1994.

[2] S. H. Jensen, P. H. Larsen, and M. Mogensen, "Hydrogen and synthetic fuel production from renewable energy sources," *Int. J. Hydrogen Energy*, vol. 32, no. 15, pp. 3253–3257, Oct. 2007.

[3] S. McIntosh and R. J. Gorte, "Direct hydrocarbon solid oxide fuel cells.," *Chem. Rev.*, vol. 104, no. 10, pp. 4845–65, Oct. 2004.

[4] A. Atkinson, S. A. Barnett, R. J. Gorte, J. T. S. Irvine, A. J. McEvoy, M. Mogensen, S. C. Singhal, and J. M. Vohs, "Advanced anodes for high-temperature fuel cells.," *Nat. Mater.*, vol. 3, no. 1, pp. 17–27, Jan. 2004.

[5] S. P. S. Badwal, S. Giddey, and C. Munnings, "Hydrogen production via solid electrolytic routes," *Wiley Interdiscip. Rev. Energy Environ.*, vol. 00, no. February, p. n/a–n/a, Sep. 2012.

[6] A. V Bridgwater, "The technical and economic feasibility of biomass gasification for power generation," *Fuel*, vol. 74, no. 5, pp. 631–653, 1995.

[7] G. W. Huber, S. Iborra, and A. Corma, "Synthesis of transportation fuels from biomass: chemistry, catalysts, and engineering.," *Chem. Rev.*, vol. 106, no. 9, pp. 4044–98, Sep. 2006.

[8] T. Seitarides, C. Athanasiou, and a Zabaniotou, "Modular biomass gasification-based solid oxide fuel cells (SOFC) for sustainable development," *Renew. Sustain. Energy Rev.*, vol. 12, no. 5, pp. 1251–1276, Jun. 2008.

[9] A. Corti, "Biomass integrated gasification combined cycle with reduced CO2 emissions: Performance analysis and life cycle assessment (LCA)," *Energy*, vol. 29, no. 12–15, pp. 2109–2124, 2004.

[10] P. Spath, A. Aden, T. Eggeman, M. Ringer, B. Wallace, and J. Jechura, "Biomass to Hydrogen Production Detailed Design and Economics Utilizing the Battelle Columbus Laboratory Indirectly-Heated Gasifier," 2005.

[11] S. B. Adler, "Factors Governing Oxygen Reduction in Solid Oxide Fuel Cell Cathodes," *Chem. Rev.*, vol. 104, no. 10, pp. 4791–4844, 2004.

[12] J. Mizusaki, "Nonstoichiometry, diffusion, and electrical properties of perovskite-type oxide electrode materials," *Solid State Ionics*, vol. 52, no. 1–3, pp. 79–91, May 1992.

[13] J. Mizusaki, Y. Mima, S. Yamauchi, K. Fueki, and H. Tagawa, "Nonstoichiometry of the perovskite-type oxides La1-xSrxCoO3-[delta]," *J. Solid State Chem.*, vol. 80, no. 1, pp. 102–111, 1989.

[14] J. Mizusaki, M. Yoshihiro, S. Yamauchi, and K. Fueki, "Nonstoichiometry and defect structure of the perovskite-type oxides La1–xSrxFeO3–delta," *J. Solid State Chem.*, vol. 58, no. 2, pp. 257–266, 1985.

[15] M. H. R. Lankhorst, H. J. M. Bouwmeester, and H. Verweij, "Importance of electronic band structure to nonstoichiometric behaviour of La0.8Sr0.2CoO3-d," *Solid State Ionics*, vol. 96, pp. 21–27, 1997.

[16] M. Kuhn, Y. Fukuda, S. Hashimoto, K. Sato, K. Yashiro, and J. Mizusaki, "Oxygen Nonstoichiometry and Thermo-Chemical Stability of Perovskite-Type La0.6Sr0.4Co1-yFeyO3- (y = 0, 0.2, 0.4, 0.5, 0.6, 0.8, 1) Materials," *J. Electrochem. Soc.*, vol. 160, no. 1, pp. F34–F42, Nov. 2013.

[17] S. R. Bishop, K. L. Duncan, and E. D. Wachsman, "Surface and Bulk Defect Equilibria in Strontium-Doped Lanthanum Cobalt Iron Oxide," *J. Electrochem. Soc.*, vol. 156, no. 10, p. B1242, 2009.

[18] J. Mizusaki, S. Yamauchi, K. Fueki, and A. Ishikawa, "Nonstoichiometry of the perovskite-type oxide La1-xSrxCrO3-delta," *Solid State Ionics*, vol. 12, pp. 119–124, 1984.

[19] J. W. Stevenson, T. Armstrong, and R. Carneim, "Electrochemical Properties of Mixed Conducting Perovskites LaMCoFeO (M= Sr, Ba, Ca)," *J. Electrochem. Soc.*, vol. 143, no. 9, pp. 2722–2729, 1996.

[20] K. J. Yoon, P. A. Zink, S. Gopalan, U. B. Pal, and L. R. Pederson, "Defect Chemistry and Electrical Properties of (La[sub 0.8]Ca[sub 0.2])[sub 0.95]FeO[sub 3–δ]," *J. Electrochem. Soc.*, vol. 156, no. 7, p. B795, 2009.

[21] P. A. Zink, K. J. Yoon, U. B. Pal, and S. Gopalan, "Analysis of the Electronic and Ionic Conductivity of Calcium-Doped Lanthanum Ferrite," *Electrochem. Solid-State Lett.*, vol. 12, no. 10, p. B141, 2009.

[22] K. Efimov, T. Klande, N. Juditzki, and A. Feldhoff, “Ca-containing CO2-tolerant perovskite materials for oxygen separation,” *J. Memb. Sci.*, vol. 389, pp. 205–215, Feb. 2012.

[23] P. Dyer, M. F. Carolan, D. Butt, R. H. E. Van Doorn, and R. A. Cutler, “Mixed Conducting Membranes for Syngas Production,” 64922902002.

[24] F. M. Figueiredo, J. A. Labrincha, J. Frade, and F. Marques, “Reactions between a zirconia-based electrolyte and LaCoO3-based electrode materials,” *Solid State Ionics*, vol. 2738, no. 97, 1997.

[25] M. D. Anderson, J. W. Stevenson, and S. P. Simner, “Reactivity of lanthanide ferrite SOFC cathodes with YSZ electrolyte,” *J. Power Sources*, vol. 129, no. 2, pp. 188–192, Apr. 2004.

[26] S. P. Simner, J. P. Shelton, M. D. Anderson, and J. W. Stevenson, “Interaction between La(Sr)FeO3 SOFC cathode and YSZ electrolyte,” *Solid State Ionics*, vol. 161, no. 1–2, pp. 11–18, Jul. 2003.

[27] M. V. Patrakeev, J. a. Bahteeva, E. B. Mitberg, I. a. Leonidov, V. L. Kozhevnikov, and K. R. Poeppelmeier, “Electron/hole and ion transport in La1–xSrxFeO3–δ,” *J. Solid State Chem.*, vol. 172, no. 1, pp. 219–231, Apr. 2003.

[28] M. Hung, M. V. Rao, and D. Tsai, “Microstructures and electrical properties of calcium substituted LaFeO3 as SOFC cathode,” *Mater. Chem. Phys.*, vol. 101, no. 2–3, pp. 297–302, Feb. 2007.

[29] J. Mizusaki, T. Sasamoto, W. R. Cannon, and H. K. Bowen, “Electronic Conductivity, Seebeck Coefficient, and Defect Structure of Lal-,Sr,FeO3 (x=O.l, 0.25),” *J. Am. Ceram. Soc.*, vol. 1, no. April, 1983.

[30] J. Newman and K. E. Thomas-Alyea, “Transport Processes in Electrolytic Solutions,” in *Electrochemical Systems*, Third., John Wiley & Sons, 2004, pp. 269–368.

[31] F. Bidrawn, S. Lee, J. M. Vohs, and R. J. Gorte, “The Effect of Ca, Sr, and Ba Doping on the Ionic Conductivity and Cathode Performance of LaFeO[sub 3],” *J. Electrochem. Soc.*, vol. 155, no. 7, p. B660, 2008.

[32] J. Mizusaki, K. Amano, S. Yamauchi, and K. Fueki, “Electrode reaction at Pt, O 2(g)/stabilized zirconia interfaces. Part II: Electrochemical measurements and analysis,” *Solid State Ionics*, vol. 22, no. 1987, pp. 323–330, 1987.

[33] G. J. la O', B. Yildiz, S. McEuen, and Y. Shao-Horn, "Probing Oxygen Reduction Reaction Kinetics of Sr-Doped LaMnO[sub 3] Supported on Y[sub 2]O[sub 3]-Stabilized ZrO[sub 2]," *J. Electrochem. Soc.*, vol. 154, no. 4, p. B427, 2007.

[34] Y. Lu, C. R. Kreller, and S. B. Adler, "Measurement and Modeling of the Impedance Characteristics of Porous La[sub 1–x]Sr[sub x]CoO[sub 3–δ] Electrodes," *J. Electrochem. Soc.*, vol. 156, no. 4, p. B513, 2009.

[35] S. B. Adler, J. A. Lane, and B. C. H. Steele, "Electrode Kinetics of Porous Mixed-Conducting Oxygen Electrodes," *J. Electrochem. Soc.*, vol. 143, no. 11, p. 3554, 1996.

[36] J. Ten Elshof, M. H. R. Lankhorst, and H. J. M. Bouwmeester, "Oxygen Exchange and Diffusion Coefficients of Strontium-Doped Lanthanum Ferrites by Electrical Conductivily Relaxation," *J. Electrochem. Soc.*, vol. 144, no. 3, pp. 1060–1067, 1997.

[37] L. M. van der Haar, M. W. den Otter, M. Morskate, H. J. M. Bouwmeester, and H. Verweij, "Chemical Diffusion and Oxygen Surface Transfer of La[sub 1–x]Sr[sub x]CoO[sub 3–δ] Studied with Electrical Conductivity Relaxation," *J. Electrochem. Soc.*, vol. 149, no. 3, p. J41, 2002.

[38] C. R. Kreller, "Measurement and Modeling of Material and Microstructural Factors Governing Performance of Solid Oxide Fuel Cell Cathodes," 2011.

[39] J. R. Wilson, D. T. Schwartz, and S. B. Adler, "Nonlinear electrochemical impedance spectroscopy for solid oxide fuel cell cathode materials," *Electrochim. Acta*, vol. 51, no. 8–9, pp. 1389–1402, 2006.

[40] J. Mizusaki, H. Tagawa, T. Saito, T. Yamamura, K. Kamitani, K. Hirano, and S. Ehara, "Kinetic studies of the reaction at the nickel pattern electrode on YSZ in Hz-H20 atmospheres," *Solid State Ionics*, vol. 70/71, pp. 52–58, 1994.

[41] a. Utz, H. Störmer, a. Leonide, a. Weber, and E. Ivers-Tiffée, "Degradation and Relaxation Effects of Ni Patterned Anodes in H[sub 2]–H[sub 2]O Atmosphere," *J. Electrochem. Soc.*, vol. 157, no. 6, p. B920, 2010.

[42] M. Vogler, A. Bieberle-Hütter, L. J. Gauckler, J. Warnatz, and W. G. Bessler, "Modelling Study of Surface Reactions, Diffusion, and Spillover at a Ni/YSZ Patterned Anode," *J. Electrochem. Soc.*, vol. 156, no. 5, p. B663, 2009.

[43] T. Horita, H. Kishimoto, K. Yamaji, Y. Xiong, N. Sakai, M. Brito, and H. Yokokawa, "Materials and reaction mechanisms at anode/electrolyte interfaces for SOFCs," *Solid State Ionics*, vol. 177, no. 19–25, pp. 1941–1948, Oct. 2006.

[44] D. G. Goodwin, H. Zhu, A. M. Colclasure, and R. J. Kee, "Modeling Electrochemical Oxidation of Hydrogen on Ni–YSZ Pattern Anodes," *J. Electrochem. Soc.*, vol. 156, no. 9, p. B1004, 2009.

[45] F. Bidrawn, G. Kim, G. Corre, J. T. S. Irvine, J. M. Vohs, and R. J. Gorte, "Efficient Reduction of CO2 in a Solid Oxide Electrolyzer," *Electrochem. Solid-State Lett.*, vol. 11, no. 9, p. B167, 2008.

[46] Z. Zhan and L. Zhao, "Electrochemical reduction of CO2 in solid oxide electrolysis cells," *J. Power Sources*, vol. 195, no. 21, pp. 7250–7254, Nov. 2010.

[47] P. Kim-lohsoontorn and J. Bae, "Electrochemical performance of solid oxide electrolysis cell electrodes under high-temperature coelectrolysis of steam and carbon dioxide," *J. Power Sources*, 2010.

[48] S. D. Ebbesen and M. Mogensen, "Electrolysis of carbon dioxide in Solid Oxide Electrolysis Cells," *J. Power Sources*, vol. 193, no. 1, pp. 349–358, Aug. 2009.

[49] D. M. Bastidas, S. Tao, and J. T. S. Irvine, "A symmetrical solid oxide fuel cell demonstrating redox stable perovskite electrodes," *J. Mater. Chem.*, vol. 16, no. 17, p. 1603, 2006.

[50] S. Tao and J. T. S. Irvine, "A redox-stable efficient anode for solid-oxide fuel cells.," *Nat. Mater.*, vol. 2, no. 5, pp. 320–3, May 2003.

[51] Y. Zheng, C. Zhang, R. Ran, R. Cai, Z. Shao, and D. Farrusseng, "A new symmetric solid-oxide fuel cell with La0.8Sr0.2Sc0.2Mn0.8O3-δ perovskite oxide as both the anode and cathode," *Acta Mater.*, vol. 57, no. 4, pp. 1165–1175, Feb. 2009.

[52] Q. Liu, C. Yang, X. Dong, and F. Chen, "Perovskite Sr2Fe1.5Mo0.5O6-delta as electrode materials for symmetrical solid oxide electrolysis cells," *Int. J. Hydrogen Energy*, vol. 35, no. 19, pp. 10039–10044, 2010.

[53] T. Nakamura, T. Kobayashi, K. Yashiro, A. Kaimai, T. Otake, K. Sato, J. Mizusaki, and T. Kawada, "Electrochemical Behaviors of Mixed Conducting

Oxide Anodes for Solid Oxide Fuel Cell," *J. Electrochem. Soc.*, vol. 155, no. 6, p. B563, 2008.

[54] R. D. Green, C. Liu, and S. B. Adler, "Carbon dioxide reduction on gadolinia-doped ceria cathodes," *Solid State Ionics*, vol. 179, no. 17–18, pp. 647–660, Jul. 2008.

[55] S. Diethelm, J. Van Herle, H. Middleton, and D. Favrat, "Oxygen permeation and stability of La0.4Ca0.6Fe1–xCoxO3–δ (x = 0, 0.25, 0.5) membranes," *J. Power Sources*, vol. 118, no. 1–2, pp. 270–275, 2003.

[56] P. Ciambelli, S. Cimino, L. Lisi, M. Faticanti, D. Minelli, I. Pettiti, and P. Porta, "La, Ca and Fe oxide perovskites: preparation, characterization and catalytic properties for methane combustion," *Appl. Catal. B Environ.*, vol. 33, no. 3, pp. 193–203, Oct. 2001.

[57] L. Isupova, S. V Tsybulya, G. N. Kryukova, G. M. Alikina, N. N. Boldyreva, A. A. Vlasov, O. I. Snegurenko, V. P. Ivanov, V. N. Kolomiichuk, and V. Sadykov, "Physicochemical and Catalytic Properties of LaCaFeO3 Perovskites Prepared Using Mechanochemical Activation," *Kinet. Catal.*, vol. 43, no. 1, pp. 140–149, 2002.

[58] R. Jiménez, R. Zamora, G. Pecchi, X. García, and a. L. Gordon, "Effect of Ca-substitution in La1–xCaxFeO3 perovskites on the catalytic activity for soot combustion," *Fuel Process. Technol.*, vol. 91, no. 5, pp. 546–549, May 2010.

[59] G. Pecchi, P. Reyes, R. Zamora, C. Campos, L. Cadus, and B. P. Barbero, "Effect of the preparation method on the catalytic activity of La1–xCaxFeO3 perovskite-type oxides," *Catal. Today*, vol. 133–135, pp. 420–427, Apr. 2008.

[60] B. P. Barbero, J. Gamboa, and L. Cadus, "Synthesis and characterisation of La1–xCaxFeO3 perovskite-type oxide catalysts for total oxidation of volatile organic compounds," *Appl. Catal. B Environ.*, vol. 65, no. 1–2, pp. 21–30, May 2006.

[61] J. Li, "Investigation of orthorhombic perovskite La1-xCaxFeO3-y (0< x< 0.50)," *Phys. Scr.*, vol. 45, pp. 62–64, 1992.

[62] E. K. Abdel-Khalek and H. M. Mohamed, "Synthesis, structural and magnetic properties of La1 – xCaxFeO3 prepared by the co-precipitation method," *Hyperfine Interact.*, vol. 222, no. 1, pp. 57–67, Aug. 2013.

[63] R. Andoulsi, K. Horchani-Naifer, and M. Férid, “Structural and electrical properties of calcium substituted lanthanum ferrite powders,” *Powder Technol.*, vol. 230, no. 3, pp. 183–187, Nov. 2012.

[64] M. V. Patrakeev, I. a. Leonidov, and V. L. Kozhevnikov, “Applications of coulometric titration for studies of oxygen non-stoichiometry in oxides,” *J. Solid State Electrochem.*, vol. 15, no. 5, pp. 931–954, Jun. 2010.

[65] J. Park and R. N. Blumenthal, “Electronic Transport in 8 Mole Percent Y2O3-ZrO2,” *J. Electrochem. Soc.*, vol. 136, no. 10, 1989.

[66] L. Heyne, “Ionic Conductivity in Oxides,” *Natl. Bur. Stand.*, pp. 149–164, 1968.

[67] M. H. R. Lankhorst, H. J. M. Bouwmeester, and H. Verweij, “High-Temperature Coulometric Titration of LSC Evidence for the Effect of Electronic Band Structure on Nonstoichiometry Behavior,” *J. Solid State Chem.*, vol. 133, pp. 555–567, 1997.

[68] J. Mizusaki, H. Tagawa, K. Naraya, and T. Sasamoto, “Nonstoichiometry and thermochemical stability of the perovskite-type La1-xSrMnO3-delta,” *Solid State Ionics*, vol. 49, pp. 111–118, 1991.

[69] M. H. R. Lankhorst and H. J. M. Bouwmeester, “Determination of Oxygen Nonstoichiometry and Diffusivily in mixed conducting oxides by oxygen coulometric titration - I - Chemical Diffusion in La08Sr02CoO3-d,” *J. Electrochem. Soc.*, vol. 144, no. 4, pp. 0–6, 1997.

[70] J. Park and R. Blumenthal, “Thermodynamic Properties of Nonstoichiometric Yttria-Stabilized Zirconia at Low Oxygen Pressures,” *J. Am. Ceram. Soc.*, vol. 72, no. 8, pp. 1485–87, 1989.

[71] C. Wagner, “The determination of small deviations from the ideal stoichiometric composition of ionic crystals and other binary compounds,” *Prog. Solid State Chem.*, vol. 6, pp. 1–15, 1971.

[72] J. Newman and K. E. Thomas-Alyea, “Thermodynamics of Electrochemical Cells,” in *Electrochemical Systems*, Third., John Wiley & Sons, 2004, pp. 27–128.

[73] C. Wagner, “The electromotive force of galvanic cells involving phases of locally variable composition,” in *Advances in Electrochemistry and Electrochemical Engineering IV*, P. Delahay and C. W. Tobias, Eds. New York: Interscience, 1966, pp. 1–46.

[74] C. Kreller, M. Drake, S. Adler, and H. Chen, "Modeling SOFC cathodes based on 3-D representations of electrode microstructure," *ECS Trans.*, vol. 35, no. 1, pp. 815–822, 2011.

[75] T. C. Geary and S. B. Adler, "Oxygen nonstoichiometry and defect chemistry of the mixed conductor La0.9Ca0.1FeO3–δ at low oxygen partial pressure," *Solid State Ionics*, vol. 253, pp. 88–93, 2013.

[76] S. B. Adler, X. Chen, and J. R. Wilson, "Mechanisms and rate laws for oxygen exchange on mixed-conducting oxide surfaces," *J. Catal.*, vol. 245, no. 1, pp. 91–109, Jan. 2007.

[77] H. von Gerischer, "Wechselstrompolarisation von Elektroden mit einem potentialbestimmenden Schritt beim Gleichgewichtspotential," *Zeitschrift fur Phys. Chemie.--1951.--Bd*, vol. 198, pp. 286–314, 1951.

[78] T. Kawada, J. Suzuki, M. Sase, A. Kaimai, K. Yashiro, Y. Nigara, J. Mizusaki, K. Kawamura, and H. Yugami, "Determination of Oxygen Vacancy Concentration in a Thin Film of La[sub 0.6]Sr[sub 0.4]CoO[sub 3–δ] by an Electrochemical Method," *J. Electrochem. Soc.*, vol. 149, no. 7, p. E252, 2002.

[79] Y. Lu, C. R. Kreller, S. B. Adler, J. R. Wilson, S. a. Barnett, P. W. Voorhees, H.-Y. Chen, and K. Thornton, "Performance Variability and Degradation in Porous La1-xSrxCoO3- Electrodes," *J. Electrochem. Soc.*, vol. 161, no. 4, pp. F561–F568, Feb. 2014.

[80] E. J. Crumlin, E. Mutoro, Z. Liu, M. E. Grass, M. D. Biegalski, Y.-L. Lee, D. Morgan, H. M. Christen, H. Bluhm, and Y. Shao-Horn, "Surface strontium enrichment on highly active perovskites for oxygen electrocatalysis in solid oxide fuel cells," *Energy Environ. Sci.*, vol. 5, no. 3, p. 6081, 2012.

[81] S. Kim and J. Maier, "On the Conductivity Mechanism of Nanocrystalline Ceria," *J. Electrochem. Soc.*, vol. 149, no. 10, p. J73, 2002.

[82] a. Esquirol, N. P. Brandon, J. a. Kilner, and M. Mogensen, "Electrochemical Characterization of La[sub 0.6]Sr[sub 0.4]Co[sub 0.2]Fe[sub 0.8]O[sub 3] Cathodes for Intermediate-Temperature SOFCs," *J. Electrochem. Soc.*, vol. 151, no. 11, p. A1847, 2004.

[83] H. J. M. Bouwmeester, M. W. Otter, and B. a. Boukamp, "Oxygen transport in La0.6Sr0.4Co1-y Fe y O3," *J. Solid State Electrochem.*, vol. 8, no. 9, pp. 599–605, Mar. 2004.

[84] T. Horita, M. Nishi, T. Shimonosono, H. Kishimoto, K. Yamaji, M. E. Brito, and H. Yokokawa, "Visualization of oxide ionic diffusion at SOFC cathode/electrolyte interfaces by isotope labeling techniques," *Solid State Ionics*, pp. 16–20, Feb. 2014.

[85] H. Inaba and H. Tagawa, "Ceria-based solid electrolytes," *Solid state ionics*, vol. 83, 1996.

[86] K. Yashiro, S. Onuma, A. Kaimai, Y. Nigara, T. Kawada, J. Mizusaki, K. Kawamura, T. Horita, and H. Yokokawa, "Mass transport properties of Ce0.9Gd0.1O2-delta at the surface and in the bulk," *Solid State Ionics*, vol. 153, pp. 469 – 476, 2002.

[87] J. Lane and J. Kilner, "Measuring oxygen diffusion and oxygen surface exchange by conductivity relaxation," *Solid State Ionics*, vol. 137, pp. 997–1001, 2000.

[88] M. Sahibzada, W. Morton, and A. Hartley, "A simple method for the determination of surface exchange and ionic transport kinetics in oxides," *Solid State Ionics*, vol. 137, pp. 991–996, 2000.

[89] a. Leonide, B. Rüger, A. Weber, W. a. Meulenberg, and E. Ivers-Tiffée, "Impedance Study of Alternative (La,Sr)FeO[sub 3–δ] and (La,Sr)(Co,Fe)O[sub 3–δ] MIEC Cathode Compositions," *J. Electrochem. Soc.*, vol. 157, no. 2, p. B234, 2010.

[90] H. J. Hwang, J.-W. Moon, S. Lee, and E. a Lee, "Electrochemical performance of LSCF-based composite cathodes for intermediate temperature SOFCs," *J. Power Sources*, vol. 145, no. 2, pp. 243–248, Aug. 2005.

[91] M. Kuhn, S. Hashimoto, K. Sato, K. Yashiro, and J. Mizusaki, "Oxygen nonstoichiometry, thermo-chemical stability and lattice expansion of La0.6Sr0.4FeO3–δ," *Solid State Ionics*, pp. 2–10, Jun. 2011.

[92] A. Bieberle-Hütter, L. P. Meier, and L. J. Gauckler, "The Electrochemistry of Ni Pattern Anodes Used as Solid Oxide Fuel Cell Model Electrodes," *J. Electrochem. Soc.*, vol. 148, no. 6, p. A646, 2001.

[93] I. Riess, "Four point Hebb-Wagner polarization method for determining the electronic conductivity in mixed ionic-electronic conductors," *Solid State Ionics*, vol. 51, no. 3–4, pp. 219–229, Apr. 1992.

[94] L. Heyne, “Electrochemistry of Mixed Ionic-Electronic Conductors,” *Top. Appl. Phys.*, vol. 21, pp. 169–221, 1977.

[95] S. Jiang, J. G. Love, and L. Apateanu, “Effect of contact between electrode and current collector on the performance of solid oxide fuel cells,” *Solid State Ionics*, vol. 160, no. 1–2, pp. 15–26, May 2003.

[96] M. Guillodo, P. Vernoux, and J. Fouletier, “Electrochemical properties of Ni–YSZ cermet in solid oxide fuel cells: effect of current collecting,” *Solid State Ionics*, vol. 127, pp. 99–107, 2000.

[97] M. Brown, S. Primdahl, and M. Mogensen, “Structure/Performance Relations for Ni/Yttria-Stabilized Zirconia Anodes for Solid Oxide Fuel Cells,” *J. Electrochem. Soc.*, vol. 147, no. 2, p. 475, 2000.